MYELIN SENSITIVITY IN QUANTITATIVE MAGNETIZATION TRANSFER AND DIFFUSION TENSOR IMAGING IN AN ANIMAL MODEL OF MULTIPLE SCLEROSIS

By

Vaibhav A. Janve

Dissertation

Submitted to the Faculty of the

Graduate School of Vanderbilt University,

Nashville, Tennessee

in partial fulfillment of the requirements

for the degree of

DOCTOR OF PHILOSOPHY

in

Physics

May, 2015

Nashville, Tennessee

Approved:

Daniel F. Gochberg, PhD

Adam W. Anderson, PhD

Mark D. Does, PhD

David J. Ernst, PhD

John C. Gore, PhD

DEDICATION

To my Parents

Late Dr. Anil V. Janve and Smt. Sulbha A. Janve,

Whom I owe everything, and

Vaishali Satpute,

My loving wife and infinitely supportive

ACKNOWLEDGEMENTS

I would like to express my appreciation and thanks all the people who helped me finish my Ph.D. First, I would like to thank Dr. Daniel Frank Gochberg for holding numerous meeting, providing pinpointed critiques, making me work independently throughout, and having me figure my way out in the graduate school. These experiences helped me to think independently, problem solve, and gave me the freedom figure out myself and grow.

I am thankful to all the members of my thesis committee for their scientific input. I am deeply grateful to Dr. Gore for directing me to the critical aspects of MR imaging and giving insightful suggestions. The leadership of Dr. Gore has created a great atmosphere of trust and collaboration at the Vanderbilt University Institute of Imaging Science. During my committee meeting he has broadened my understanding by asking me big picture questions and fundamental aspects of my study. Dr. Does helped me focus on critical aspects of my project and to identify the main areas, I need to improve on. I am thankful to Dr. Ernst for always finding time to provide guidance and share his thoughtful insights. I am especially thankful to Dr. Anderson for his willingness to help and support me when no one else would. His input on diffusion tensor imaging was much needed to move my project forward. Finally, I would like to thank my committee members for being flexible to schedule committee meetings and taking time from their busy schedules.

I would like to thank Dr. Yankeelov to kindle my interest in imaging to a level that I could endure through the ups and downs of graduate school. His passion conveys a genuine interest to help students. He helped me address important aspect of my research question that I had struggled

for long time by suggesting appropriate analysis (ROC analysis). I look up to him as an individual who has the commitment to empower others.

I would like to acknowledge the support of Dr. Shriram Subramaniam for providing critical insights and the animals for my thesis project. I thank Dr. Song-yi Yao for performing the injections in rat brains and histology staining of the brain slices. Without their help in providing theses resources this project would not have possible.

I would like to acknowledge the help and support of Dr. Zhongliang Zu to help me get through difficult times. It was a pleasure to have the opportunity to work with him and discuss numerous aspects of imaging research. With his help, I got my first abstract accepted in ISMRM, which provided me the opportunity to see exciting imaging research from across the world. Dr. Zu was also upfront in giving the guidance when I critically needed it. Over the course of my graduate career he helped me as much with life issues as he did scientifically. It has been inspirational to see him grow from a productive and hardworking post-doctoral fellow to a faculty. I wish him all the very best for his scientific journey.

It is difficult to articulate all the wonderful memories and experiences at VUIIS and physics department. I would like to thank Xiawei Ou, Aroshan jaysinghe, David Mashburn, Aritra, joyeeta, Vimal, Jeff Luci, Richard Baheza, Zhou, Ming, Chaohui, Don Pickert, Sandy Childress, Peggy, Vicky Greene for giving a wonderful experience at VUIIS.

It would not have been possible to continue my Ph.D. without the funding support from the Department of Physics and Astronomy. My teaching assistant duties have improved my communication skills and helped me become a better teacher. I would also like to thank Carolyn Dever, Dean of College of Arts and Sciences for the Summer Research Award, a grant that helped to me add a new dimension to my thesis project.

It would be impossible to have reached to this point in my life without the infinite love and support of my mother Mrs. Sulbha Janve. Thank you for always believing in me and encouraging me. Even in difficult times for the family she made sure I get what is needed for my growth. She is an example of how to rise gracefully above life's challenges no matter how difficult the situation seems. I love her and miss her with all my heart. I also thank Liz Leis for the invitation letter that helped to get my mother get the US VISA. I would like to thank Dean Ruth Schemmer for excellent career support. I would like to thank Teniel Ramikie for being a true friend and helping out in difficult times.

Most of all, I thank my wife Vaishali for her selflessness, tremendous support and motivation. She moved to Nashville to support me, even when there was lot at stake, without her this journey would not have been possible.

ABSTRACT

Conventional MRI is sensitive to detect brain abnormalities non-invasively through excellent contrast generated by variation in relaxation times and water proton density. However, conventional MRI lacks the specificity and quantitation to specific pathologies and tissue components such as myelin. Myelin is the major constituent of white matter ─an insulating macromolecular sleeve wrapped around axons of brain cells. Loss of white matter, specifically myelin leads to severe motor and cognitive deficits in diseases such as multiple sclerosis. Advanced quantitative MRI methods such as quantitative magnetization transfer (qMT) and diffusion tensor imaging (DTI) have emerged as putative biomarkers that improve sensitivity, specificity and provide quantitative metrics to measure myelin. qMT and DTI are model based quantitative techniques, which provide sub-voxel information of the underlying tissue architecture. qMT is sensitive to the tissue macromolecular content, whereas DTI is sensitive to tissue microstructure. Pool size ratio (PSR, a qMT parameter) and radial diffusivity (RD, a DTI parameter) provide an indirect quantitative measure of myelin. However, their relative sensitivities and specificities to myelin are unclear. qMT and DTI are based on different physical principles and may provide complementary information. While histology is the gold standard for myelin quantification, it can only be performed postmortem or through invasive biopsies. Thus, systematic quantitative MRI and histological validation studies are essential to determine the specific sensitivities of non-invasive quantitative metrics. Although, limited data is available on such studies due to their tedious, time intensive and complex nature. My thesis work addresses this gap by performing quantitative MRI and histological validation on a relatively new animal model of multiple sclerosis (MS), which recapitulates the inflammatory and non-inflammatory

demyelinating phases seen in patients. The animal model was characterized using structural MRI, qMRI and histological methods. To enable quantitative comparisons amongst MRI and histological parameters, detailed processing protocol were designed and implemented including 3D qMT and DTI protocols and histological pipeline. *In vivo* and *ex vivo* studies were performed and qMT and DTI metrics were correlated with histology and among each other to determine their specific sensitivities. Furthermore, in an attempt to translate the animal work to clinical settings, a fast qMT sequence with GRASE readout was tested on human scanners. In conclusion, we found that PSR, and RD are sensitive to histological myelin content with PSR having the strongest correlation.

TABLE OF CONTENTS

LIST OF TABLES

Table Page

Chapter II

Chapter III

LIST OF FIGURES

Figure Page

Chapter I

Chapter II

APPENDIX

ABBREVIATIONS

AD	Axial diffusivity
CC	corpus callosum
CNS	central nervous system
CSF	cerebrospinal fluid
CT	X-ray computed tomography
DTI	diffusion tensor imaging
DWI	Diffusion Weighted Imaging
EAE	experimental allergic encephalomyelitis
FLAIR	Fluid attenuated inversion recovery
FR	Fast rate
GM	gray matter
IC	Internal Capsule
LFB	Luxol-Fast blue
LPS	lipopolysaccharide
MBP	myelin basic protein
MeT2	Multiexponential-T_2
MRI	Magnetic resonance imaging
MS	multiple sclerosis
MT	magnetization transfer
MTI	Magnetization transfer imaging
MTR	Magnetization transfer ratio
NMR	nuclear magnetic resonance

OD	optical density
PAS	Periodic-Acid Schiff
PBS	phosphate buffer saline
PD	proton density
PNS	peripheral nervous system
PSR	pool size ratio
qMRI	quantitative magnetic resonance imaging
qMT	quantitative magnetization transfer
qMTI	quantitative magnetization transfer imaging
RA	Relative anisotropy
RD	radial diffusivity
RF	radio frequency
ROI	Region of interest
ROIs	regions of interest
Sf	Inversion efficiency parameter
SIR	selective inversion recovery
SNR	signal to noise ratio
SR	Slow rate
T1-w	T1 weighted
T2s-w	T2 star weighted
T2-w	T2 weighted
TE	Echo time
TR	Repetition time
WM	white matter

CHAPTER I

INTRODUCTION

In this chapter, we introduce the underlying motivation for the thesis and briefly explain the key scientific and technical principles upon which our work rests. Specifically, we discuss the facets of multiple sclerosis (MS), the fundamentals of magnetic resonance imaging (MRI), and the application of conventional and quantitative MRI methods to assess the MS pathologies with particular emphasis on demyelination. These topics lay the ground work for chapters two and three, where we examine the specific sensitivities of quantitative MRI methods to myelin in an animal model of MS.

Motivation

MRI is currently established as one of the most useful methods for imaging soft tissue anatomy due to its excellent soft tissue contrast. In particular, MRI plays an essential role in the diagnosis of MS - a neurodegenerative disease of the central nervous system (CNS) - and has a potential to serve as a biological marker of the severity of this disease. MRI methods continue to evolve to meet clinical needs. Currently, there is a need to transition from qualitative MRI methods, used for diagnosis, to quantitative MRI methods especially suited for the assessment and monitoring of disease progression and treatment efficacy. The work presented here is aimed at determining the specific sensitivities to myelin of two promising quantitative MRI methods,

quantitative magnetization transfer (qMT) and diffusion tensor imaging (DTI). Myelin is a membranous structure enveloping axons of nerve cells in both the central (CNS) and peripheral nervous system (PNS) of vertebrates. Determining myelin content is of great interest as demyelination (loss of myelin) is a central feature in many white matter diseases, with MS being the most common one. Furthermore, white matter abnormalities are observed in many neurological and psychological disorders in which white matter abnormality is not considered as the primary etiology, such as Alzheimer's disease, Schizophrenia, depression, and learning and reading disorders. Thus, quantifying demyelination with greater sensitivity and specificity is important from both clinical and research point of view. As MS is the most common demyelinating disease our work focusses on quantifying demyelination in an animal model of MS.

Multiple sclerosis (MS)

MS is a chronic neurodegenerative disease of the CNS with progressive disability. The prominent feature of MS is loss of motor control, though decline in many other CNS functions are also observed in patients. MS symptoms usually appear in the third or fourth decade of life, and later progresses to an irreversible neurological condition by the sixth or seventh decade. Among young adults MS is the most common cause of neurological disability. The early onset of MS during the prime productive time of adults has huge economic costs (Naci et al., 2010). Although the disability in MS may wax and wane, especially in the early stages, it is recognized that MS is an active condition in most patients. Cumulative damage during the reversible phase of MS ultimately reaches a point of no return, leading to progressive impairment in most patients. Brian and spinal cord lesions seen with MRI images make the diagnosis of MS more

accurate than with symptoms alone. However, there is a need to develop quantitative MRI methods that can improve diagnosis and management of MS.

MS subtypes

In majority of individuals MS presents as a complex combination of pathologies such as inflammation, demyelination, axonal loss, and gliosis. In addition, MS pathology can manifest in a focal or diffused form throughout the CNS. The highly heterogeneous nature of MS at multiple levels including lesions, the clinical progression and response to treatments in patients adds to the difficulty of identifying the underlying mechanisms. In an effort to increase diagnostic accuracy and treatment efficacy, MS has been classified as relapsing–remitting, primary–progressive, secondary–progressive, and progressive–relapsing MS subtypes (Milo and Miller, 2014). Of these the relapsing–remitting is the most common clinical phenotype, affecting about 80% of MS patients (Weinshenker et al., 1989). The recurrent and reversible neurological deficits continue for about a decade. During the second decade almost all the patients experience frequent relapses progressing to continuous and irreversible neurological decline (Confavreux et al., 2000).

The classification of MS disease course into the above mentioned clinical subtypes aids in disease understanding and management. Similarly, the heterogeneous MS lesions seen in patient biopsies and autopsies are classified into four categories-Types I, II, III and IV in an effort to understand the MS pathophysiology. This classification is based on patterns of demyelination: loss of myelin protein, pattern of plaques and oligodendrocyte destruction, and immunopathology (Lucchinetti et al., 2000). The destruction of myelin and degeneration of the

underlying axons can occur primarily by two pathological mechanisms: autoimmune and neurodegenerative. First, the hallmark perivenular inflammatory MRI lesions that include Type I and II lesions are thought to be due to an autoimmune response against myelin. The autoimmune hypothesis with T-cells as major players is widely recognized. The second form of pathology occurs due to the loss of myelin generating oligodendrocytes (type III and IV lesions) in absence of inflammatory cellular response (primary oligodendrogliopathy). This is noted as the second most common form of demyelination in MS patients. Such demyelination accounts for about 40% of MS lesions, and are classified as type III lesions (Lucchinetti et al., 2000). Since the type III MS lesions are non-inflammatory in nature they do not respond to the conventionally used immunosuppressive drugs. Furthermore, the progressive irreversible phase of MS is also non-responsive to immunosuppressive therapy, where primary oligodendrogliopathy could be the leading cause of demyelination (Maggs and Palace, 2004). Therapies that could rescue oligodendrocytes might be effective in rescuing or slowing down the MS progression. Also, there is a clinical need to develop MRI methods that could differentiate between demyelination incurred either by the inflammatory autoimmune response or the primary oligodendrogliopathy. One of the approaches towards this end is development of an *in vivo* myelin specific marker, which is likely to assist in (1) monitoring of disease progression, (2) early detection and treatment planning, and (3) insight in disease mechanisms. My thesis addresses these needs by comparing the specific sensitivities of two quantitative MRI methods to myelin in a lipopolysaccharide (LPS) induced rat model of MS, with demyelination presented as type III lesions. In the following sections, I introduce the basic MRI principles and techniques to provide sufficient background for understanding the work presented in this thesis.

Magnetic Resonance Imaging (MRI)

The first report of reconstructing a proton spin density map (i.e. an image of the water distribution) using nuclear magnetic resonance (NMR) was made by Lauterbur in 1973 (Lauterbur, 1973). In the same, year Mansfield and Grannell independently demonstrated the Fourier relationship between the spin density and the NMR signal acquired in the presence of a magnetic field gradient (Mansfield and Grannell, 1973). These seminal papers laid the theoretical foundations for current clinical and research MR imaging methods.

Brief overview of the principles of MRI

MRI is primarily based on the interaction of the hydrogen nuclei (protons) with the external magnetic fields. These hydrogen nuclei are the most abundant in body and present in all tissues and fluids. However, not all protons in the tissue are alike. Most of the protons are present in water molecules and a smaller number are present in macromolecules. The milieu significantly affects the magnetic properties and diffusion of protons. MRI techniques based on the interaction between water and macromolecular protons, and the water diffusion influenced by macromolecular structures such as myelin is the subject of this thesis.

MRI involves coordination of three applied magnetic fields: the strong polarizing magnetic field (B_0), the oscillating radio frequency (RF) field (B_1), and the spatial magnetic field gradient (G). When a spin is placed in an external magnetic field, the torque acting on the spin leads to precession of spin around the net magnetic field at a Larmor precession frequency given by

$$\vec{\omega} = \gamma \vec{B}$$

Where $\vec{\omega}$ is the Larmor precession frequency, γ is the gyromagnetic ratio, and $\vec{B}$ is the external magnetic field at the location of the spin. This relation expresses the fact that the spin precession frequency is proportional to the local magnetic field strength (~B_0). This precession of magnetization induces signal (in the radiofrequency range) in the detector coil; the greater the precession frequency the stronger the signal. As the precession frequency depends on the external magnetic field strength, there is motivation to use higher B_0. The gyromagnetic ratio is unique for each nuclei. Hydrogen protons, apart from being the most abundant nuclei in the body, possess one of the highest gyromagnetic ratios, which make hydrogen proton particularly suitable for MRI.

Relaxation

Relaxation can be defined as the process by which the spins return to the Boltzmann equilibrium state following a perturbation. At equilibrium the longitudinal magnetization is M_0 ($\boldsymbol{M_z = M_0}$) and the equilibrium transverse magnetization is zero($\boldsymbol{M_{xy} = 0}$). The relaxation processes, longitudinal and transverse, are commonly modeled as mono exponential decay to their equilibrium values, respectively.

T_1 relaxation

The restoration of the longitudinal equilibrium magnetization is characterized by the longitudinal or spin-lattice relaxation time constant T_1. The T_1 recovery of longitudinal magnetization after a saturation pulse is described by

$$\boldsymbol{M_z(t) = M_0\left(1 - e^{\frac{-t}{T_1}}\right)}$$

T_2 relaxation

The disappearance of transverse magnetization as the spins dephase (lose coherence) is described by the transverse or spin-spin relaxation time constant T_2. The T_2 decay of Transverse magnetization after an excitation pulse is described by

$$\boldsymbol{M_{xy} = M_0\left(e^{\frac{-t}{T_2}}\right)}$$

However, in presence of inhomogeneous B_0, the signal decays faster due to the spread in the spin precession rates. Thus, the new decay constant T_2^* is:

$$\boldsymbol{\frac{1}{T_2^*} = \frac{1}{T_2} + f(B_0)}$$

The following relation holds true.

$$\boldsymbol{T_2^* \leq T_2 \leq T_1}$$

The **Bloch Equation** describes the evolution of magnetization, including relaxation effects, when an imaging sample in the presence of a magnetic field.

$$\mathbf{\frac{d\vec{M}}{dt} = \gamma\vec{M} \times \vec{B}_{eff} + \frac{1}{T_1}\left(\vec{M}_0 - \vec{M}_z\right) - \frac{1}{T_2}\vec{M}_{xy}}$$

Where, $\vec{\mathbf{M}}$ is the net magnetization; $\vec{\mathbf{B}}_{\mathbf{eff}}$ is the effective magnetic field at the location of the spin; $\mathbf{T_1}$ is the longitudinal relaxation rate; $\vec{\mathbf{M}}_{\mathbf{0}}$ is the initial magnetization; $\vec{\mathbf{M}}_{\mathbf{z}}$ is the longitudinal

magnetization in the direction of polarizing field B_0. $\mathbf{T_2}$ is the transverse relaxation, and $\vec{\mathbf{M}}_{\mathbf{xy}}$ is the transverse magnetization.

The Bloch equation can model spin behavior for conventional imaging methods; however, additional terms are needed to model MT and diffusion effects.

A MRI pulse sequence can be viewed as a combination of RF pulses and gradients in presence of strong B_0 magnetic field. In many cases the method of spatial encoding and the pulse sequence (RF pulses) are independent, and hence we can discuss the pulse sequence sensitivities separately. Practically all sequences produce signal proportional to proton density; however an additional biophysical weighting on the measured signal are important contributions to the image and contrast modulations. This unique quality of contrast tuning is responsible for the wide range of applications for MRI.

Conventional MRI methods

Conventional MRI contrast methods include T1, T2 and proton density (ρ) weighted images. These provide excellent soft tissue contrast and thus have been used extensively in clinical MR. As many different brain pathologies can give rise to similar appearing lesions in an MR image, the high brain pathological sensitivity of these methods also brings in low specificity towards underlying brain pathologies. For adults there is not a fixed relationship between relaxation time-weighting and myelination.

However, conventional T1- weighted and T2-weighted imaging have been used extensively in studies of myelin development in newborn and young children (Barkovich, 2005; Henkelman et al., 2001). There is consensus in the literature today that T1 relaxation is primarily determined by water content (Fatouros et al., 1991; Kamman et al., 1988). Using T_1-weighted imaging to assess myelin content implicitly assumes that the only non-aqueous tissue added in developing brain is myelin. Conventional T1-weighting and T2-weighting should be considered a qualitative measure of myelination and has limited application for subjects older than 2 years of age.

Conventional imaging methods used for MS

The past three decades have seen a steady increase in the role of MRI for MS diagnosis (McDonald et al., 2001; Polman et al., 2011; Polman et al., 2005a; Young et al., 1981). The first use of MRI in MS patients by Young and colleagues (Young et al., 1981) demonstrated the high sensitivity of MRI over X-ray computed tomography. Since then MRI has become the most prominent imaging modality for MS due to the excellent soft tissue contrast and non-invasive nature. In 2001, MRI was included in the diagnostic criteria of MS (McDonald et al., 2001).

Clinical diagnosis of MS is made after careful consideration of neurological examination, patient history, blood test, and occasionally CSF examination. Since the deployment of clinical MRI systems in the late 1970s, MRI has emerged as a leading modality with an integral role in the accurate and early MS diagnosis, and monitoring disease activity. The guidelines for diagnostic criteria of MS are *ad hoc* and have been addressed by several publications, revised over the years to simplifying the criteria and improve the sensitivity while retaining specificity for MS. The most recent panel on Diagnosis of Multiple Sclerosis determined MRI of central nervous system

could support, supplement and even replace certain clinical criteria necessary for diagnosis (Barkhof et al., 1997; Filippi, 2011; McDonald et al., 2001; Polman et al., 2011; Polman et al., 2005a). Clinical diagnostic criteria has three major components 1) dissemination in space (DIS), 2) dissemination in time (DIT), and 3) absence of any evidence for other possible diagnosis than MS. Interpretation is based on the location, size, and progression of MS lesions.

MRI can clearly demonstrate multiple aspects of MS pathology. MS lesions are seen to have an acute or early inflammatory phase followed by focal loss of oligodendrocytes, with axonal loss seen in chronic or late stage lesions. The early inflammatory phase in MS is accompanied with the breakdown of blood brain barrier and is seen as signal enhancement in post contrast images after intravenous administration of gadolinium contrast agent. The excellent tunability of MRI contrast allows sequences to emphasize various tissue properties. On T1 weighted images the water with its long relaxation time appears hypointense (dark) while fat and normal white matter with shorter T1 appears bright. Chronic MS lesions appear as hypointense regions on pre-contrast T1-weighted images that signify tissue volume loss and are known as “black holes”. On other hand, in T2-weighted sequences tissue components with longer T2 such as inflamed MS lesions appear bright. The fluid attenuated inversion recovery (FLAIR) sequence is useful in visualizing the lesions located near the CSF rich structures such as the ventricles. The proton density weighted (PD) sequences provide contrast influenced by proton concentration in tissue. Fewer protons lead to hypo intensity and inflamed lesions with higher protons appear hyper intense.

In recent years, there has been considerable attention to the gray mater involvement in MS, which is difficult to image on conventional MR imaging. High field strength imaging may improve

their detection. In a study involving 15 clinically definite MS patients, the number of lesions detected on a 4T scanner were about 1/3 greater than that observed at 1.5T scanner (Keiper et al., 1998). Similarly, volume quantification also benefits with higher field strength (Sicotte et al., 2003). As such, increasing field strength results in greater sensitivity to lesion detection and lesion volume quantification.

Limitations of conventional MRI imaging methods

Although significant advances have been made to improve conventional MRI methods, they still lack pathological specificity. This is especially relevant for MS, with high levels of heterogeneity and multiple pathological processes occurring simultaneously and with limited access to brain tissue (autopsy and biopsy) samples during different stages of disease development.

Myelin and MRI techniques for assessment of Myelin

In the CNS, oligodendrocytes (a subtype of glial cells) produce the protective myelin sheath, around the axons of neurons, as an extension of their cell membrane. Myelin is mainly found in the white matter (WM), with much smaller concentrations in gray matter (GM). As a major constituent of WM, myelin contributes to about 50% of its dry weight, and gives WM its characteristic white color. Myelin has a complex ultrastructure and assembly, with approximately 80% lipid and 20% protein content (Norton and Autilio, 1966; Obrien and Sampson, 1965). The non-aqueous protons of myelin macromolecules are difficult to image directly because, (1) the transverse magnetization signal decays to zero in a few tens of micro seconds and (2) the signal from protons in myelin is indistinguishable from that arising from protons in other non-aqueous constituents of CNS tissue. Many approaches have been explored in literature to

image myelin directly such as Ultrashort-T_2 imaging (Horch et al., 2011) and indirectly such as Multiexponential-T_2 (MeT2) (MacKay et al., 1994), quantitative magnetization transfer (qMT) (Henkelman et al., 2001), diffusion tensor imaging (DTI) (Song et al., 2002), and qSusceptibility (Liu et al., 2011).

Magnetization Transfer Imaging (MTI)

In 1989, magnetization transfer imaging (MTI) was introduced by Wolff and Balaban (Wolff and Balaban, 1989) as a MR technique enabling measurements that extend beyond those of conventional imaging methods, such as proton density (**PD**), $\boldsymbol{T_1}$, $\boldsymbol{T_2}$, and $\boldsymbol{T_2^*}$. As discussed earlier, MRI is mainly based on mobile water protons. The biological protons mainly reside in water molecules, but a small and less mobile fraction is also present in macromolecules, such as lipids and proteins. The magnetization transfer (MT) techniques utilize the exchange between these two different proton pools which can be mediated by through space dipole-dipole interactions or labile proton mediated chemical exchange mechanism. MT mechanism provides an additional way to generate unique contrast in MRI, allowing access to the macromolecular protons, which are invisible to the conventional MRI sequences.

Due to the rapid tumbling motion of water molecules, the water protons experience a relatively similar average magnetic field leading to narrow absorption line shape. Thus, water protons (free water proton pool) have relatively longer T_2 values (10's of ms) allowing enough time to play out spatial encoding gradients (of the order of few ms) between excitation and acquisition. On the other hand, the macromolecular protons (bound or semi-solid proton pool), associated with biological membranes and other structures, are less mobile and strongly coupled with each

other, which leads to a broad absorption line shape. Thus, macromolecular protons have T_2 decay times typically of the order of few μs and are too short to be detected directly in conventional MRI. The broad absorption line shape of macromolecular protons compared to that of the free water protons make them highly sensitive to off-resonance RF pulses (up to 10^6 times) (Henkelman et al., 1993; Henkelman et al., 2001). These two proton pools exchange magnetization and are in a dynamic equilibrium state. In equilibrium, the net magnetization exchange between the two pools is zero. Any combination of RF pulses that influence the macromolecular proton pool and mobile liquid proton pool to a different extent, imbalances the established equilibrium between the two pools. Thereby, the magnetization transfer taking place by dipole-dipole interactions and/or chemical exchange between the two pools becomes apparent. This exchange of magnetization between the two proton pools is called magnetization transfer (MT) and can in principle be used to generate MT contrast as the two pools exchange magnetization to attain the equilibrium.

MT methods can be classified into two broad classes (off-resonance and on-resonance) depending on how the established thermal magnetization equilibrium state is disrupted between the mobile free water and bound macromolecular proton pools. The water protons are primary signal sources in the MRI and thus the Larmor frequency of water protons serves as reference for distinguishing on- and off-resonance RF pulses.

(1) Off-resonance MT (steady state)

A RF pulse - which is off-resonance to the free water proton pool but is still on-resonance to the semi-solid macromolecular proton pool - is applied to saturate the broad absorption line of the

macromolecular proton pool. The macromolecular proton pool saturation destroys the dynamic thermal equilibrium established between the two proton pools. Thus the rate of magnetization transfer from free water pool to bound macromolecular pool now exceeds the counterpart, leading to MT effects and saturation of the free water proton pool. This saturation of water proton pool is observed as corresponding reduction in image intensity. No intensity reduction is observed in tissues which do not show MT effects.

(2) On-resonance MT (transient)

When an on-resonance pulse (short duration as compared to T_2) is applied to the free water proton pool, it alters the longitudinal magnetization of water protons and thus disturbs the established equilibrium between the two proton pools. Although the on-resonance pulse to water protons is also on-resonance for macromolecular protons the saturation of macromolecular pool is minimal due to the low power. As the dynamic equilibrium is disturbed there is net transfer of magnetization from the macromolecular pool to free water pool. Thus, the observed free pool magnetization is slightly higher than if MT was absent due to faster recovery rate. The selective inversion recovery (SIR) method for MT used in this thesis is based on modeling of this transient recovery process.

Magnetization transfer ratio (MTR)

MTR is a quantitative measure of MT in tissues that summarizes the MT phenomena in a single value. In 1992, Dousset and colleagues (Dousset et al., 1992) used MTR in clinical study and were first to show the greater sensitivity of MTR in comparison to conventional MRI. Particularly they showed sensitivity to demyelination and furthermore, the ability of MTR to classify myelin loss in MS patients. MTR is also shows greater degree of reproducibility on same scanner and

imaging sequence implementation (Vavasour et al., 2006). The greater sensitivity and specificity of MTR to myelin loss along with the simplicity and ease of implementation led to widespread use of MTR especially in myelin related diseases such as MS.

MTR calculation requires acquisition of two images, one with magnetization transfer saturation pulse, applied off-resonance (typically 1-2 kHz) to the free water proton pool, (M_s), and one without (M_0) used for normalization. MTR is defined as

$$\boldsymbol{MTR = 100\frac{(M_0 - M_s)}{M_0}\ pu}$$

Where pu is percentage unit. MTR is higher in tissue with higher macromolecular content, *e.g.*, white matter MTR is typically between 30-60 pu while MTR for CSF is close to zero with gray matter MTR values lying in between CSF and WM. In demyelinating lesions the MTR values are lower compared to WM of healthy controls (Dousset et al., 1992).

Even though MTR is quantitative as it yields a numerical value, its specificity to demyelination is limited as it depends on the acquisition scheme along with the sample properties, unlike the tissue relaxation time constants T_1, T_2 and other intrinsic tissue properties. Furthermore, MTR values depend on the off-resonance frequencies and mean saturation powers used (Tofts et al., 2006). For example, MTR values in normal WM ranged from 17-50 pu for a frequency range of 1-1.5 kHz (van Buchem and Tofts, 2000). Thus, reproducibility of MTR values in different research settings is a concern, and attempts have been made to increase uniformity of MTR values (Berry et al., 1999b; Silver et al., 1999). Additionally, MT is a complex phenomenon, and

a single value representation is unable to capture aspects with potential clinical value such as the fundamental parameters of the two pool model.

Although a marked reduction in MTR values is seen in MS patients due to demyelination (Dousset et al., 1992; Gass et al., 1994; Ge et al., 2001), concomitant pathologies—such as inflammation and axonal loss—could also affect MTR values. Does and colleagues compared the MTR with T1 and T2 properties in peripheral nerves (Does et al., 1998). The authors found different MT properties for the two short T2 water components but similar MTRs. In an experimental allergic encephalomyelitis (EAE) model of MS, Gareau and co-workers altered inflammation using antibodies. They found that the MTR values were changed with altered inflammatory activity (Gareau et al., 2000). Cook et al found that both demyelination and inflammation reduces MTR values (Cook et al., 2004). These studies highlight the need for myelin-specific quantitative methods, which can differentiate demyelination from co-existing pathologies such as inflammation and gliosis.

Quantitative Magnetization Transfer (qMT)

MT involves interaction between mobile water pool and bound macromolecular pool protons. In brain WM, the majority of macromolecular protons are contributed by myelin, and pathologies such as demyelination are expected to cause a decrease in the macromolecular proton pool of the tissue. The limited ability of MTR to characterize the MT phenomena led to development of qMT methods. Modeling the MT processes may quantify fundamental physical tissue properties such as the macromolecular pool fraction and the exchange rate between the free and bound

proton pools, thus potentially increasing the specificity of MRI to demyelination and other pathologies, which is a major limitation of conventional MRI methods.

qMT characterizes the MT phenomena in tissue by fitting the MRI signal acquired to a mathematical model, which contain the fundamental tissue properties. Thus, qMT provides more detailed information on the MT processes and possibly greater specificity towards pathologies involved. A simpler implementation of qMT is commonly based on a two pool (free proton pool and restricted macromolecular pool) mathematical model of spin exchange. The equations of motion for magnetization are written separately for the two pools and include the exchange terms to model the magnetization transfer. Two-pool model is simple yet sufficient to give quantitative interpretation of MT in WM (Henkelman et al., 1993).

Figure 1-1 describes the two pool MT model. Pool 1 (left) is the free water proton pool. In Pool 1, the total magnetization of the free water proton pool is normalized to 1, of which the longitudinal magnetization is represented by shaded area. The unshaded region represents other magnetization which may be transverse or saturated. Pool 2 (right) corresponds to the restricted semisolid proton pool with size F, determined by the equilibrium longitudinal magnetization in absence of RF pulses. The restricted semisolid pool is similarly divided into longitudinal (shaded) and other magnetization. The longitudinal magnetization recovery rates for each pool are represented by R_{1f} *and* R_{1r} *and* correspond to T_1 relaxation constant for the two pools, respectively, and T_1 governs the recovery of longitudinal magnetization. The rate of loss of longitudinal magnetization in the presence of RF pulses results in saturation, designated as S_f and S_r in pools 1 and 2, respectively. F represents the relative populations of the pools in

steady state and denotes the ratio of free to restricted proton pools. As the relative populations of the pools are in steady state the pseudo-first-order rate constants are characterized by K_r and K_f. In this qMT model there are four relaxation parameters R_{1f}, R_{1r}, T_{2f}, and T_{2r}; two exchange parameters K_f, and K_r; and the corresponding magnetizations of free and restricted pools M_{0f} and M_{0r}. The normalization of free proton pool reduces one free parameter as only the pool size ratio, F, is sufficient to describe the relative pool sizes. The steady state condition requires K_f= F. K_r, thus reducing one more free parameter. Thus there are seven independent parameters and with normalization six. These parameters are properties of system and are independent of sequence. They characterize the MT process completely (Henkelman et al., 1993).

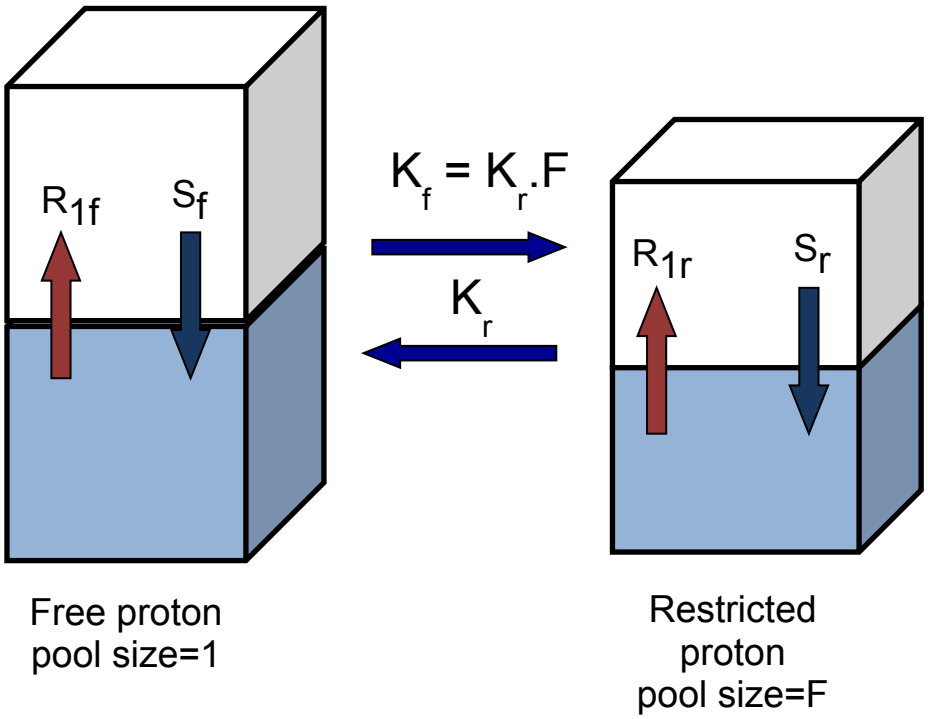

Figure 1-1. The two pool qMT model. Pool1 is free proton pool and pool 2 corresponds to the restricted semisolid proton pool with size F. the subscripts f, and r denote the free water and restricted macromolecular proton pools respectively. The rate of magnetization exchange between the two pools is described by the pseudo-first-order rate constants K_r and K_f. The longitudinal magnetization recovery rates for each pool is represented by R_{1f} *and* R_{1r} correspond to T_1 which govern the recovery of longitudinal magnetization. S_f and S_r denote saturation in pool 1 and 2 respectively. The total number of spins in free pool is normalized to 1. The figure is based on Henkelman et al. (Henkelman et al., 1993).

Selective Inversion Recovery fast spin echo (SIR-FSE) method for qMT measurements

The presence of coupling between the free and semisolid proton pools in a MT system leads to a bi-exponential T_1 recovery. A relatively new qMT method developed by Gochberg and Gore (Gochberg and Gore, 2003, 2007b) was used to acquire qMT data for the project. SIR-FSE is an on-resonance qMT method with an inversion pulse on free water pool and fast spin echo readout. The length of inversion pulse is much longer than T_{2m} and much smaller than T_{2f} and $1/K_{mf}$. The f, and m in subscript denotes free water and restricted macromolecular proton pools, respectively. The inversion pulse affects the free pool and the restricted pool magnetization to different degrees. Specifically, the free pool magnetization is completely inverted, assuming an ideal 180° inversion pulse; the restricted pool magnetization is marginally saturated depending on T_{2r}. The Pulse sequence used for SIR-FSE sequence is shown in Figure 1-2. The SIR-FSE experiment is performed with a series of inversion times and the measured signal is fitted to a bi-exponential recovery model. Following the prescribed analysis (Gochberg and Gore, 2007b) MT parameters such as Pool size ratio (F) and exchange rate, k_{mf} can be extracted.

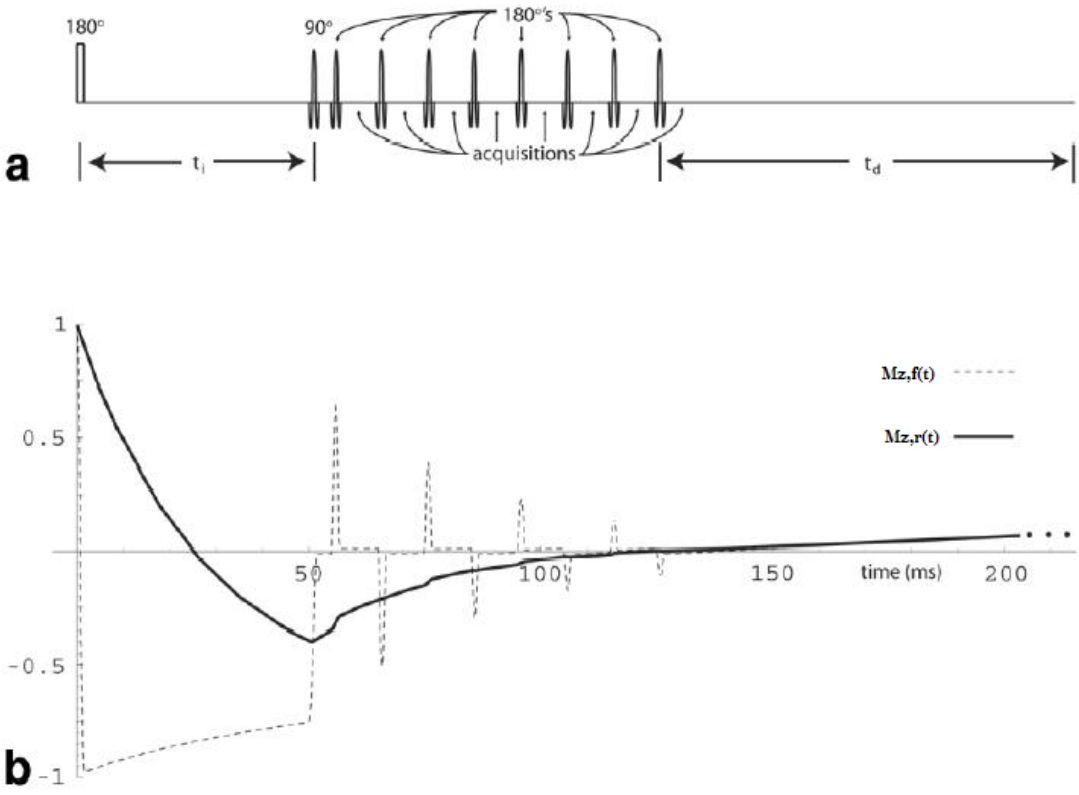

Figure 1-2. Pulse sequence and longitudinal magnetization evolution for SIR-FSE qMT method. a) the pulse sequence; b) the simulated evolution of longitudinal magnetization. Note that after the series of 180°pulses in the FSE acquisition, both the free pool and restricted pool longitudinal magnetization will be zero: $\boldsymbol{M_{z,f}}$ is flipped to transverse plane by the 90°pulse and any attempt to recover is inverted by the series of 180°pulses; $\boldsymbol{M_{z,r}}$ is gradually pulled toward to zero by the saturation of $\boldsymbol{M_{z,f}}$. After a constant time delay $\boldsymbol{t_d}$, both the free pool and restricted pool magnetization evolve as $\left(1 - e^{\frac{-t_d}{T_1^{obs}}}\right)$ towards their equilibrium values (right before the inversion pulse). Figure from Gochberg et al, 2007 (Gochberg and Gore, 2007b).

Diffusion Weighted Imaging (DWI)

The first diffusion measurement in MR was Diffusion Weighted Imaging which was introduced by Stejskal and Tanner in 1965 (Stejskal and Tanner, 1965). These researchers used a simple spin echo sequence (90-180-echo) and added two identical magnetic gradient pulses before and after the 180 RF pulse. The first (magnetic field) gradient pulse serves to encode the spin locations in space, along a single direction determined by the applied gradient, with phase. Subsequently, the second gradient pulse unwraps the additional phase. If the spins were stationary, there would be no residual phase due to applied gradients and no signal loss. If the spins move during the diffusion time (Δ), i.e. the interval between the gradient pulses, there would be a residual phase and a lack of full phase coherence that results in the signal attenuation. This signal attenuation can be used to measure the diffusion. The sensitivity of the sequence to the diffusion is determined by the configuration of these gradients which is summarized by the term, b-value. For example, the b-value increases with higher Δ, which increases sensitivity to motion by allowing more time for spins to diffuse. The b-value also increases with G, the magnitude of gradient, or δ**,** the width of gradient pulse, both of which determine the area of under the gradient pulse. The area under the gradient pulse leads to greater phase accumulation, with smaller displacements, as well as greater signal attenuation due to diffusion. This signal attenuation can be modeled as a single exponential function with an apparent diffusion coefficient, $[\frac{S}{S_0} = \exp(-b.ADC)]$. S and S_0 are the signal measurements with and without the diffusion gradients, respectively. This allows for normalization of signal decay due to T_2 relaxation which would take place during the pulse sequence. Given that the DWI uses intrinsic water spins, it quickly became a popular method to measure water diffusion over then popular methods that utilized dyes and radioactive tracers to measure diffusion [ref].

By the mid-1980's, LeBihan and colleagues incorporated the diffusion measurement in imaging sequences to measure diffusion in human brain tissue (Le Bihan et al., 1986). The intra-voxel incoherent motion (IVIM) in the tissue has contributions from both blood in the capillaries (assumed randomly oriented) within the imaging voxel and the water in the tissue outside the vasculature. Thus, a two compartment mathematical model, with a bi-exponential signal attenuation curve, was proposed to model the signal from the intra- and extra-vascular water. At lower b-values, the signal attenuation is dominated by the intravascular water which can be modeled as a pseudo diffusion coefficient that is relevant for only *in vivo* measurements:

$$\frac{S}{S_0} = x.\exp(-b.ADC_{blood}) + (1-x).\exp(-b.ADC_{tissue}).$$

The diffusion coefficient is very sensitive to tissue injury and drops quickly following tissue insults. For example, ischemic brain injury is detected in diffusion weighted images 2-3 hours prior to changes in T_2 weighted images (Moseley et al., 1990). However, the bi-exponential signal attenuation is also observed in single compartmental studies (Sehy et al., 2002), thus a careful interpretation of the signal origin is necessary before reaching any conclusion on the validity of the models discussed above. DWI is used to measure diffusion co-efficient. In anisotropic tissue, the diffusion coefficient is dependent upon the direction of the applied gradient (Hansen, 1971). Thus, a more complex model is needed to characterize diffusion in anisotropic tissues, such as white matter found within the CNS (Figure 1-3).

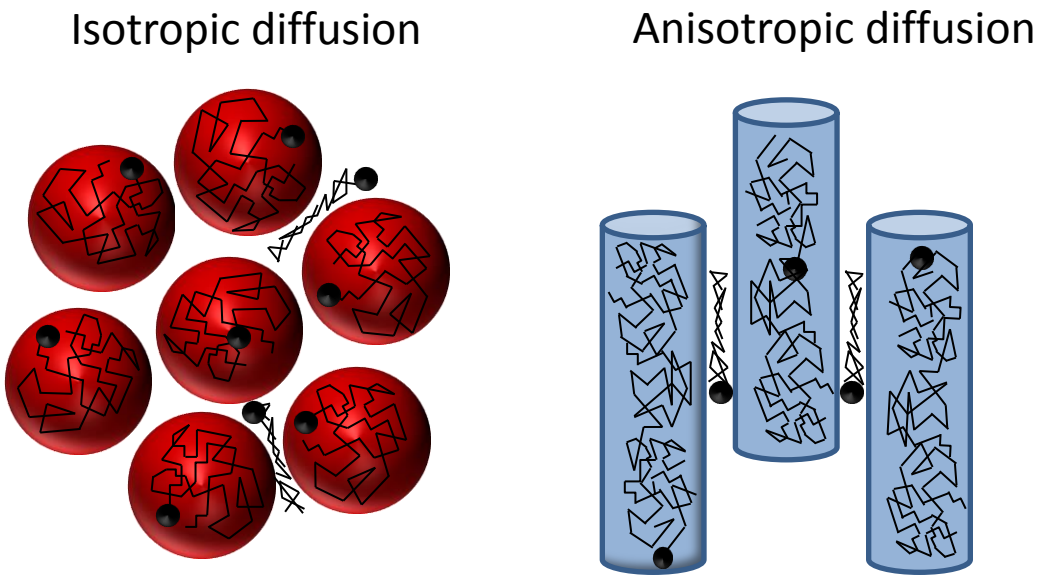

Figure 1-3. An illustration of isotropic and anisotropic diffusion in tissue. In Isotropic diffusion (right) milieu the mean diffusion displacements are similar in all direction, where as in case of anisotropic diffusion (left) the mean diffusion displacement are not similar in all direction e.g. greater along the nerve fibers compared to perpendicular direction.

Diffusion Tensor Imaging (DTI)

DTI provides a more complex framework to characterize anisotropic diffusion in tissue (Basser et al., 1994a, b). DTI is a prominent imaging technique that is often used for white matter evaluation (Assaf and Pasternak, 2008). It is sensitive to microstructural changes in tissue that are orders of magnitude smaller than the imaging resolution and, thus, can be used to make meaningful inferences under the assumption that the microstructural order extends to spatial scales of voxel dimensions. Diffusing water molecules probe tissue on a microscopic scale, which is orders of magnitude smaller than MRI voxels (mm's in size). Thus, if the underlying tissue microstructure within the imaging voxel is truly inhomogeneous and unordered, the information will be lost in averaging over the scale of a voxel. However, to observe anisotropy at the macroscopic level in voxels of DTI images, the anisotropy needs to be present at the microscopic level extending to macroscopic scale along with a level of coherence in structure.

As described by Stejskal and Tanner (Stejskal and Tanner, 1965), the diffusion weighted signal for an imaging voxel can be expressed as:

$$S = S_0 e^{-\gamma^2 G^2 \delta^2 \left(\Delta - \frac{\delta}{3}\right) D} = S_0 e^{-b(ADC)}$$

Where S_0 is the signal intensity without diffusion weighting, γ is the gyromagnetic ratio, *G* is the strength of the linear gradient, δ is the length of the gradient, Δ is the time interval between the two gradients, and ADC is the apparent diffusion constant. If we apply the diffusion weighted gradients in different combinations of phase encoding (x), readout(y), and slice selection (z) directions, then we can calculate the diffusion tensor according to equation:

$$S = S_0 e^{-b\, \boldsymbol{n}^T \boldsymbol{D}\, \boldsymbol{n}}$$

In which $\boldsymbol{D} = \begin{bmatrix} \boldsymbol{D_{xx}} & \boldsymbol{D_{xy}} & \boldsymbol{D_{xz}} \\ \boldsymbol{D_{yx}} & \boldsymbol{D_{yy}} & \boldsymbol{D_{yz}} \\ \boldsymbol{D_{zx}} & \boldsymbol{D_{zy}} & \boldsymbol{D_{zz}} \end{bmatrix}$ is the diffusion tensor. **n** is a unit vector representing the encoding direction of applied diffusion gradient (Basser and Pierpaoli, 1996). Diffusion Tensor imaging relies on the assumption that the diffusing water molecules follow the Gaussian distribution profile, this is true for freely diffusing water molecules but in tissue where diffusion of water molecules is hindered and restricted by obstacles and boundaries the assumption of Gaussian profile is no longer valid and thus the diffusion constant measured is referred to as apparent diffusion constant. DT models the diffusion as an ellipsoid. The three principal eigenvectors determine the orientation of the ellipsoid and the three Eigen values define the shape of diffusion ellipsoid, total six independent components. The DT is calculated using the diffusion weighted measurements along at least six independent directions. DT has 9 different elements, although the diagonal elements D_{xx}, D_{yy} and D_{zz} represent the diffusion constant along the x, y and z axis respectively. The off diagonal terms such as D_{xy}, D_{yz} and D_{zx} do not have direct interpretation as diffusion constants along certain direction and carry information about the rotations and thus the orientation of diffusion ellipsoid.

The three eigenvalues of this diffusion tensor $\lambda_1, \lambda_2, \lambda_3$ $(\lambda_1 \geq \lambda_2 \geq \lambda_3)$ and corresponding eigenvectors ($\boldsymbol{v}_1$, $\boldsymbol{v}_2$, $\boldsymbol{v}_3$) can be derived by matrix diagonalization. DTI parameters can be calculated from these eigenvalues:

The radial diffusivity (RD): $\lambda_{\perp} = (\lambda_3 + \lambda_2)/2$

The axial diffusivity (AD): $\lambda_{\parallel} = \lambda_1$ (λ_1 is the largest eigenvalue)

The relative anisotropy: RA = $\frac{\sqrt{(\lambda_1 - Tr/3)^2 + (\lambda_2 - Tr/3)^2 + (\lambda_3 - Tr/3)^2}}{\frac{Tr}{\sqrt{3}}}$

The trace: $Tr(D) = \lambda_1 + \lambda_2 + \lambda_3$

The fractional anisotropy: $FA = \frac{\sqrt{3}\sqrt{(\lambda_1 - Tr/3)^2 + (\lambda_2 - Tr/3)^2 + (\lambda_3 - Tr/3)^2}}{\sqrt{2}\sqrt{\lambda_1^2 + \lambda_2^2 + \lambda_3^2}}$

Thesis overview

In this chapter, we briefly reviewed the clinical presentation of MS, the role of conventional MRI methods currently utilized for MS diagnosis, as well as, the quantitative MR (qMR) methods used in our study to examine an animal model of type III MS lesions. The qMRI methods described above, i.e. qMT and DTI, were used to assess their relative specific sensitivity to myelin through quantitative comparison with histology– the gold standard for MS pathological assessments. This comparative validation, we hoped, would serve as a guideline for the choice of quantitative methods employed for the assessment of MS-related demyelination in clinical settings.

To this end, in Chapter 2 we investigated the *in vivo* specific sensitivity of qMT and DTI methods to myelin in an animal model of type III MS lesions. The key results from this study indicated a greater sensitivity of PSR (qMT) to myelin as compared to all other qMRI parameters, from qMT and DTI, in combined GM and WM analyses. The results of this study suggest that the qMT parameter, PSR, may be better suited to assess *in vivo* myelin content. However, a major limitation of our study was that we could not quantify demyelination within WM due to loss of experimental precision. Thus, for our subsequent study (Chapter 3) we addressed the sources for these experimental uncertainties that confounded the true physiological relationships between qMR parameters and histological myelin content. Our results from this chapter supported our conclusions in Chapter 2 and more strongly demonstrated the ability of PSR to quantify degrees of WM demyelination in MS-related lesions. In our final chapter, Chapter 4, we summarized the overall findings of our results as well as possible experimental directions.

CHAPTER II

IN VIVO qMT AND DTI IMAGING IN AN ANIMAL MODEL OF MULTIPLE SCLEROSIS

Introduction

As mentioned in the Introduction, this work aims to determine the specific sensitivities of novel magnetic resonance imaging (MRI) methods for *in vivo* myelin detection, in an attempt to develop more robust tools for myelin evaluation under normal and pathological conditions. One such pathological process is multiple sclerosis (MS), the most common demyelinating disease of the brain and one of the most frequent causes of non-traumatic neurological disability in adults. Within the United States, MS is estimated to affect 400,000 individuals, with over 2 million individuals affected worldwide (Hauser, 1994; Noseworthy et al., 2000; Weinshenker, 1996) Of particular note, this disease is characterized by a number of debilitating neurological deficits that significantly affect the patient's quality of life. For example, 50% of patients are non-ambulatory 25 years after the disease onset (Trapp and Nave, 2008). As such, it is particularly important to understand the pathophysiology of MS to alleviate cost and global disease burden within this diseased population (World Health Organization).

Though the causes of MS are unknown, its accurate and timely clinical diagnosis is highly dependent upon the identification of classical clinical symptoms and indicators of MS, one of

which is white matter (WM) lesions within the central nervous system (CNS) (Poleman 2011, Valk and Barkhof. Chapter 79. *Clinical Features and Laboratory Investigations*). Histological examinations aimed at understanding the clinical features of MS revealed that MS-related lesions are highly heterogeneous and largely consist of demyelinated plaques within the cerebral WM, in addition to axonal damage, inflammatory infiltrates, and gliosis (Lassmann et al., 2001; Lucchinetti et al., 2001). Furthermore, the extent of axonal injury, inflammation, and the degree of demyelination also varies within lesions and between MS patients, thus making this disease particularly complex in its diagnosis and treatment (Lassmann et al., 2001). MS lesions could be categorized into four distinct types (types I-IV) based on pathological features such as its associated demyelination patterns. Though these histological examinations of MS lesions allow further insight into disease pathogenesis and pathology, these methods are highly invasive and, thus, are largely performed postmortem. As a result, the utility of this approach for timely disease identification and treatment is very limited.

Over 33 years ago, Young and colleagues (Young et al., 1981) introduced the use of an *in vivo* brain-imaging tool, MRI (then nuclear MRI) to identify MS-related WM abnormalities and demonstrated the unique sensitivity of MRI over X-ray computed tomography (CT). In this study, a significantly greater number of lesions was detected on MRI with clearer margins as compared to CT. In addition, these authors demonstrated that lesions observed in MRI correlated with clinically identified areas of abnormality, thus satisfying the diagnostic criteria for MS. By doing so, Young and colleagues revolutionized the diagnostic methods for MS (Young et al., 1981). Since then, MRI has emerged as the most prominent —often the only— needed imaging modality, with high positive predictive power, for MS diagnosis. MRI usage as a diagnostic tool is particularly critical as it permits the evaluation of MS-related WM abnormalities

in space and time. Furthermore, this *in vivo* evaluation allows for early clinical interventions in form of treatment, assessment, and monitoring for MS. This process may ultimately slow the progression or even prevent permanent neurological injury. Unfortunately, as there is no known cure, this approach serves as the best treatment paradigm for this disease (Inglese, 2006). To this end, MRI has revealed multifocal cerebral WM abnormalities in 95% of clinically identified MS patients (Compston and Coles, 2002; Rovira-Canellas et al., 2000). Though these conventional MRI studies lack the specificity to determine the pathological characteristics of these WM abnormalities, these results correlated with earlier histological examinations and indicate that *in vivo* identification of WM lesions may serve as a reliable and accurate biomarker for MS pathology.

Of further note, similar studies have shown that demyelination is a central feature of MS pathology. Myelin is a layered structure, composed of 80% lipid and 20% protein, that ensheaths axons within the central nervous system (CNS) (Quarles R, 2006). Myelin facilitates efficient and fast transmission of electrical signals and, by doing so, promotes efficient signal transmission between neurons. Furthermore, the myelin and axons are closely interlinked structurally and functionally, thus any damage to either often leads to damage in the other (Simons et al., 2014). Thus, given its critical functions, myelin loss (i.e. demyelination) and axonal damage results in severe physical and neurological disabilities.

Demyelination is a central feature in many CNS diseases, with multiple sclerosis (MS) being the most common (Noseworthy et. al. 2000, Frohman et. al. 2003, Evans et. al. 2013). Thus, demyelination is an attractive pathological feature to use as a biomarker for MS pathology. Though the current MRI techniques are sensitive to enumerating MS-related WM abnormalities,

they lack the specificity towards determining the lesion type and the underlying pathology of the MS-related lesion (for example, the presence and extent of demyelination) (Wayne Moore GR 2003). Therefore, development of an *in vivo* myelin-specific marker is likely to assist in: (1) monitoring disease progression, (2) early detection and treatment planning, and (3) providing insight into disease mechanisms.

To this end, the work presented in this chapter examines the *in vivo* myelin sensitivity of two quantitative MRI methods: 1) quantitative magnetization transfer (qMT) and 2) diffusion tensor imaging (DTI) using an animal model of type III MS WM lesions. We are using these two *in vivo* imaging approaches as they provide a quantitative assessment of WM damage beyond conventional MRI. Unlike conventional MRI methods, qMT and DTI are model based MRI methods that provide quantitative metrics sensitive to the sub-voxel tissue integrity, composition, and structure. These methods are based on different physical principles and tissue model assumptions. While qMT quantifies the macromolecular content and its interaction with water, DTI is sensitive to tissue microstructures and quantifies the anisotropic diffusion that diffusing water molecules experience while they probe the surrounding tissue microstructure. Myelin is a macromolecule and a primary contributor to MT contrast in brain[]. While its “jelly-roll” like structure -encapsulating elongated axons in white matter fibers- restricts the water diffusion perpendicular to the axonal orientation, thereby contributing to diffusion anisotropy. The resulting quantitative metrics, specifically pool size ratio (PSR) from qMT and radial diffusivity (RD) from DTI, have been shown to be particularly sensitive to myelin [Song 2002, 2005; Klawiter 2011; Janve 2013, Ou 2009, underhill 2011, Schmierer 2007].

As such, these two methods yield fundamental quantitative tissue parameters that can be compared across MS patients. These methods have been developed to improve upon the limited specificity of conventional MRI. Many studies have found that qMT and DTI parameters such as PSR, RD, and AD have pathological specificity towards MS-related pathological conditions such as the extent of demyelination and axonal damage (Ou 2009, Song 2005, etc.). A quantitative validation of the specific sensitivities of PSR and RD to myelin would contribute to the understanding of MS-related WM pathology and may assist in the development of an ideal myelin biomarker. As such, our aim is to correlate quantitative imaging measures, derived from qMT imaging and DTI, with histology in order to validate and quantify the ability of qMT and DTI to characterize demyelination under the pathological conditions found in a type III animal model of MS.

In this investigation, we used an animal model of type III MS lesions which represent 26% of observed lesions in MS patients (Lucchinetti C, Bruck W, Parisi J et al 2000). In our study, the lesions were induced in the corpus callosum (CC)— the largest cerebral commissure that acts as a major white matter (WM) pathway, connecting and facilitating communication between homologous structures in both hemispheres of the brain (Siffrefi 2013; Paul 2011; Llufriu et al Saiz 2012). We chose this brain region because the CC is commonly targeted in MS pathology and frequently demonstrates focal demyelinating lesions in the early stages of the disease (Audoin B, Ibarrola D, Malikova I et al 2007). Furthermore, it is thought that this MS-CC damage precipitates the physical disability and early cognitive impairments of MS (Llufriu et al., 2012). As will be discussed later in this Chapter, we first examined the focal lipopolysaccharide (LPS)-induced CC lesions using qMT and DTI parameters and subsequently correlated these experimental results with the histopathological examinations of type III lesions in our MS rodent

model. More specifically, correlations of the qMT metric pool size ratio (PSR) and the DTI metric radial diffusivity (RD) with myelin histology were carried out, as PSR and RD are putative MRI markers of myelin. Thus, changes in these metrics may act as a biomarker MS-related demyelination. This represents a novel experimental approach to validate the sensitivity of qMT and DTI using quantitative myelin histology.

Methods

Study design (Figure 2-1): As mentioned earlier, LPS injections in the CC reproduce the demyelination observed in MS lesions. Thus for this study rats from the same litter were randomly assigned for injection with either LPS or saline (control) in the CC (as described in detail in section below).

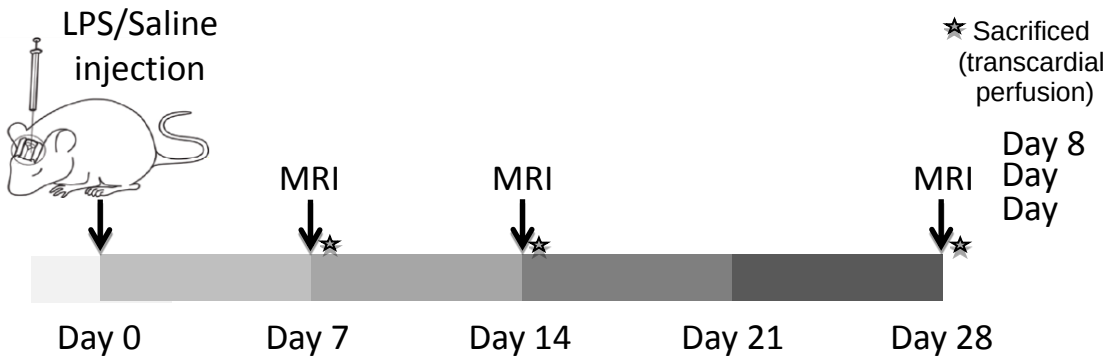

Figure 2-1. Experimental timeline showing the procedures performed at three post injection time points: Day7, Day14, and Day28. Three animals were injected (2LPS, 1Saline) for each time point and; Structural MRI scans followed by qMT and DTI scans were performed before animals were sacrificed for histology.

Animal model

Animal preparation and histological processing were performed in collaboration with the research group led by Dr. Subramaniam Sriram in the Neurology Department, located at Vanderbilt Stallworth Rehabilitation Hospital of Vanderbilt University.

Nine female Sprague–Dawley rats, two months old and weight of about 200 g were used for study. Animals were allowed at least one week of acclimation period and no manipulations were performed during this period. Animals were housed in facility with a 12h light/dark cycle with food and water ad libitum. All experiments were performed in accordance with IACUC and NIH guidelines for animal care and use.

Injection of lipopolysaccharide (LPS) into the central nervous system (CNS) white matter in the spinal cord results in the development of an acute inflammatory response followed by demyelination. Rats were intracerebrally injected with LPS or saline. Three of them were injected with saline, and six with LPS. For injection, rats were anesthetized by 2% isoflurane and positioned in a small animal stereotaxic apparatus (David Kopf Instruments, Tujunga, CA) to conform to a brain atlas (Pellagrino, 1979). The hair was cleared from top of the injected brain region, and exposed skin was cleaned by alcohol and iodine solution before incision to expose the skull. Microinjection of LPS (Escherichia coli serotype 055:B5) into the corpus callosum was performed by injection at the following coordinates: 1 mm posterior from Bregma, and 1 mm lateral the sagittal sutures of the skull, and 3.3-3.5mm below the dura matter. A high-speed drill was used to penetrate the skull by drilling a hole with 1 mm diameter. Microinjection was performed with a 32-gauge needle inserted through the hole on the skull. Saline controls received 5 µl of PBS (Phosphate buffered saline) solution while LPS treated rats were injected with 5 µl of PBS containing 5 µg of LPS. Injections were performed with a Hamilton Syringe operated by a microinjection pump. Injections were performed over 15 min duration to allow

ample time for LPS to diffuse into the corpus callosum and the needle stayed inside the brain for an additional 10 minutes before being pulled out gently to avoid unintentional removal of the injected LPS/Saline solution before it diffuses. After injection, the skin incision was carefully sutured. Bitter apple and topical lidocaine were applied to the wound and the rats were allowed to gradually recover from anesthesia before returning to the cage.

The rats were divided in three groups of three rats each with one Saline and two LPS treated rats for imaging at three different time points.

MRI

In vivo MRI experiments were performed on the rats at 7, 14 and 28 days after the injection on a Inova 7 Tesla scanner with a 160 mm bore, actively shielded gradients of 27 G/cm, and rise times of 100 µs. A 38 mm quadrature volume coil was used to transmit and receive RF signal.

Rats were anesthetized by isoflurane (2-chloro-2-(difluoromethoxy)-1,1,1-trifluoro-ethane, a halogenated ether) 4-5% for induction and 2% for maintenance. Body temperature was kept at 37°by supplying hot air flow, measured with a rectal temperature probe, and the respiration rate of rat was monitored and maintained at 40-55 breaths per minute by slight adjustment of the isoflurane level.

T2 weighted (T2w) fast spin echo images were used to determine the brain geometry, to select an axial imaging slice (perpendicular to the corpus callosum), and to identify the needle track to indicate the site of injection.

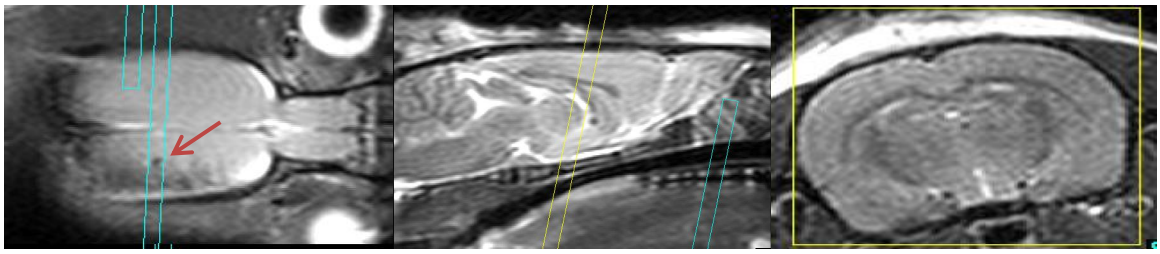

Figure 2-2. MRI slice selection procedure. Representative single slice *in vivo images,* from T2w FSE multislice acquisition, in orthogonal orientations a) coronal, b) sagittal and c) axial plane used to locate the injection site. Cyan and yellow boxes indicate the slice prescription for single slice qMT and multislice DTI acquisition. Above image is representative for cases where the needle track is not clearly visible in axial sections. However, notice the damaged region is clearly visible in coronal section indicated by red arrow.

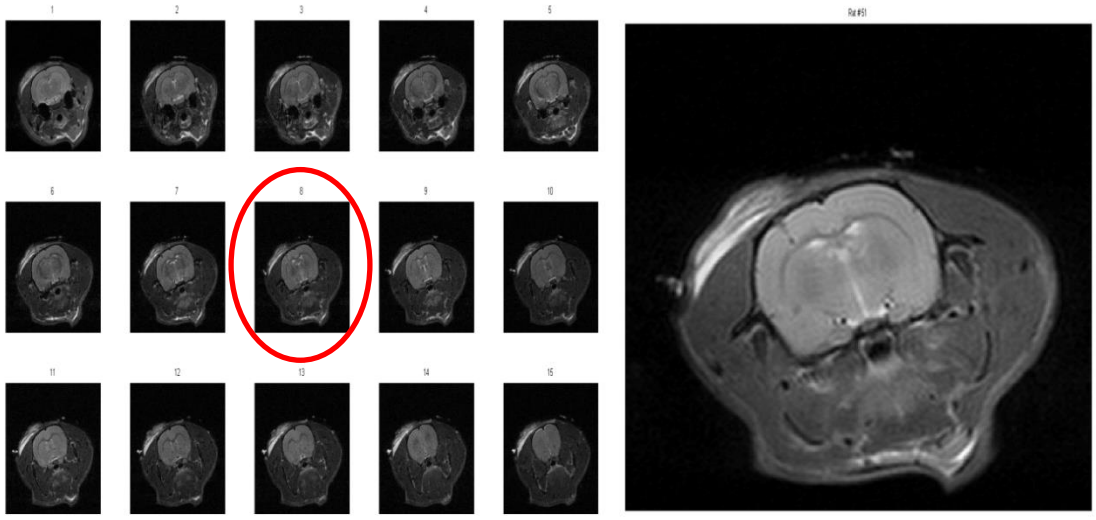

Figure 2-3. MRI slice selection procedure for qMT and DTI acquisition. (a) Typical serial T2 weighted multislice FSE images revealing anatomical details and extent of damage in CC to accurately place the selected slice, and (b) selected slice containing needle track (tissue damage is clearly visible). Figure illustrates representative case where the needle track is clearly visible in axial section.

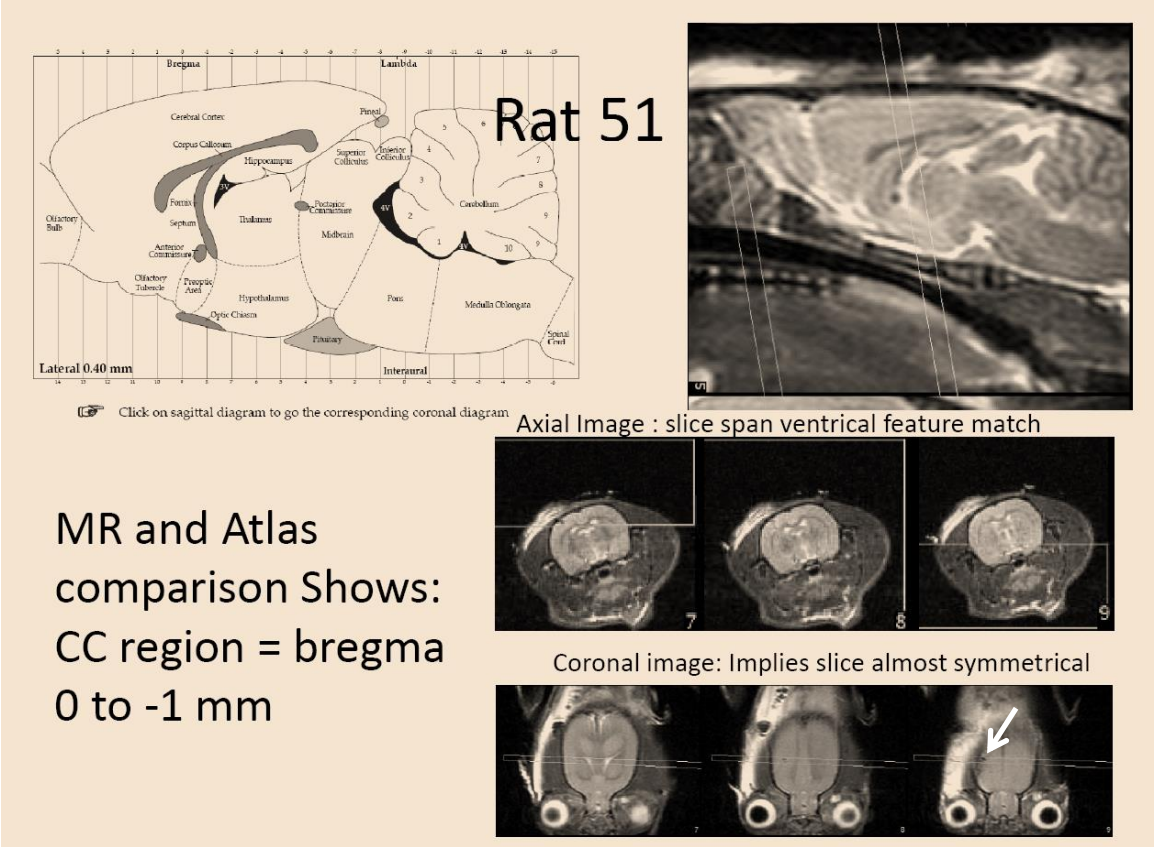

Figure 2-4. MRI selected slice and atlas comparison. a) Sagittal view from rat brain atlas through midline, b) corresponding T2 weighted multislice FSE image through midline c),d) illustrate the symmetrical placement of MRI slice plan for qMT and DTI acquisition about midline indicated by yellow rectangles. Note that the planned slice and the track created by needle damage may not be aligned, indicated by red arrow.

For the QMT study, a fast spin echo sequence with a 1 ms hard inversion pulse was used. 22 images with inversion times ranging from 4 ms to 6 s were obtained with a 2.5 s constant pre-delay, 2 averages, 8 echoes, 10 ms echo spacing time, 35 mm by 35 mm field of view, 1 mm thick slice, and 128x128 data matrix (zero-filled to 256x256) (see Figure 2-5). The total imaging time was about half an hour. Data were fitted to a bi-exponential function of the inversion times to determine QMT parameters pixel-by-pixel (Gochberg and Gore, 2007b).

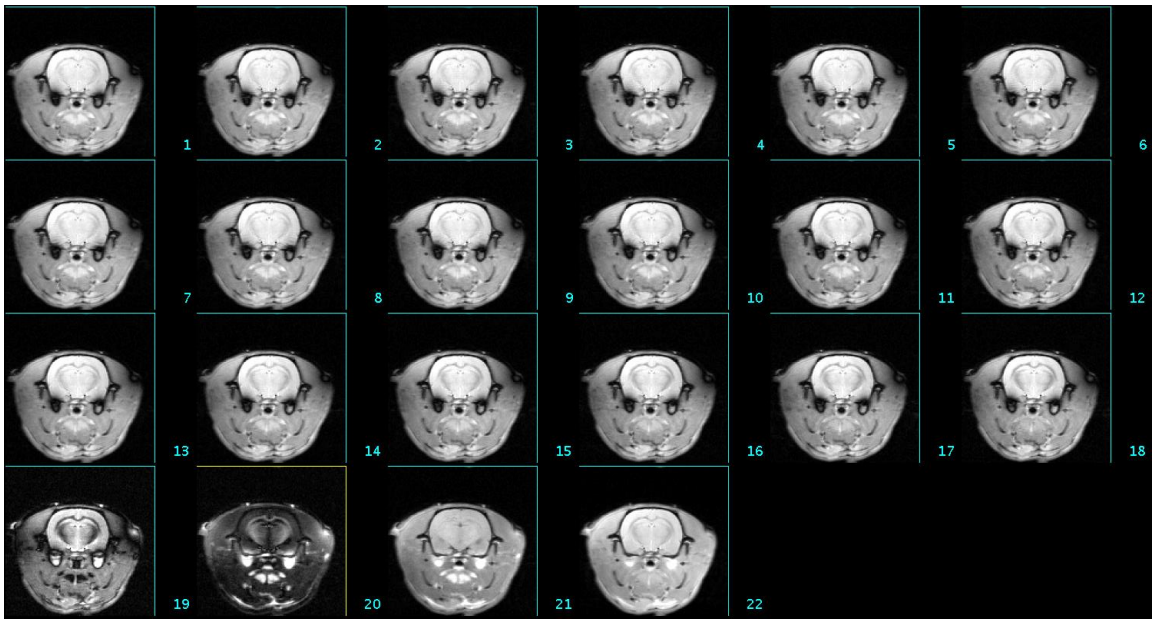

Figure 2-5. Representative qMT dataset consisting of 22 T1 weighted images acquired using SIR-FSE sequence. The contrast was modulated by varying the inversion time (ti) in an exponential manner. The white matter appears dark compared to the grey matter in images 1-18 and 22, while the sharp contrast inversion can be seen in image 19 where the white matter appears bright compared to the grey matter.

For the DTI study, a diffusion weighted spin echo pulse sequence with a 1.2 s repetition time, 2 averages, 29 ms echo time, 15 ms between gradient pulses, 6 ms diffusion gradient duration, b value of 1.3398 ms/μm2, diffusion sensitizing gradients along twelve directions (1,1,0), (-1,-1,0), (0,1,1), (0,-1,-1), (1,0,1), (-1,0,-1), (-1,1,0), (1,-1,0), (0,-1,1), (0,1,-1), (1,0,-1), (-1,0,1) plus a normalizing image with no diffusion gradients, and the same spatial resolution as in the QMT experiments was used to acquire data as shown in Figure 2-6. The scan time was about 50 minutes.

The diffusion tensor (D), calculated by matrix diagonalization from tensor element maps, on a pixel by pixel basis, was used to derive the eigenvalues $\lambda_1, \lambda_2, \lambda_3$ and eigenvectors. DTI parameter maps were calculated from these eigenvalues using custom software written in Matlab, where, RD = $(\lambda_2 + \lambda_3)/2$; AD = λ_1, the largest eigenvalue; Davg = $(\lambda_1 + \lambda_2 + \lambda_3)/3$; and the relative anisotropy (RA) = $\frac{\sqrt{(\lambda_1 - Tr/3)^2 + (\lambda_2 - Tr/3)^2 + (\lambda_3 - Tr/3)^2}}{\frac{Tr}{\sqrt{3}}}$, where Tr(D)= $\lambda_1 + \lambda_2 + \lambda_3$ is the trace.

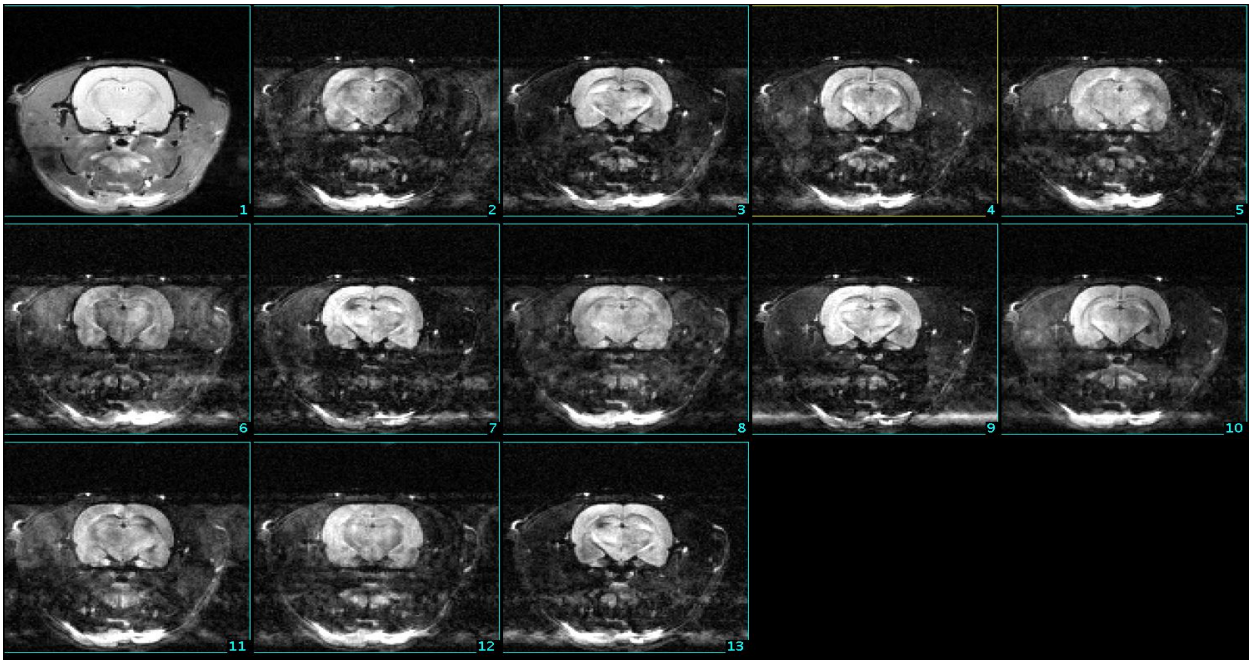

Figure 2-6. Representative DTI dataset consisting of one non-diffusion weighted (B0) image and 12 diffusion weighted images. Each diffusion weighted image is acquired with same b-value but diffusion sensitization in different direction (details in methods section). Notice the blurring in diffusion weighted images due to motion.

A multiple spin echo pulse sequence were used to acquire data for MET2 measurements. The same resolution and imaging slice position was chosen, but the slice thickness was set to 2 mm to increase the SNR. 8 averages, 3 s repetition time, 32 echoes with echo times linearly distributed between 10 ms and 320 ms were used. The total scan time was about 50 minutes. The signal intensity of regions of interest (ROI) in the acquired 32 images were used to fit to a multiple exponential function to determine T2 spectrums.

Histology

The rats were sacrificed within 12 hours after MRI imaging and at 7, 15, and 28 days post injection (no rat was imaged at multiple time points). For immunostaining of paraffin embedded brain tissue, rats were perfused using 4% paraformaldehyde/4% sucrose in PBS. The rat head was decapitated and the brain was removed and postfixed in 10% formaldehyde for 24 h. The injection site was identified by placing the brain in a brain matrix (Plastic one TM) and a 2 mm thickness of brain, which spanned 1 mm anterior and 1 mm posterior to the injection track was cut and embedded in paraffin before sectioning. Two brains were blocked in single paraffin block. The embedding was performed by the Neuropathology Lab of Vanderbilt University. Serial coronal sections (8–10 μm thickness) of the brain were cut and mounted on electroplated glass slides. The slides were then subjected to immune (Myelin basic protein, MBP; microphages, CD68) and histochemical (Luxol-Fast blue—Periodic-Acid Schiff, LFB-PAS) staining protocols.

Initial set of slides were stained with LFB-PAS dual stain. After careful comparison of anatomical structures in serially sectioned histological slides (unstained and stained) and consecutive

structural MRI slices a new set of histology slides for each rat with close correspondence with qMRI slice were identified (data not shown). LFB-PAS staining provides additional pathological information (myelin and microphages). However, the color contrast interferes with accurate myelin quantification along with additional staining issues such as uniformity of staining and oversaturation leading to marginalized myelin quantification. Thus, the new sets of slides were stained with LFB alone.

Luxol fast blue (LFB) histochemical staining was performed to detect the myelin content in the rat brain, primarily in the corpus callosum. LFB –an alcohol soluble sulphonated copper phthalocyanine type dye– is widely used for staining of myelin/myelinated axons on formalin-fixed, paraffin-embedded and frozen sections of CNS (brain and spinal cord) tissue. The myelin, including phospholipids, is stained blue, and the neurons are stained violet. PAS stain highlights microphages stained in pale pink.

Image and Statistical analysis

LFB stained tissue sections were imaged on an Olympus AX70 microscope with field of view of about two millimeters in diameter at lowest magnification. Hence, due to smaller field of view, about 80 images were needed to cover the whole slide with additional photo stitching and image processing steps. MRI images have ~250 µm /pixel in plane resolution, which dictates the resolution required from histological stained slide images for correlation; and images of histological sections with micron level resolution were not deemed essential. Thus, I built an in-house custom setup using Cannon Rebel XSi camera and 180 mm macro imaging lens, to image the histology sections. This setup was used for imaging stained and unstained histological slides. High quality 24-bit RGB images were acquired of histological LFB stained

slides. The demyelination is seen as a reduction in blueness in LFB stained slides, in the region of LPS injection (Figure 2-8a). The CC of rats injected with phosphate buffer saline (PBS) did not show prominent demyelination (Figure 2-8b).

Various processing methods were explored to find a simple and suitable myelin specific contrast generating method. Four methods were compared. 1) Max – Red-channel, 2) Blue-channel – Red-channel, 3) Blue+Green-channel – Red-channel, 4) Transmitted intensity gray level image (R+G+B). Vector methods for color separations were explored (Macenko et al., 2009) but were not selected on basis of complexity, image quality required and simpler methods stated above performed adequately.

As shown in appendix #, while methods 1, 3, and 4 showed excellent myelin contrast, method 2 (Blue-channel – Red-channel) produced the greatest myelin content tissue contrast. However, method 4 (transmitted gray level, referred as OD transmitted) was used due to its wide use in the literature and ease of comparing our results with literature. To normalize myelin maps for inter-rat staining variations, maximum myelin content pixel in non-demyelinated CC was chosen to calculate the normalization factor. Other approaches using the normalization factor calculated from gray matter ROI, and other white matter structures outside CC were explored. While Normalization using gray matter ROI was explored, white matter based normalization was preferred due to higher normalization factor to noise (within ROI intensity fluctuations across rats) ratio. The normalization factor was calculated using white matter structures outside CC had comparable results.

Co-registraton between MRI and histology is challenging due to the tissue shrinkage, distortions, and tearing that occurs during tissue processing. Tissue shrinkage is minimal during fixation. However, shrinkage, distortions, and tearing occur during paraffin blocking, sectioning, staining, and mounting procedures. We attempted rigid, affine and nonlinear registration approaches to register MRI sections with stained histology sections. However, due to the severe artifacts and structural mismatches, these approaches did not yield satisfactory results to perform pixel-by-pixel correlation. Affine registration lead to best results due to inclusion of rotation, translation, scaling and shearing transforms Correcting for the local distortions using non-linear registration approaches lead to obvious additional unreal deformations in an attempt to match histology. However, even after affine registration, there were clear mistakes on a pixel-to-pixel basis. Hence, after affine registration, an ROI comparison approach was employed. The registration programs used for analysis were part of in-house VUIIS Image Processing package (vuTools) written in MATLAB that uses the Insight Segmentation and Registration toolkit (ITK) programs.

ROI's were selected by segmenting the CC in 1mm sections on each side from the sagittal suture, midline in axial sections. We used five 1 mm ROI's on each side of sagittal suture (midline) within CC for white matter and above CC for gray matter (as illustrated in Figure 2-7) to characterize demyelination. A total of about 10 ROI's were examined for each rat in CC white matter and in gray matter just above the CC. the ROI's were all adjacent each spanning about 1mm in CC.

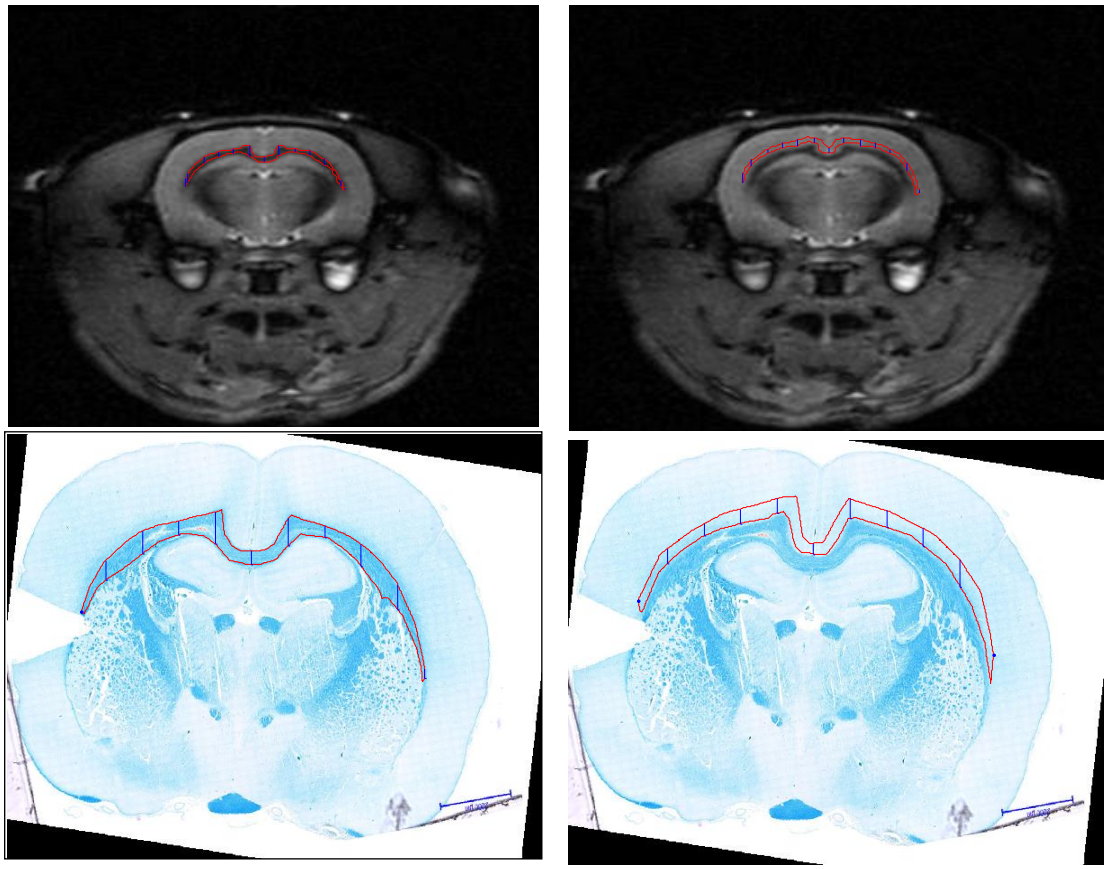

Figure 2-7. Representative T2 weighted axial MR images and corresponding light microscopy. Slices with CC WM and cortical GM ROIs are outlined in red. ROIs and further segmented in 1mm sections, from midline of brain as indicated by blue lines.

The ROIs selected were used to investigate associations between qMRI metrics and myelin histology. To investigate the relationship between these two numeric variables, scatter plots were generated for each rat, where each point correspond to a 1 mm ROI in CC or cortical GM above CC, to compare MRI parameters with histochemical staining measure of myelin count.

The strength of correlations and significance levels observed in scatter plots were quantified by calculating R-squared, Pearson-R correlation coefficient, and corresponding p-values. Pearson's correlation coefficients were calculated using mean ROI values for MR and histological matrices using Matlab. P-values were calculated to determine the statistical significance of correlations and test for the probability of observing the correlations as extreme as seen when in fact the null hypothesis (H_0) is true, and is coincidental.

To investigate the difference in qMRI parameters in WM and cortical GM above CC. mean of all GM and WM ROI's were calculated. Two-sample t-test was performed on the null hypothesis that GM and WM ROIs are independent random samples from normal distributions with equal means and unknown variances against alternative hypothesis that means are not equal, at 5% significance level. Two-sample t-test yielded the p-value and 95% confidence interval on the difference in means. The difference in mean and confidence interval was used to quantify the ability of qMRI parameters to separate white and GM.

Evaluation of correspondence between MRI and histological slice is important for meaningful correlations. Histological sections were selected for myelin staining based on evidence of tissue damage cause by injection needle. Serial axial histological sections and serial structural MRI

images were carefully examined for anatomical feature correspondence. Histological sections with anatomical features corresponding to MRI imaging slice, used for qMRI slice prescription, were selected and stained with LFB myelin stain. Unfortunately, it was found that for the two saline injected rats (Rat 66 and Rat 70) the qMRI slice and histological section did not match. The histological slice with anatomical features corresponding to qMRI slice was not present in the sectioned histological slices from 2mm tissue slab extracted for histology. In the case of Rat 66, day 14 saline injected rat, the dual stained histological section selected during initial staining did not match with the anatomical features. In addition, the dual stained section suffered from non-uniform and over-saturation in staining. Rat 66 was excluded for the fact that the myelin staining was of poor quality and was stained differently from other rats using dual stain Luxol fast blue – periodic acid Schiff (LFB-PAS) that also resulted in normalization methods ineffective. However, for Rat 70 – day 28 saline injected rat – no myelin stained section was available. Thus, these two saline rats were excluded from myelin histology analysis.

Results

Histopathology reveals LPS does induce focal demyelination within the rodent CC

We first sought to validate our rodent model of MS where LPS was used to induce focal demyelination within the CC. To validate this, we used histopathological examination, which is the gold standard for detecting demyelination. LPS administration in the CC of the left hemisphere led to focal demyelination at the injection site (as described in method section) as indicated by histochemical LFB staining and immunohistological MBP staining. The demyelination was indicated by the reduction of LFB intensity at the site of LPS injection (indicated by red arrows in Figure 2-8) as determined by light microscopy. Figure 2-8 shows representative LFB stained axial sections for LPS- and saline-injected rats 7 days post-injection,

respectively. The histopathology of saline-injected rat CC did not show local demyelination at the injection site as myelin content was similar to the contralateral non-injected hemisphere (Figure 2-8b).

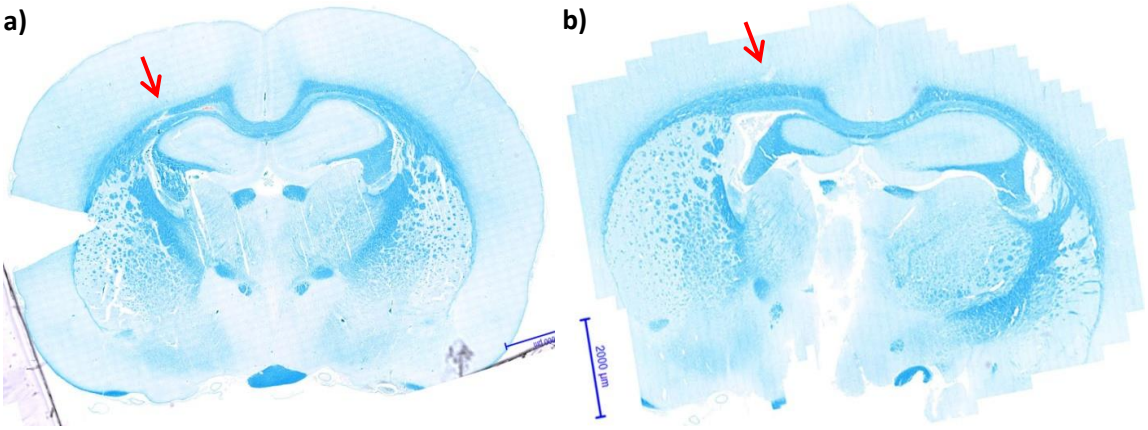

Figure 2-8. Focal demyelination is seen on myelin histology in LPS injected rats. Figure shows representative LFB stained axial histological sections at injection site in a) LPS and b) saline injected animals. The blue color intensity is indicative of myelin content. Notice the degree of demyelination observed in LPS injected rat (left) in comparison to saline rat (right). Red arrows indicate the injection site.

Immunohistological MBP and histochemical LFB myelin stains reveal similar demyelination patterns in LPS-induced lesions.

Visual examinations of MBP and LFB-PAS stained serial sections showed similar patterns of demyelination at the LPS injection site within the CC (ROIs were chosen following visual inspection and are outlined in Figure 2-9c-d) as compared to the non-injected contralateral CC (Figure 2-9a-b). These results indicate that both MBP (an immunohistological stain) and LFB (a histochemical stain) reveal similar extent of demyelination. Although MBP staining is more specific to myelin, MBP staining is more complex, time, and labor intensive (in addition to being costly). Comparatively, LFB staining provided superior contrast between demyelinated and non-demyelinated regions and was easier to quantify due to Red-Green-Blue (RGB) channel digitization in images. Given these advantages of LFB staining, we decided to use LFB staining for our subsequent experiments.

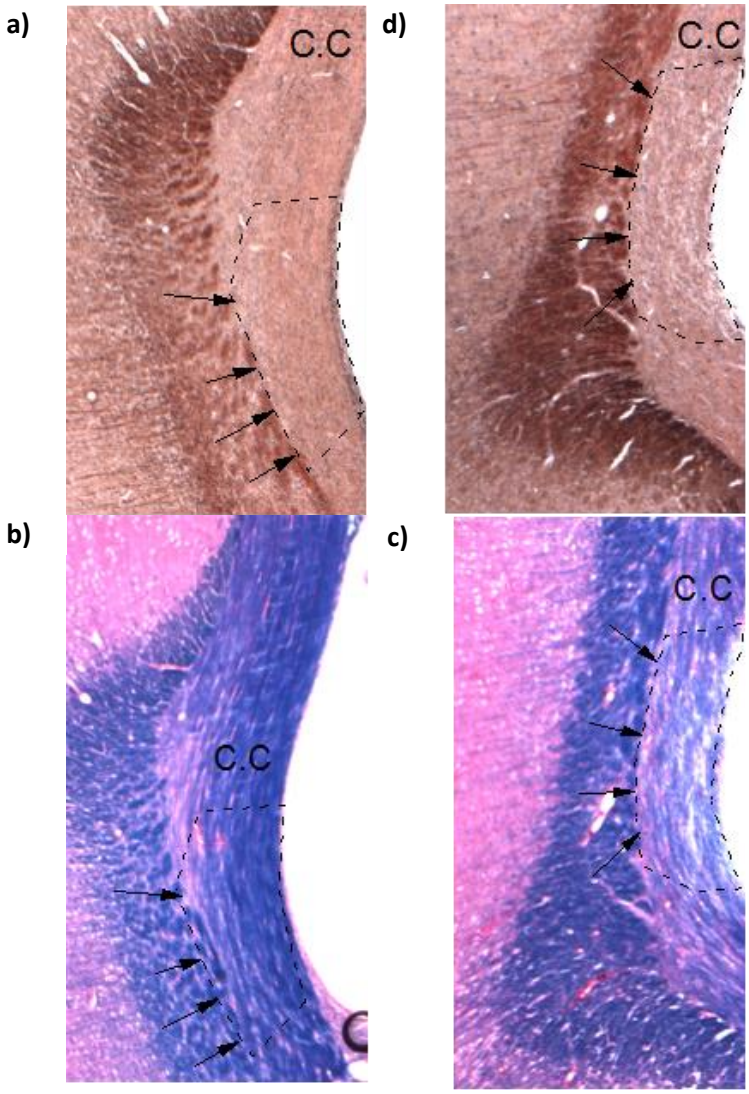

Figure 2-9. Comparison of MBP and LFB myelin stains. Side-by-side comparison of MBP (top panel) and LFB-PAS (bottom panel) myelin stains in the CC in the non-injected left (a-b) and LPS-injected right hemisphere (c-d) 28 day post-injection: The injection site is indicated by black arrows and ROIs are outlined by the dashed lines.

Histological examinations reveal small and thin demyelinated lesions.

Moving from left to right, along the CC, the extent demyelination ranged from no demyelination to near complete demyelination. More specifically, the demyelination along the length of the CC ranged from 1-2 mm at the site of LPS injection (Figure 2-8a) and, in some test cases, extended to the right hemisphere of the brain along CC fibers in the trunk region (data not shown). Furthermore, the thickness of demyelination ranged from 1/2 to less than 1/3 of CC.

Two of six LPS injected rats developed extended demyelination along the CC as indicated by light microscopy images of LFB-stained histological sections. Four of six LPS-injected rats showed no prominent demyelination at the injection site following visual inspection of LFB-stained sections (Figure 2-10). These observations indicated animal response variability, following LPS injection, which include the spatial expanse and degree of CC demyelination.

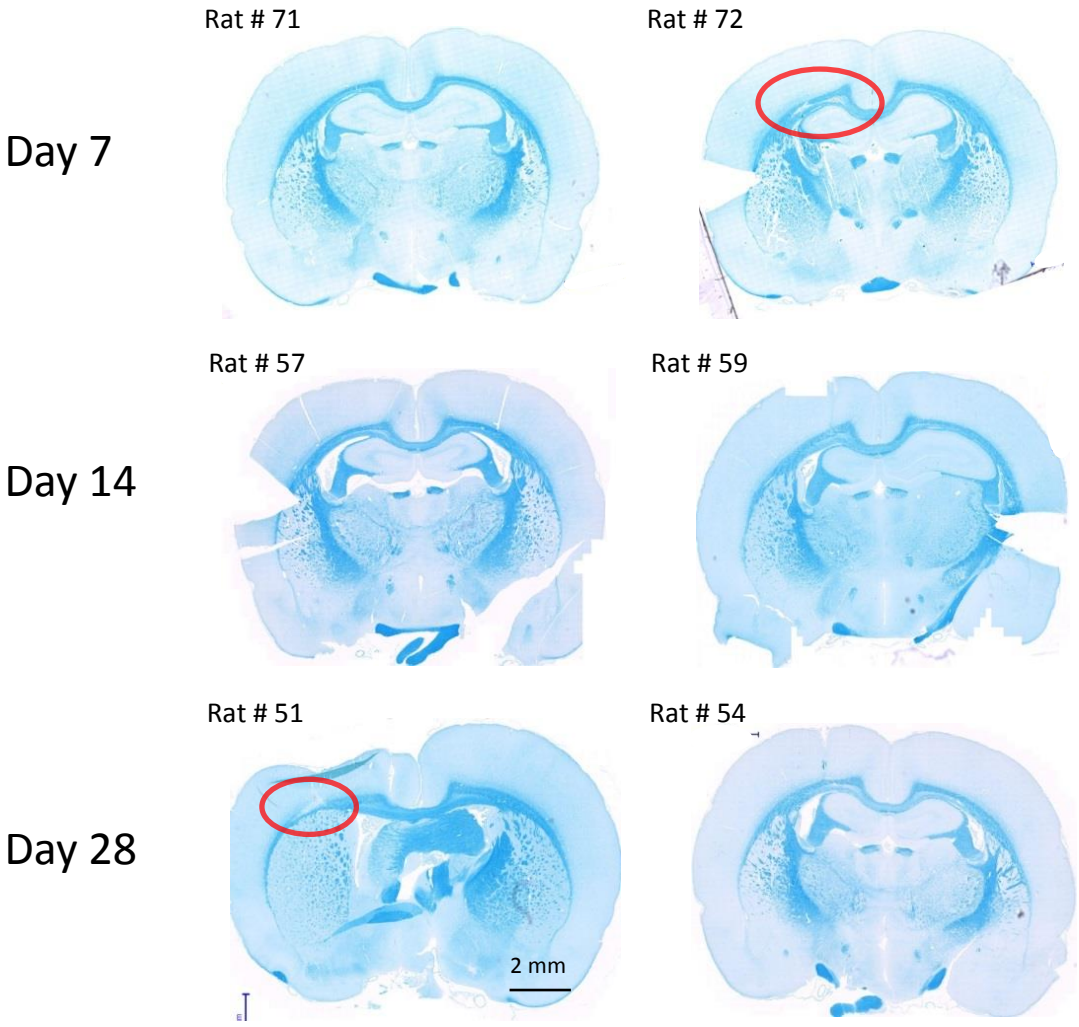

Figure 2-10. LFB stained axial sections of LPS injected rats. Selected LFB stained axial sections from the injection site for six LPS-injected (left hemisphere) rats after three time points post-injection: Day 7, Day 14, and Day 28. Demyelination in Rat 51 (Day 7) and Rat 72 (Day 28), is highlighted with red oval ROIs.

Anatomical feature discrepancy observed between MR and histology images.

Along with inter-rat variability in response to LPS injection, visual inspection revealed anatomical discrepancies between MR and stained/unstained histological images. These latter discrepancies arose from a major limitation of comparative analyses of MRI and histological methodologies. More specifically, the precise determination of qMT and DTI parameters requires a slice thickness of 1 mm due to the demands on SNR and image resolution. However, our histological sectioning was performed at 8-10 µm slice thickness. As a result, we were comparing MR images of 1 mm slice to 8-10 µm thick histological sections. Given that we were comparing MR images from 1 mm thick brain slices, our MR images had contributions from anatomical features within our selected within 1 mm range. Conversely, the histological sections sampled a fraction of the 1 mm MR thickness. Thus, a certain degree of discrepancy is expected between observed anatomical features in MR and histology images. Though these discrepancies may increase experimental variability, we do not expect the anatomical features observed on histological sections to be different from the averaged MRI features. For our experimental studies, we were able to map the averaged MRI anatomical features to our histological sections characterized by a specific Bregma co-ordinate (Paxinos Rat Brain Atlas). When we were not able to map our MRI images to the Bregma co-ordinate of our histological sections, the rats were excluded from further analyses.

Alternatively, the discrepancy between MR and histological images may have arisen from technical errors in histological analyses such as the differences in the plane of serial slicing (e.g. oblique sectioning resulting in left and right asymmetry, see Figure 2-10), mounting of brain tissue, section alignment, and non-linear distortions of histological sections (Simmons and Swanson, 2009).

These discrepancies may explain the misregistration between MRI and histological images observed in our experimental group. In four of the six experimental rats, anatomical features, such as ventricle size and shape, were consistent in both MR and histological images as determined by the Paxinos Rat Brain Atlas (Figure 2-11). Conversely, the remaining two LPS-injected rats, rat 66 and rat 70, were excluded from myelin histological analysis due to clear anatomical differences in MR and histological images, such as the anatomical features of the ventricles and internal capsule, indicating that the histological section did not correspond with the location covered for qMRI analysis in CC (Figure 2-11). As such, these animals were excluded from the rest of the study.

T2w FSE imaging is ineffective in identifying LPS-induced focal demyelination within the CC.

T2w FSE images are routinely used clinically to assist in accurate MS diagnosis via *in vivo* detection of WM lesions. Given the heavy use of T2w FSE images in the identification of MS-related lesions, we first used T2w FSE images to locate the injection site as well as to identify the spatial extent of the LPS-induced lesions. To do so, we used T2w FSE images to determine brain geometry and to select an axial image slice perpendicular to the CC. This approach allowed us to plan the prescription of the qMRI slice. These experimental results showed that T2w FSE images were effective in identifying the injection-induced tissue damage just below the skull (red arrow; Figure 2-2). Although T2w FSE images were effective in identifying injection sites just below the skull, however, this approach was less effective in accurately localizing both the CC injection site and LPS injection-induced focal demyelination (Figure 2-2). Overall, these

experimental results indicate the T2w FSE images were not an effective tool to locate LPS-induced lesions *in vivo*.

Excellent gray-white matter contrast is observed in qMRI parameters.

Figure 2-12 shows representative *in vivo* qMT and DTI parameter maps from a qMRI slice that contains the injection site. High contrast between gray and white matter structures was observed in the qMRI parameter maps, most notably in the PSR (qMT) map. Furthermore, the white matter appears brighter in the PSR map and darker in RD (DTI) parameter map.

GM and WM differences were significant for all qMRI parameters with PSR showing the greatest GM and WM separation.

GM and WM contrast in MRI is critical to accurately distinguish and segment anatomical regions, as well as increase the sensitivity towards primary demyelinating lesions (e.g. Type III MS lesions) (Lucchinetti et al., 2000) that are otherwise difficult to detect with conventional MRI sequences. Thus, we next investigated the comparative power of qMRI parameters to separate GM and WM. Table 2.3 summarizes the mean values in WM and GM ROIs for each rat along with the variation (standard deviation) in WM and GM, respectively, of each rat. Std (rats) column denotes standard deviation in WM and GM and indicates the inter-rat variation in parameter for comparison with intra-rat variations as shown in sub tables stdWM and stdGM, respectively.

Given that we have examined the intra- and inter-rat variations in WM and GM, we next sought to examine the pooled the WM and GM within experimental groups to further examine the WM

and GM differences with greater statistical power. A two sample t-test analysis can evaluate the difference between two groups. To quantify the ability of qMRI parameters to separate WM and GM, a two sample t-test was performed. The null hypothesis being that the WM and GM ROIs have the same mean with all rats (grouped together) n=8 and 10 ROIs for each rat in GM and WM, respectively. All qMRI parameters rejected null hypothesis (indicated by h=1 in Table 2.4). PSR has the smallest p-value among qMRI parameters (i.e. best ability to separate WM from GM). The columns in Table 2.4 'Δ-Parameter' shows the difference between GM and WM while 'ci' shows the 95% confidence intervals on this difference. Figure 2-20 and Figure 2-21 represent the same information as displayed in table 2.4. In Figure 2-20, the mean values for qMRI parameters in WM and GM are plotted along with their standard deviations (error bars) normalized to the mean GM value for respective qMRI parameters. This allowed for direct comparison of the relative difference between GM and WM values. Notably, the PSR shows the best separation of gray and white matter second to myelin histology, as is also seen in the data point groups of GM and WM on the qMRI axis (y-axis) of the scatter plots. There was no normalization performed in Figure 2-21. These figures also include data from Rodney and colleagues (1980) (Gore et al., 1981; Rodney et al., 1980) on protein and lipid composition of gray and white matter of the brain. A striking similarity is observed in WM values relative to GM between PSR and total protein + lipid content, and also between LFB measured myelin content and lipid content.

Though PSR shows the strongest correlation (and tightest confidence interval) with quantitative myelin histology in combined WM and GM analyses, no strong correlations were observed within WM or GM with myelin content.

Figures 2-13 to 2-18) show the scatter plots of qMRI parameters vs. histological myelin content in ROI's selected in gray and white matter regions (as is shown in Figure 2-7) with linear regression analyses performed for each sample. Each data point in the scatter plot corresponds to a 1mm ROI in both white matter of CC or the gray matter above the CC. Clear separation between the gray and white matter data groups was observed on myelin histology axis (x-axis) due to lower myelin content in gray matter compared to CC white matter. Notably, there was a lack of clear correlations within the WM and GM data points with myelin content, which was further investigated by grouping the data into three sets of combined GM and WM, WM, and GM groups.

Table 2.1 gives the Pearson correlation coefficient (R), the coefficient of determination (R2), and the p-value for the correlations in the following experimental groups: 1) WM ROIs, 2) GM ROIs, and 3) WM+GM ROIs. For direct comparison, Figure 2-19 represents these correlations graphically, with the error bars denoting 95% confidence interval for these correlations. No significant correlations ($p>0.05$) were seen in the separate GM and WM analyses, except RD in GM which demonstrated a weak Pearson R of 0.27 at 95% confidence. Upon plotting the myelin histology content (x-axis) of GM and WM, both GM and WM fell into two discrete groups (see Figures 2-13 to 2-18) and increased the dynamic range of myelin content variation. In the combined WM and GM analyses, all the correlations between qMRI (qMT and DTI) parameters vs. histological myelin content were found to be significant (at 95% confidence level, see Table 2.2). qMT parameters correlated strongly with myelin content. More specifically, PSR and SR showed the strongest positive correlations (Pearson-R: 0.93 and 0.85, respectively) while FR correlated negatively with a correlation coefficient of -0.74 (Pearson-R). The correlations for the

DTI parameters were comparatively weak with RA and AD correlating positively with R= 0.57 and 0.46 (Pearson-R), respectively, while RD correlated negatively with a Pearson-R of -0.36.

The coefficient of determination (R2) is a measure of goodness of fit for a linear model and can be interpreted as the fraction of variability in the dependent variable explained by the independent variable. The trend of correlations in qMT parameters with myelin histology, discussed above, persisted for the WM+GM analyses of individual rats (Table 2.2). The R2 of the qMRI parameters and myelin (LFB) content, for each individual rat, with combined WM and GM ROIs demonstrated stronger R2 values for PSR and SR (Table 2.1a corresponding; p-values are given in Table 2.2b).

In summary, DTI parameters including RD has much weaker association with histological myelin content while qMT parameters, specifically PSR, associated strongly with myelin content. Overall, these data lend support to the hypothesis that, in comparison to RD, PSR demonstrates greater sensitivity to myelin in type III model of MS lesions.

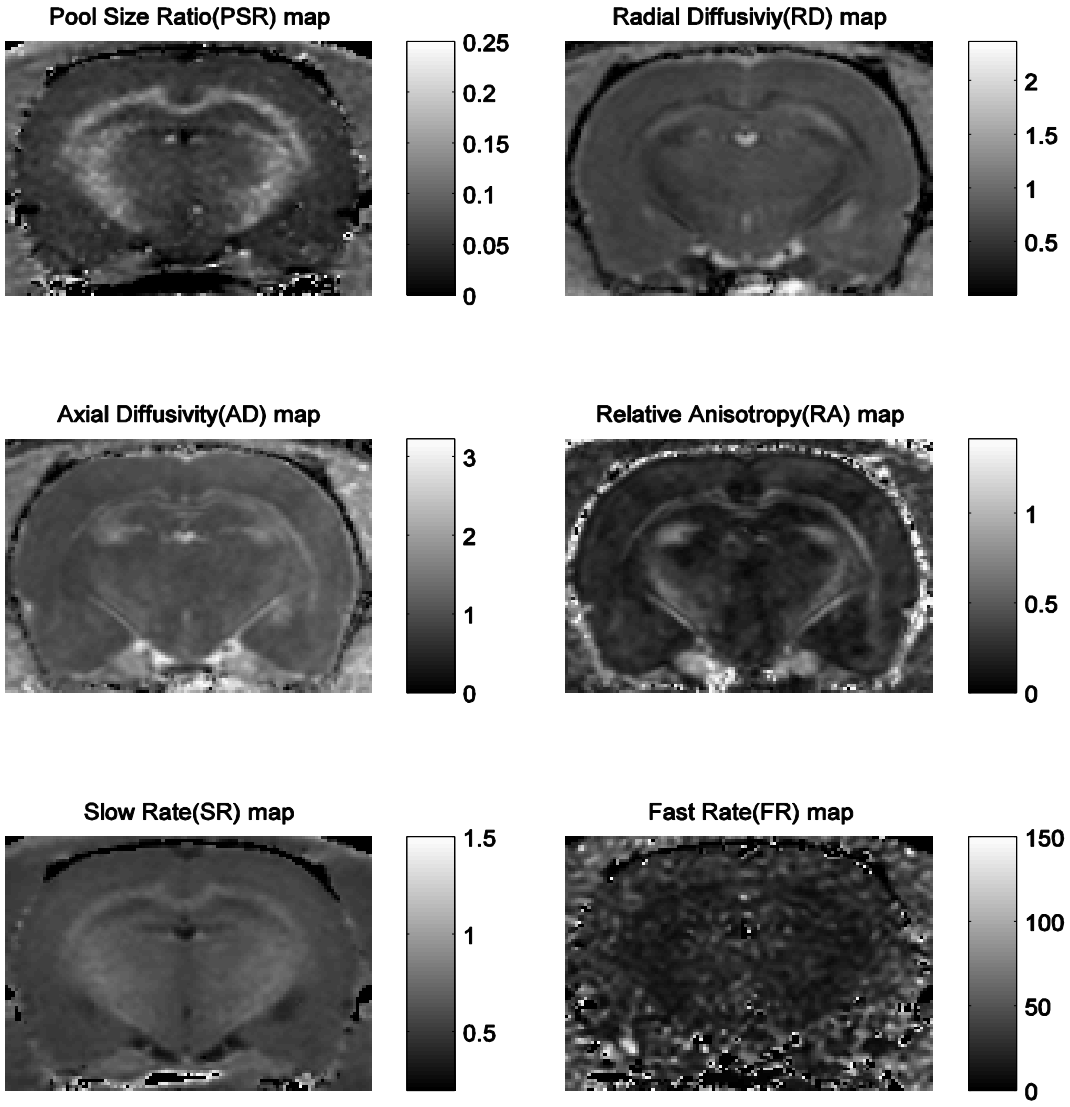

Figure 2-11. qMRI Parameter maps. Representative qMT (PSR, Slow rate, Fast rate) and DTI (Radial diffusivity, axial diffusivity, Relative anisotropy) parameter maps of selected 1mm thick axial slice for a LPS injected rat.

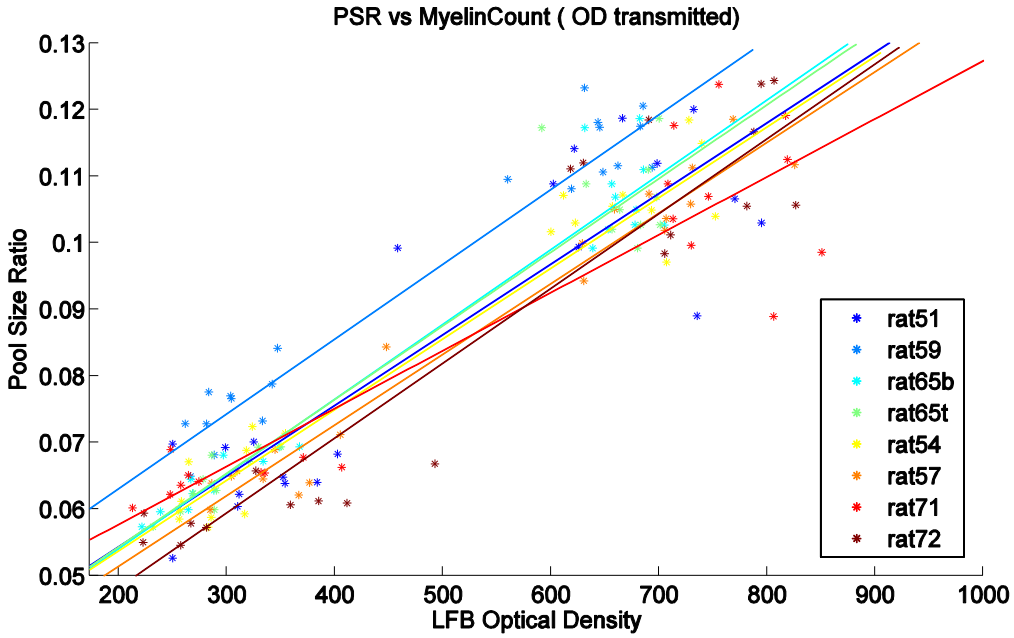

Figure 2-12. Correlation of PSR to LFB. Scatter plot of qMT measured pool size ratio and myelin count quantified by LFB stained histological transmitted optical density in gray matter (above corpus callosum) and white matter (corpus callosum) regions. Colored lines are best linear fits for each individual rat.

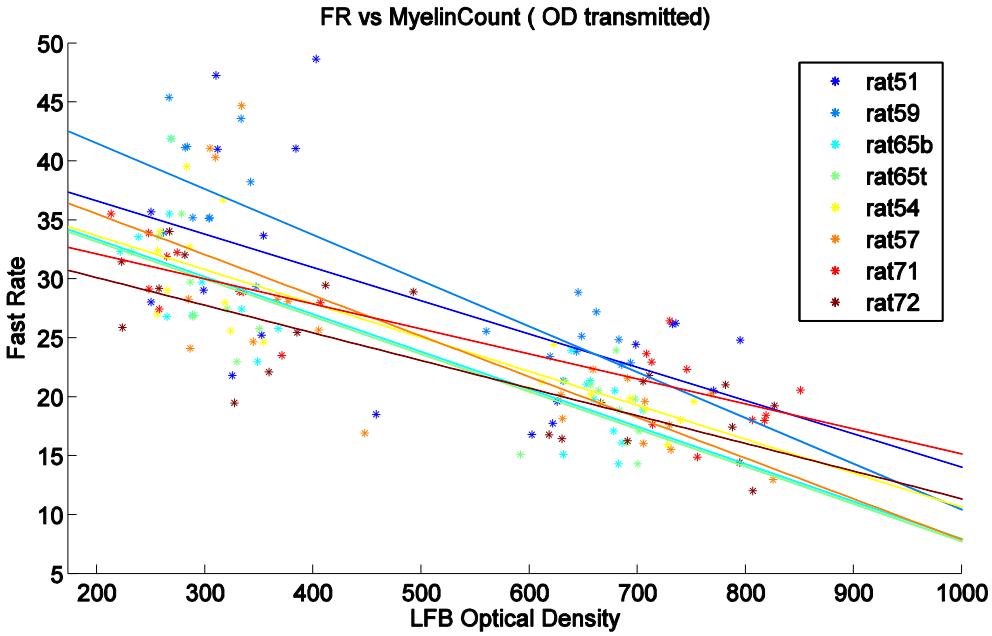

Figure 2-13. Correlation of Fast Rate to LFB. Scatter plot of qMT measured fast recovery rate and myelin count quantified by LFB stained histological transmitted optical density in gray matter (above corpus callosum) and white matter (corpus callosum) regions. Colored lines are best linear fits for each individual rat.

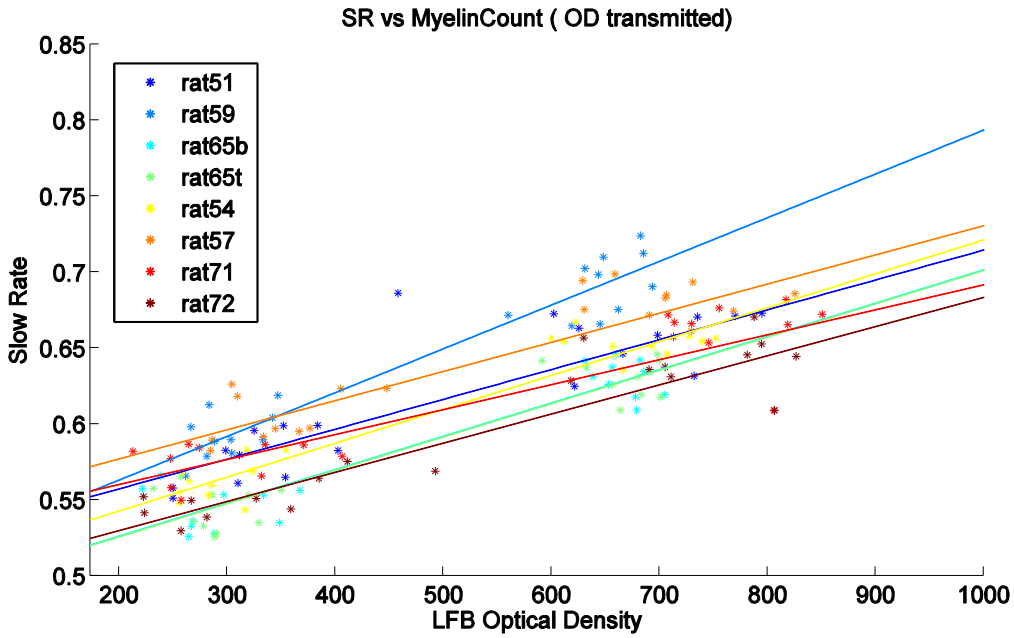

Figure 2-14. Correlation of Slow Rate to LFB. Scatter plots of qMT measured slow recovery rate and myelin count quantified by LFB stained histological transmitted optical density in gray matter (above corpus callosum) and white matter (corpus callosum) regions. Colored lines are best linear fits for each individual rat.

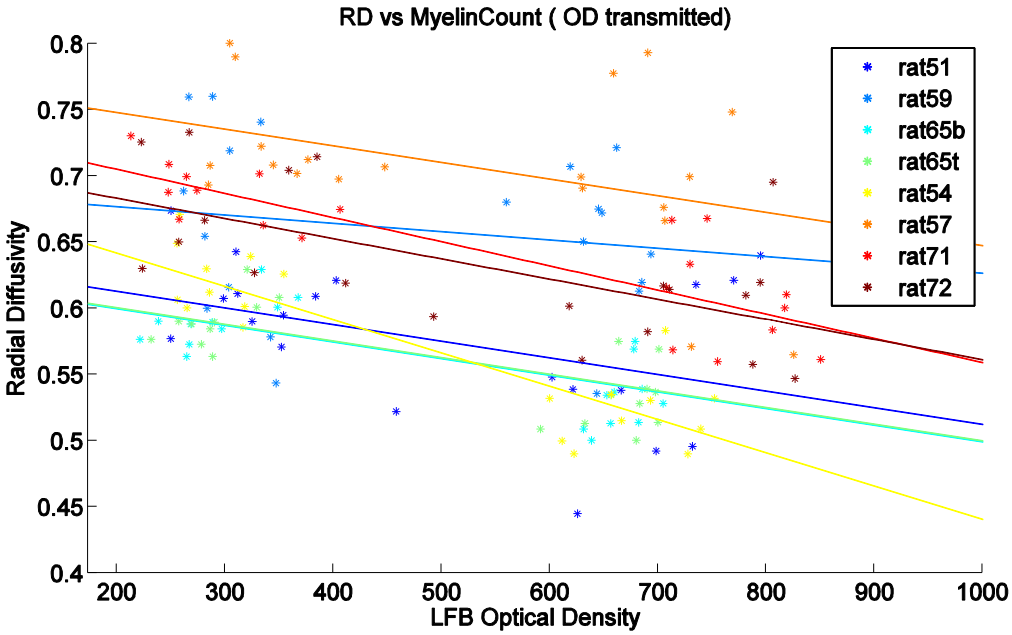

Figure 2-15. Correlation of Radial Diffusivity to LFB. Scatter plots: Scatter plot of DTI measured radial diffusivity and myelin count quantified by LFB stained histological transmitted optical density in gray matter (above corpus callosum) and white matter (corpus callosum) regions. Colored lines are best linear fits for each individual rat.

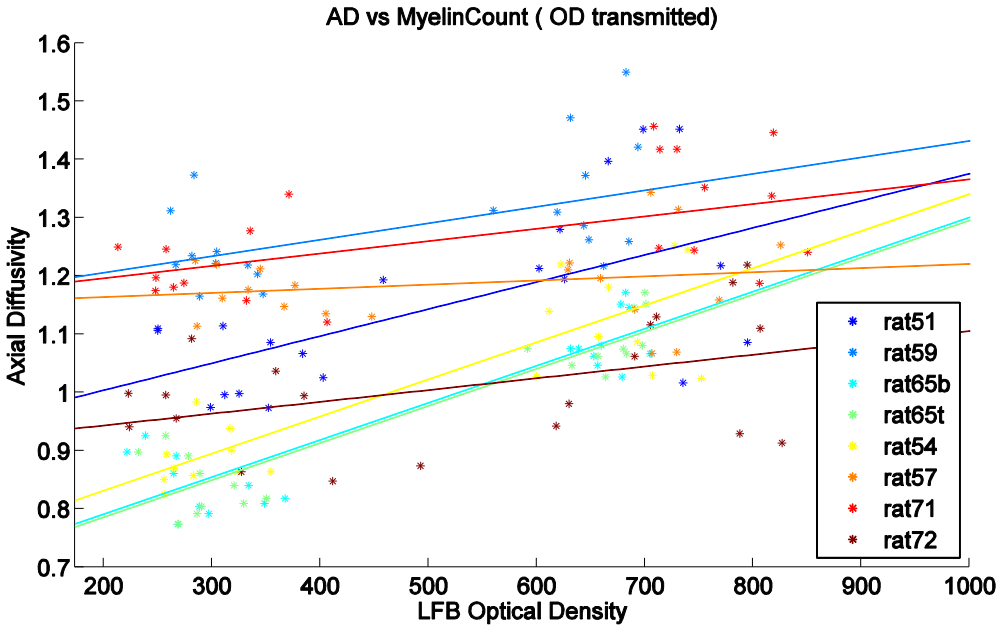

Figure 2-16. Correlation of Axial Diffusivity to LFB. Scatter plots: scatter plot of DTI measured axial diffusivity and myelin count quantified by LFB stained histological transmitted optical density in gray matter (above corpus callosum) and white matter (corpus callosum) regions. Colored lines are best linear fits for each individual rat.

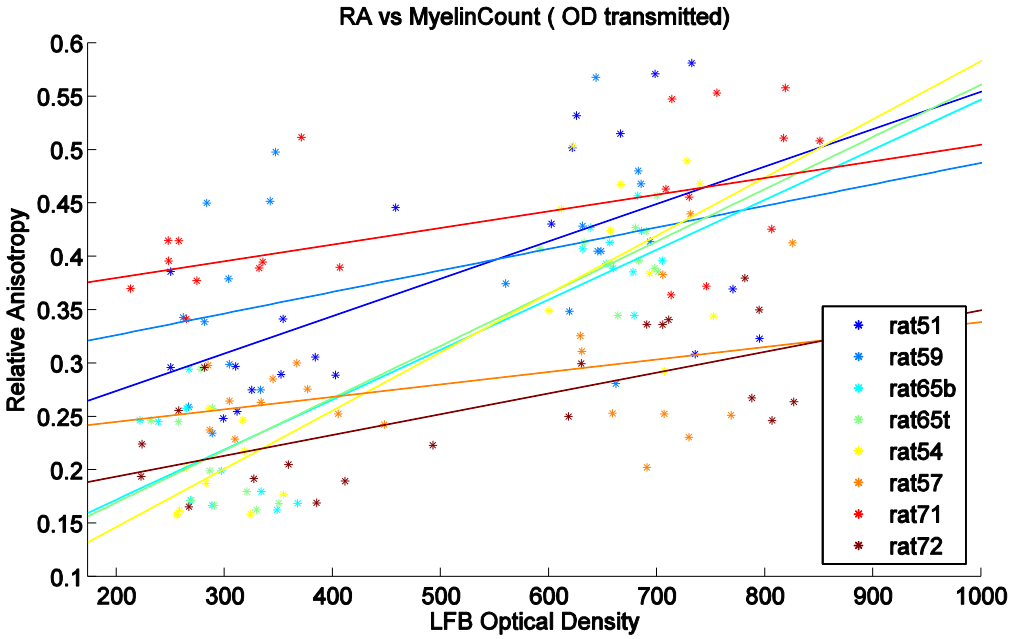

Figure 2-17 Correlation of Relative Anisotropy to LFB. Scatter plot of DTI measured relative Anisotropy and myelin count quantified by LFB stained histological transmitted optical density in gray matter (above corpus callosum) and white matter (corpus callosum) regions. Colored lines are best linear fits for each individual rat.

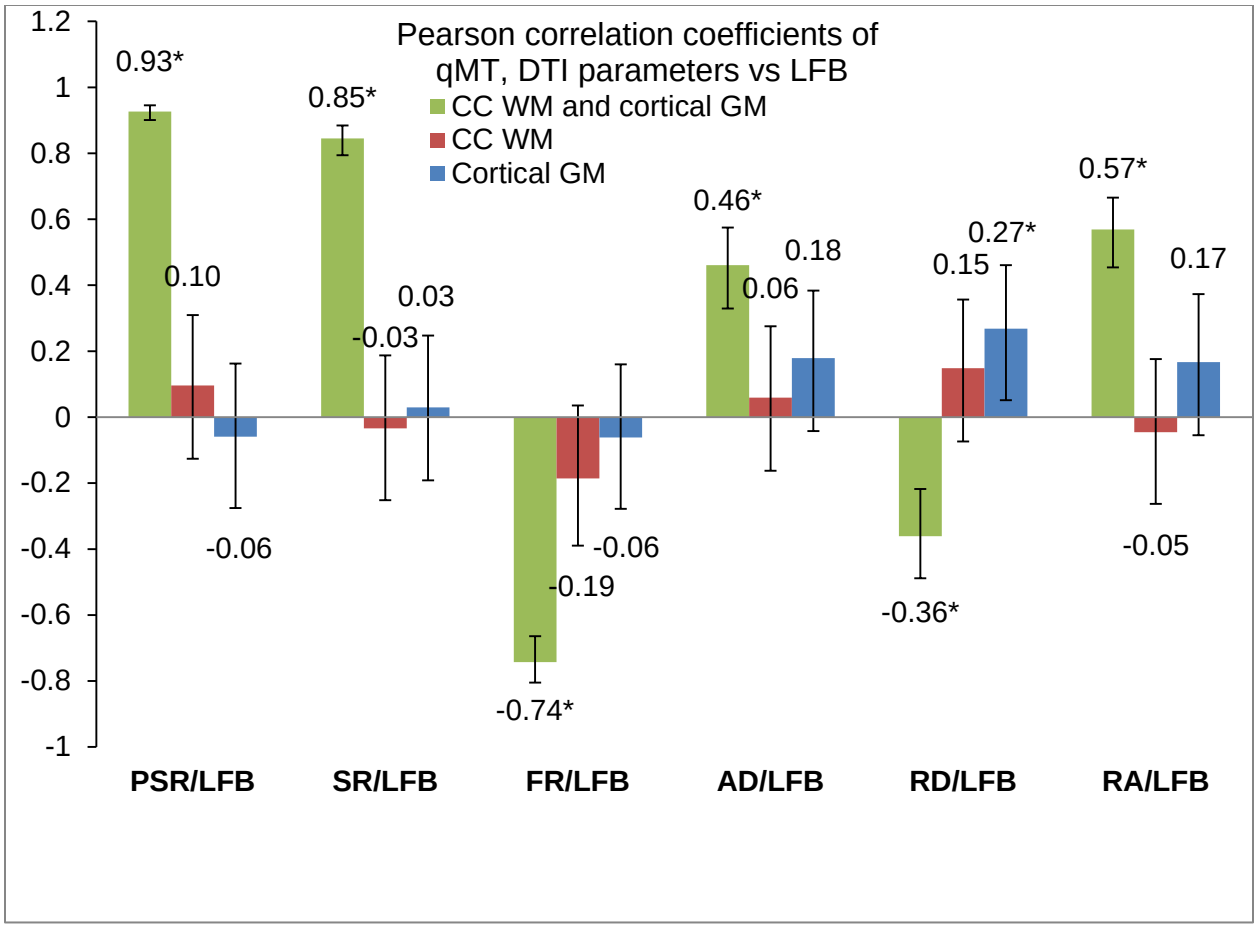

Figure 2-18. Pearson correlations of DTI (RD, AD, and RA) and qMT (PSR, SR, and FR) parameters vs LFB histology. The error bars denote the 95% confidence intervals for correlation coefficients. p-values for the correlations are given in Table 2.2. Correlations with * are significant at α=0.05 significance level.

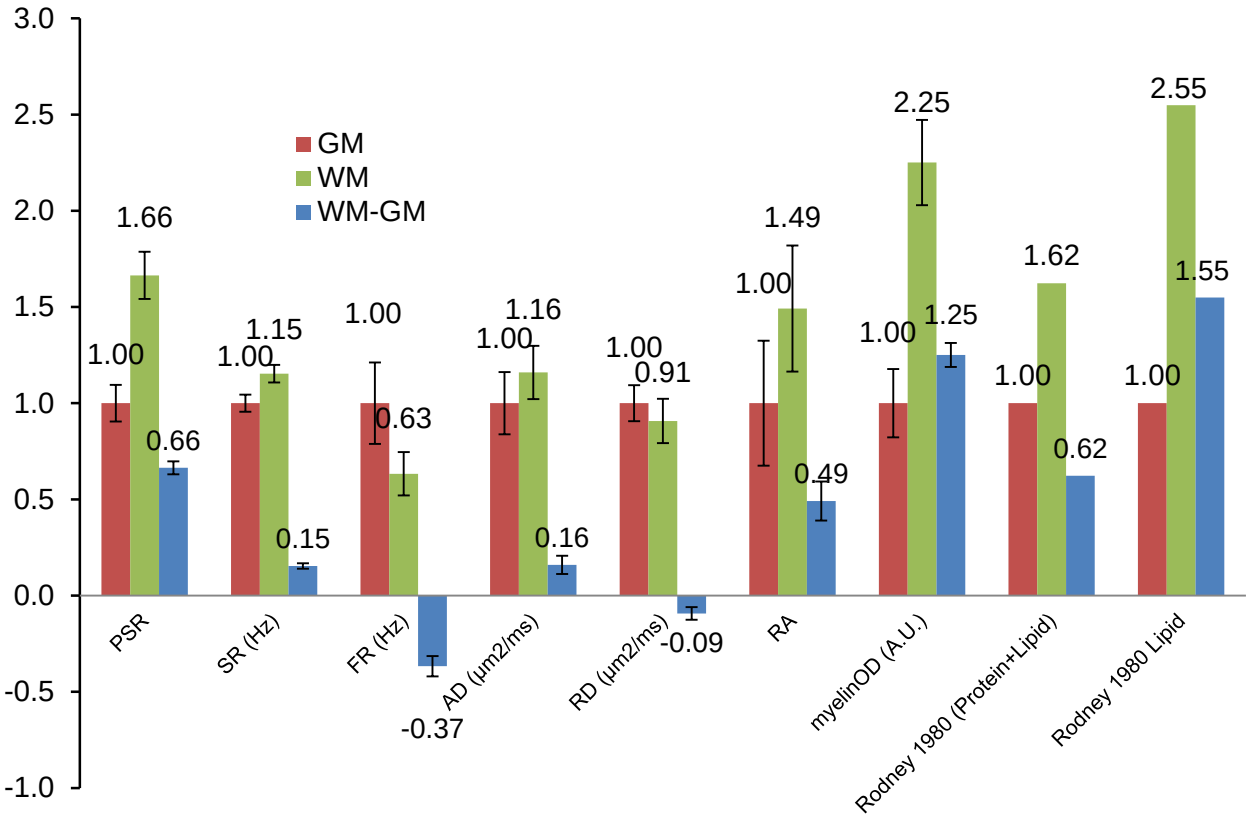

Figure 2-19. qMT parameter PSR best differentiates gray matter (GM) and white matter (WM). Mean and std of qMT (PSR, SR, and FR), and DTI (RD, AD, and RA) parameters across all ROIs in CC WM (red) and cortical above-CC GM (green), normalized to the GM value. The error bars denote the normalized standard deviation. WM-GM column (blue) represents difference and error bars denote 95% confidence interval.

Table 2-1. Statistical analysis of qMRI parameters with myelin histology. R2, Pearson-R and corresponding p-value for correlations of qMRI metrics with myelin histology in combined CC-WM and cortical above-CC GM, CC-WM and, cortical GM. Data from all rats are grouped together.

WM+GM	PSR/LFB	SR/LFB	FR/LFB	AD/LFB	RD/LFB	RA/LFB
R^2	0.8582	0.7144	0.5515	0.2125	0.1302	0.324
Pearson R	0.9264	0.8452	-0.7426	0.4609	-0.3608	0.5692
p-value	6.75E-69	7.54E-45	2.63E-29	8.58E-10	2.78E-06	4.05E-15
WM						
R^2	0.00924	0.001146	0.03444	0.00352	0.02203	0.002077
Pearson R	0.09612	-0.03385	-0.1856	0.05933	0.1484	-0.04557
p-value	0.3963	0.7656	0.09931	0.6011	0.1889	0.6881
GM						
R^2	0.003528	0.000862	0.003821	0.03202	0.07189	0.02791
Pearson R	-0.05939	0.02936	-0.06181	0.179	0.2681	0.1671
p-value	0.6007	0.796	0.586	0.1122	0.01619	0.1386

Table 2-2a. R-squared value for individual rats. The R-squared values for WM+GM calculated for seven rats from the scatter plots for the relevant qMT and DTI parameters.

qMRI \Rat #	rat51	rat59	rat65b	rat65t	rat54	rat57	rat71	rat72
PSR	0.7808	0.95	0.9488	0.9281	0.94	0.961	0.8469	0.8827
SR	0.7336	0.9179	0.8754	0.881	0.9202	0.8452	0.8401	0.8709
FR	0.3099	0.7729	0.7194	0.6911	0.7532	0.5692	0.7682	0.6274
AD	0.3753	0.2931	0.8117	0.8503	0.7484	0.0268	0.3133	0.1756
RD	0.1564	0.0333	0.5467	0.568	0.7538	0.1626	0.7054	0.3718
RA	0.3725	0.1837	0.7744	0.8086	0.7667	0.1409	0.3699	0.4655

Table 2-2b: *t*-test analysis for individual rat correlations. The p-values values calculated for seven rats from the scatter plots for the relevant qMT and DTI parameters. p-values < 0.05 for the null hypothesis indicate statistically significant correlations.

qMRI \Rat #	rat51	rat59	rat65b	rat65t	rat54	rat57	rat71	rat72
PSR	2.4E-07	3.7E-13	4.6E-13	9.9E-12	1.9E-12	3.9E-14	9.2E-09	8.2E-10
SR	1.4E-06	3.3E-11	1.4E-09	9.4E-10	2.5E-11	1.0E-08	1.4E-08	2.0E-09
FR	1.1E-02	3.3E-07	2.3E-06	5.6E-06	7.1E-07	1.2E-04	4.0E-07	3.2E-05
AD	4.1E-03	1.4E-02	6.1E-08	7.5E-09	8.5E-07	4.9E-01	1.0E-02	6.6E-02
RD	8.4E-02	4.4E-01	2.0E-04	1.2E-04	7.0E-07	7.8E-02	3.6E-06	4.3E-03
RA	4.3E-03	5.9E-02	3.1E-07	7.0E-08	4.3E-07	1.0E-01	4.4E-03	9.2E-04

Table 2-3a. The mean and standard deviations for WM of each rat. The mean and standard deviations of ROI averaged relevant qMT and DTI parameters in CC WM and cortical GM above CC for each individual rat.

Mean WM	rat51	rat59	rat65b	rat65t	rat54	rat57	rat71	rat72
PSR	1.1E-01	1.1E-01	1.1E-01	1.1E-01	1.1E-01	1.1E-01	1.1E-01	1.1E-01
SR	6.6E-01	6.9E-01	6.3E-01	6.3E-01	6.5E-01	6.8E-01	6.6E-01	6.4E-01
FR	2.1E+01	2.5E+01	1.9E+01	1.9E+01	2.0E+01	1.8E+01	2.0E+01	1.8E+01
AD	1.2E+00	1.3E+00	1.1E+00	1.1E+00	1.1E+00	1.2E+00	1.3E+00	1.1E+00
RD	5.5E-01	6.5E-01	5.3E-01	5.3E-01	5.2E-01	6.9E-01	6.1E-01	6.0E-01
RA	4.6E-01	4.2E-01	4.0E-01	4.0E-01	4.2E-01	3.1E-01	4.8E-01	3.1E-01
myelinOD	6.7E+02	6.5E+02	6.7E+02	6.7E+02	6.8E+02	7.1E+02	7.7E+02	7.4E+02

Mean WM	PSR	SR	FR	AD	RD	RA	myelinOD
Std(rats)	3.01E-03	1.99E-02	2.15E+00	1.06E-01	5.84E-02	6.22E-02	3.92E+01

Std WM	rat51	rat59	rat65b	rat65t	rat54	rat57	rat71	rat72
PSR	0.01	0.01	0.01	0.01	0.01	0.01	0.01	0.01
SR	0.02	0.02	0.01	0.01	0.01	0.01	0.02	0.02
FR	3.61	2.24	3.09	3.09	2.20	2.94	3.50	3.18
AD	0.15	0.11	0.05	0.05	0.09	0.09	0.10	0.11
RD	0.06	0.05	0.02	0.02	0.03	0.08	0.04	0.04
RA	0.10	0.08	0.03	0.03	0.07	0.08	0.07	0.05
myelinOD	99.09	39.08	22.90	35.11	54.80	60.92	52.61	74.64

Table 2-3b. The mean and standard deviations for GM of each rat.The mean and standard deviations of ROI averaged relevant qMT and DTI parameters in CC WM and cortical GM above CC for each individual rat.

Mean GM	rat51	rat59	rat65b	rat65t	rat54	rat57	rat71	rat72	Std(rats)
PSR	0.06	0.07	0.06	0.06	0.06	0.07	0.06	0.06	0.00
SR	0.58	0.59	0.54	0.54	0.56	0.60	0.58	0.55	0.02
FR	35.12	37.81	30.27	30.27	30.94	30.18	29.92	27.78	3.22
AD	1.04	1.24	0.84	0.84	0.88	1.17	1.21	0.96	0.15
RD	0.61	0.67	0.59	0.59	0.62	0.72	0.69	0.67	0.04
RA	0.30	0.35	0.21	0.21	0.19	0.26	0.40	0.21	0.07
myelinOD	324.21	301.59	289.91	290.52	292.04	346.32	295.36	323.10	19.65

Std GM	rat51	rat59	rat65b	rat65t	rat54	rat57	rat71	rat72
PSR	0.0054	0.0055	0.0043	0.0043	0.0058	0.0069	0.0026	0.0041
SR	0.0177	0.0161	0.0143	0.0143	0.0134	0.0165	0.0132	0.0143
FR	9.2191	4.9635	5.6013	5.6013	4.9218	8.8637	3.4988	4.5564
AD	0.0577	0.0633	0.0507	0.0507	0.0467	0.0397	0.0648	0.0796
RD	0.0308	0.0791	0.0189	0.0189	0.026	0.0384	0.0236	0.0498
RA	0.0404	0.0901	0.0475	0.0475	0.0374	0.0249	0.0447	0.0402
myelinOD	51.0013	30.6192	47.6095	35.188	34.6301	53.5068	62.4339	88.7918

Table 2-4. GM and WM contrast and *t*-test analyses for qMRI parameters. The mean and standard deviations of qMT and DTI parameters in CC WM and cortical GM above CC averaged over all rats. Following table summarizes the hypothesis test comparison of means for GM and WM.

	PSR	SR	FR	AD	RD	RA	myelinOD
Mean WM	0.1085	0.656	19.963	1.1865	0.5844	0.3983	692.9675
std	0.008	0.0261	3.5497	0.1416	0.0742	0.0874	68.174
Mean GM	0.0652	0.5687	31.5367	1.0231	0.6441	0.267	307.8812
std	0.0062	0.0255	6.6722	0.1658	0.0601	0.0866	54.7103

Hypothesis testing: t-test2							
h	1	1	1	1	1	1	1
p-value	1.08E-81	1.31E-48	1.20E-28	3.46E-10	9.28E-08	2.50E-17	1.25E-83
Δ parameter	0.0433	0.08735	-11.5737	0.16335	-0.05975	0.13125	385.0863
ci	0.0411	0.0793	-13.2426	0.1152	-0.0808	0.1041	365.7837
	0.0455	0.0954	-9.9048	0.2115	-0.0387	0.1584	404.3888

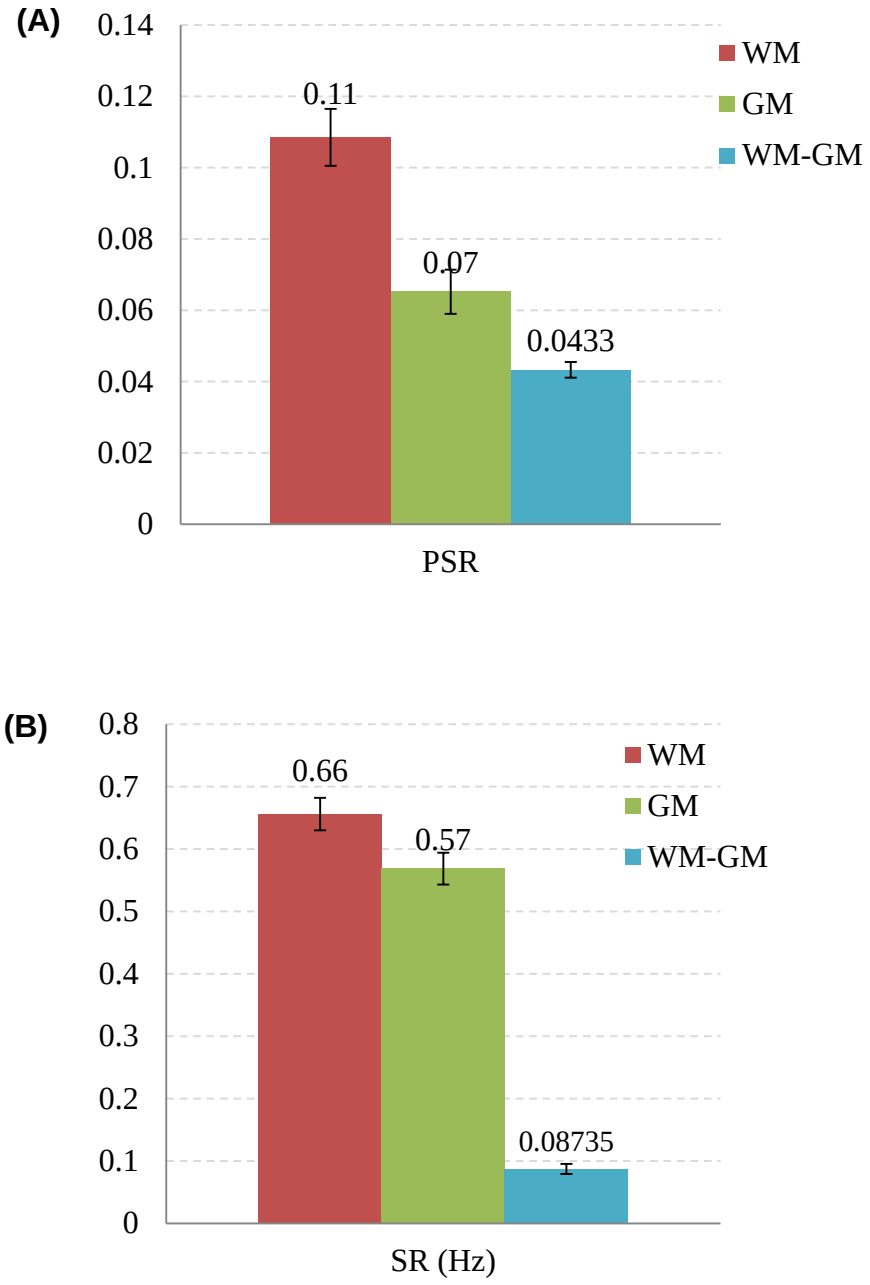

Figure 2-20. WM and GM contrast for PSR (A) and SR (B). The means from GM (green) and WM (red) ROIs from 8 rats, each rat with 10 ROIs each. The error bars indicate the standard deviation for WM and GM. The difference (WM-GM), i.e. the blue bar, denotes the difference in GM and WM and error bars indicate 95% confidence interval on the difference.

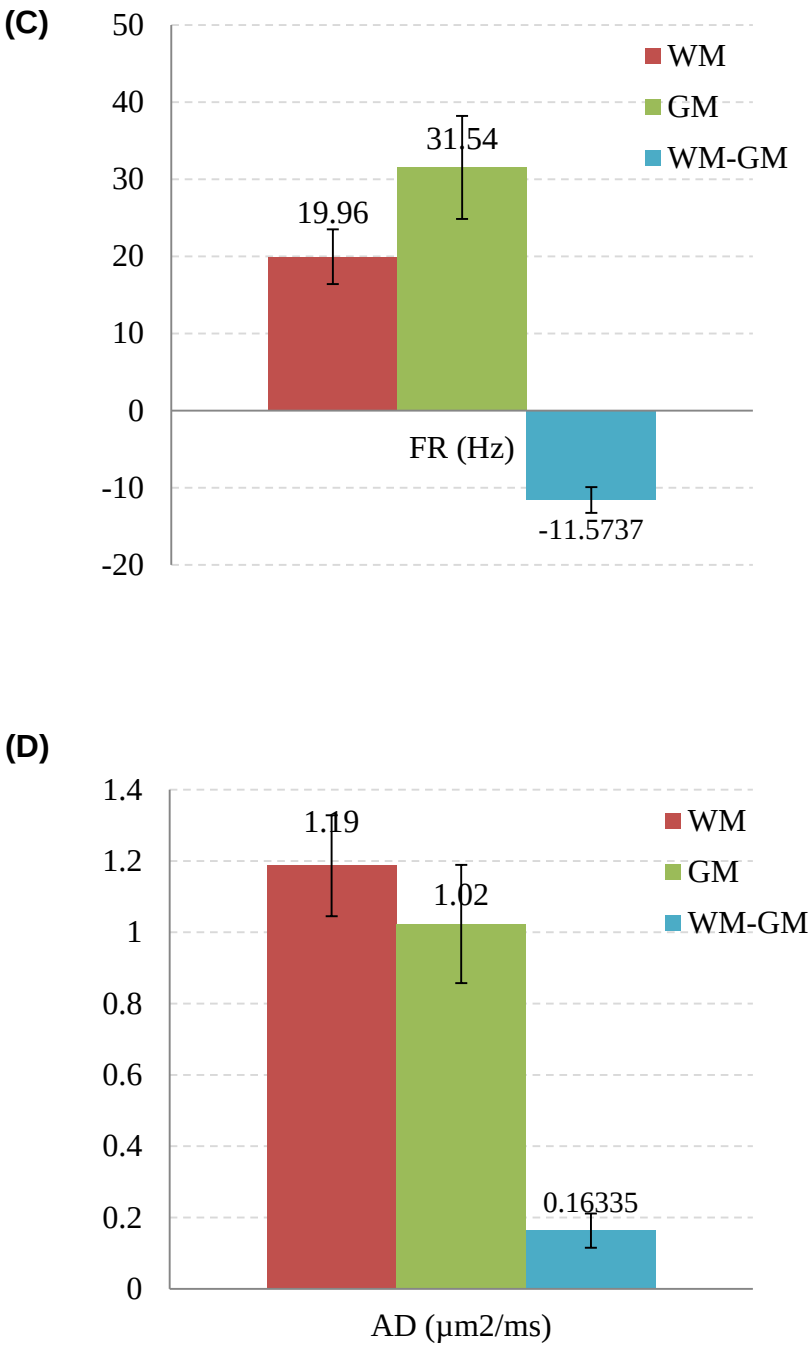

Figure 2-21. WM and GM contrast for FR (C) and AD (D). The means from GM (green) and WM (red) ROIs from 8 rats, each rat with 10 ROIs each. The error bars indicate the standard deviation for WM and GM. The difference (WM-GM), i.e. the blue bar, denotes the difference in GM and WM and error bars indicate 95% confidence interval on the difference.

(E)

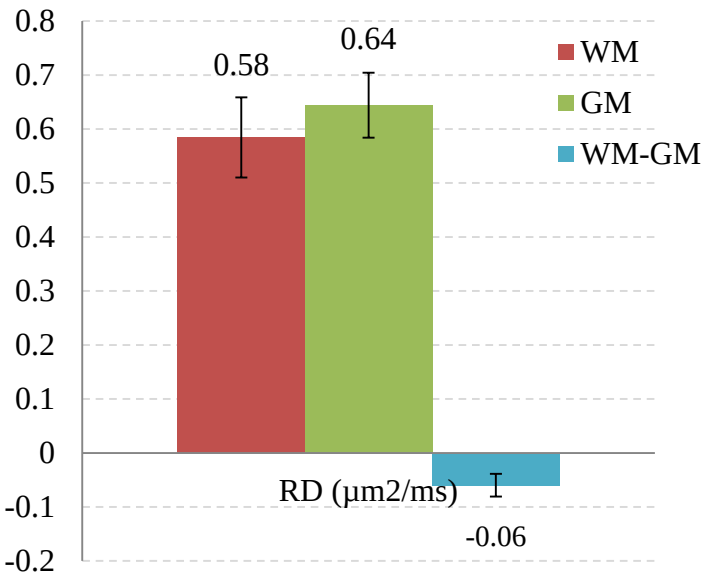

(F)

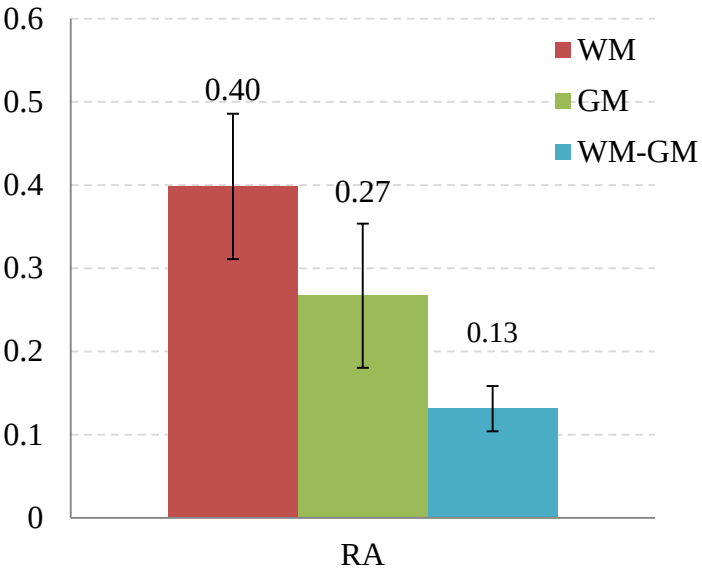

Figure 2-22. WM and GM contrast for RD (E) and RA (F). The means from GM (green) and WM (red) ROIs from 8 rats, each rat with 10 ROIs each. The error bars indicate the standard deviation for WM and GM The difference (WM-GM), i.e. the blue bar, denotes the difference in GM and WM and error bars indicate 95% confidence interval on the difference.

(G)

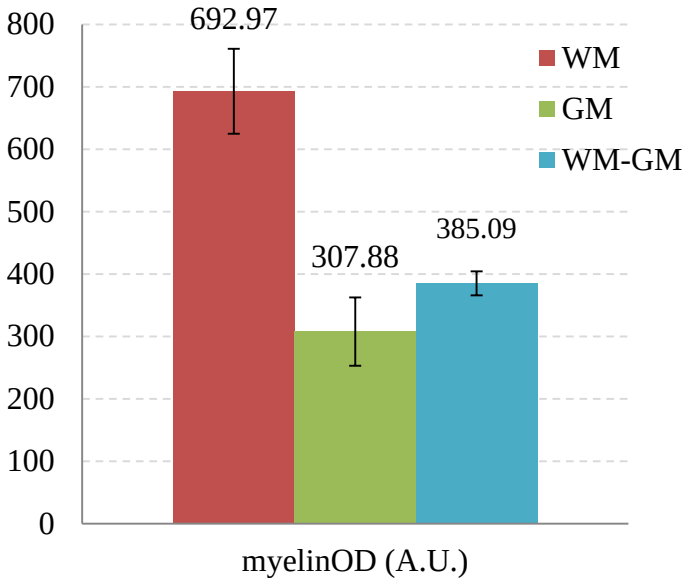

(H)

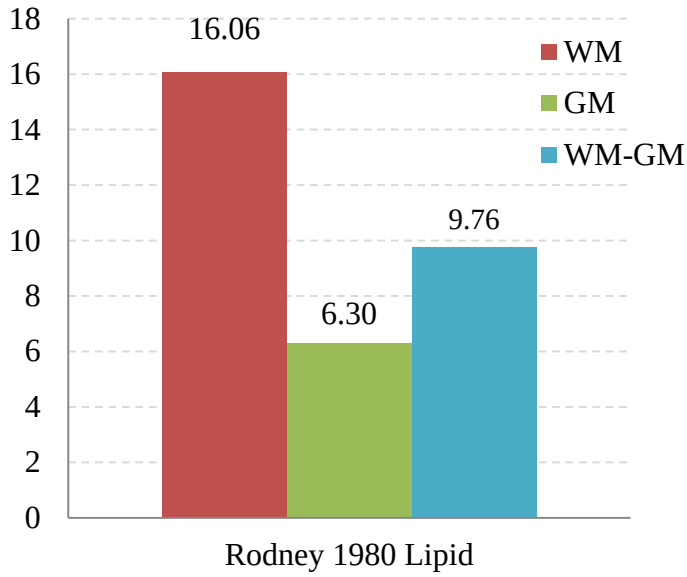

Figure 2-23. WM and GM contrast for myelin optical density (G) and Rodney 1980 Lipid Profile (H). The means from GM (green) and WM (red) ROIs from 8 rats, each rat with 10 ROIs each. The error bars indicate the standard deviation for WM and GM. The difference (WM-GM), i.e. the blue bar, denotes the difference in GM and WM and error bars indicate 95% confidence interval on the difference.

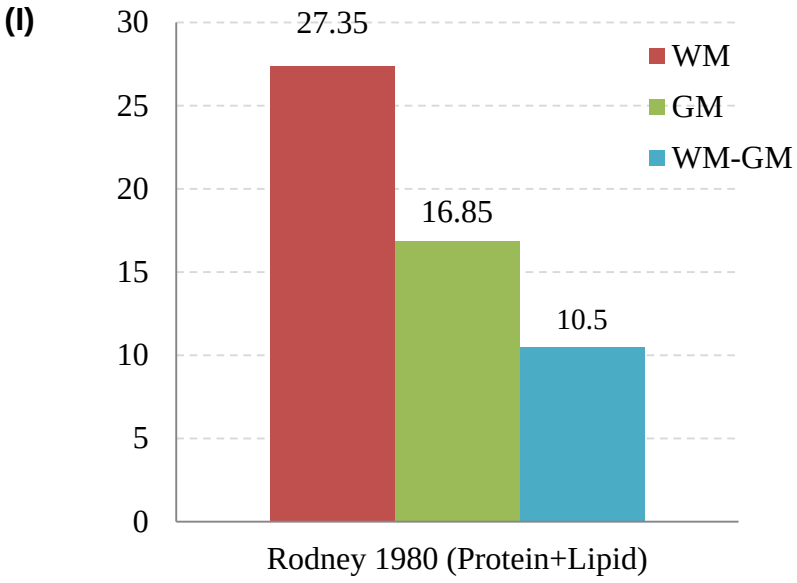

Figure 2-24. WM and GM contrast for Rodney 1980 Total Protein and Lipid Profile (I). The means from GM (green) and WM (red) ROIs from 8 rats, each rat with 10 ROIs each. The error bars indicate the standard deviation for WM and GM. The difference (WM-GM), i.e. the blue bar, denotes the difference in GM and WM and error bars indicate 95% confidence interval on the difference.

Discussion

Few studies have investigated demyelination utilizing multiple quantitative imaging techniques and have validated the qMRI parameters with histological myelin content e.g. (Dula et al., 2010a; Samsonov et al., 2012). qMT and DTI are commonly employed techniques given their sensitivity to myelin. In this chapter, we have employed both qMT and DTI techniques to determine their comparative performance for detecting demyelination *in vivo* using a LPS induced rat model of type III MS lesions. Our results have revealed that under the given pathological conditions, of the two techniques, qMT has a stronger correlation with myelin content as compared to DTI. As such, these results indicate that as compared to RD (DTI), PSR (qMT) has a greater sensitivity to detect *in vivo* myelin content.

The key findings of our study are that the qMT parameter, PSR, shows strongest and significant correlation with histological myelin content in the acquired dataset, which includes white and gray matter. Additionally, PSR shows the highest contrast between gray and white matter among the qMRI parameters. However, separate WM and GM analyses, in general, revealed no strong or significant correlations within WM or within GM with histological myelin content. This was the major limitation of our study, and thus we could not extensively quantify demyelination within WM. However, after increasing the dynamic range in myelin content variation by including GM, as previously utilized by Underhill and colleagues (2011) (Underhill et al., 2011), we observed a significant correlation between all the qMRI parameters and histological myelin content.

Among the qMT and DTI parameters investigated for contrast between WM and GM, PSR showed the highest contrast (66%) followed by the diffusion anisotropy measure, RA (49%). The anisotropy information is widely used for tracking white matter fibers. In addition, diffusion anisotropy measures (fractional anisotropy and relative anisotropy) are routinely used for segmentation of white matter. Although DTI is a promising technique, the diffusion anisotropy is dictated by structural features and geometry of white matter fibers. Thus, diffusion anisotropy measures were affected by structural features such as crossing white matter fibers, which would lead to loss of contrast between white matter and the surrounding tissue. On the other hand, the contrast in PSR parameter maps is driven by differences in macromolecular content, such as myelin. The contrast observed in PSR parametric maps is dictated by tissue composition and thus may provide composition based tissue segmentation. The excellent contrast seen in PSR parametric maps in our study suggests that PSR is a good candidate for applications such as white matter segmentation.

The PSR profile in GM and WM observed in our study resembles the total protein and lipid composition in brain as reported by Rodney et al. (1980) (Gore et al., 1981; Rodney et al., 1980) (see Figure 2-20). PSR is a two-pool MT model parameter that reflects the fraction of exchanging macromolecular protons with the free water protons. Both proteins and lipids contribute to this macromolecular proton pool, thus the resemblance of PSR profile in GM and WM with the total protein and lipid composition is consistent with the two-pool MT model. In WM, myelin is the major contributor of proteins and lipids. In GM, where myelin is in much smaller quantities, contributions from other tissue components (membranes, glial cells) to the total protein and lipid content is significant. Although the resemblance in the PSR profile is consistent with the total protein and lipid content, there are other factors that could lead to the

observed PSR profile and needs clarification. For example, previous studies (Fralix et al., 1991; Koenig, 1991; Kucharczyk et al., 1994) have shown evidence towards heterogeneous contributions of different myelin lipid components to the MT contrast. Thus, the resemblance observed might be a coincidence. Further studies are needed to explore these relationships in detail.

It is interesting to note that in our study while PSR resembles the total protein and lipid profile in the brain, the histological myelin content measured in our study also resembles the total lipid profile reported by Rodney and colleagues (1980) (Gore et al., 1981; Rodney et al., 1980). The myelin content in our study was quantified by transmitted light microscopy of LFB stained slides. LFB primarily stains phospholipids (Kluver and Barrera, 1953) and is found to be suitable for myelin quantification due to its stoichiometric properties, which allows linearity between myelin content and transmitted light (Salthouse, 1962; Scholtz, 1977). Although, LFB primarily stains phospholipids, prolonged formalin fixation increases the probability of staining other tissue components such as proteins (Scholtz, 1977). Furthermore, LFB staining does not have the specificity of immunohistological stains (Bodhireddy et al., 1994). Given these potential lack of specificity in our LFB staining, further studies will be needed to investigate the association between the lipid profile in brain tissue and LFB histology.

T2w images are the workhorses for clinical MRI examination as they have a high sensitivity towards MS lesions and are included in the McDonald Criteria for the diagnosis of MS (Polman et al., 2011). In fact, the number of lesions seen on T2w images is an important component for MS diagnosis (McDonald et al., 2001; Polman et al., 2011; Polman et al., 2005b). Based on this clinical precedence, we used T2w FSE images to locate the injection site and LPS-induced

lesions. However, we had limited success in detecting LPS-induced lesions using T2w FSE images. In clinical T2w FSE images, acute MS lesions appear hyperintense due to inflammation. However, the limited success of our T2w FSE images may have been due to the non-inflammatory and primarily demyelinating lesions in our type III MS lesion rat model. We thought that the tissue damage resulting from the needle track at the injection site in CC would aid in locating the injection site and qMRI slice prescription for axial images. However, the needle track was not clearly visible in axial slices from most rats, as shown in Figures 2 and 3. In such cases, the coronal slice located just beneath the skull was the most reliable means to locate the needle track and the injection site. However, the separation of a few mm between skull and CC may result in errors positioning the qMRI slice accurately when the needle track was not visible. Though good contrast was observed between gray and white matter regions in T2w FSE images, it was not observed between the lesion site (as confirmed by histology) and the surrounding tissue. Thus, in our animal model the extent and location of the lesions were unclear in the T2w FSE images even though they are routinely used for clinical examination. We speculate that these observations could be due to the small size of lesions, limited resolution of MRI images, and partial volume effects from neighboring imaging voxels. Furthermore poor reproducibility (only two of six LPS injected rats showed prominent demyelination in histological examination) and limited severity of LPS induced lesions suggests presence of other confounding factors not directly related to performance of T2w images that could contribute ineffectiveness of T2w images for our animal model.

Although strong and significant correlations were observed in cumulative gray and white matter group analysis, we were also interested in associations with histological myelin content within WM and within GM. This lack of correlation may be attributed to true physiological

characteristics of CNS tissue or an artifact due to loss in experimental precision. Further investigation revealed several factors that could contribute to the poor correlations observed. These include greater MRI slice thickness (1 mm) compared to lesion spread, limited in-place resolution on MRI (~260 μm/pix), motion related issues during MRI scan, as well as poor correspondence between MRI and histological slice leading to co-registration. We discuss these study limitations and factors identified that could contribute to the increase in uncertainty in correlation measurements below, along with the implementation of remedial measures in the next chapter.

For this study, we utilized SIR-qMT, a variation of the qMT technique. The advantages of the SIR-qMT method include its utilization of low-power pulses that does not depend upon explicit assumptions on macromolecular pool lineshape and separate acquisition of B1 and B0 field maps (Gochberg and Gore, 2007a). Despite these advantages, as we investigated the lack of GM and WM correlations with histological myelin content, we determined that our current SIR-qMT methodology could have contributed to the increased uncertainty in the observed correlations. We think that this may have been the case given the suboptimal precision and increased imaging times that the current SIR-qMT provided. As such, in our subsequent studies that will be discussed in Chapter 3, we optimized our SIR-qMT methods to enhance the SIR-qMT precision and time efficiency so as to decrease the variability of measured qMT parameters and increase the signal-to-noise ratio, respectively. Furthermore, we decreased approximations using exchange rate as compared to T1f relaxation to fit the data to a more precise qMT model which revealed the fundamental tissue parameters (Gochberg and Gore, 2007a).

In our *in vivo* study, the aim of detecting demyelination following LPS injection into the CC was not achieved. Within WM no strong correlations were observed, however, we were able to show strong correlations with myelin content by increasing the dynamic range of myelin content through inclusion of GM ROI's. Probable causes for the lack of correlations within WM include: poor lesion reproducibility, limited lesion size and severity, partial volume effects (resolution, slice thickness, neighboring tissue characteristics greatly differ [CSF near lesion site], motion), high SNR requirement (limited parameter precision), and limited *in vivo* imaging time (limits SNR, resolution, use of gating to compensate motion). Our subsequent work, discussed in Chapter 3, addressed these potential issues.

Another potential contributor to the lack of correlation observed within WM is partial voluming effects. Partial voluming effects can lead to loss of sensitivity in quantitative measurements by reducing the ability to detect small changes in qMRI parameters due to signal contamination from neighboring image voxels. This neighboring image voxel contamination is further increased if the structure of interest is a few pixels wide, thus having a high boundary to volume pixel ratio. Furthermore, the neighboring image voxel contamination may also increase if there are greater differences in the neighboring tissue properties. The location of CC presents these challenges as the CC is adjacent to gray matter and CSF filled ventricles are likely to contaminate the signal from MRI voxel. Furthermore, partial voluming effects may have also contributed to the increased uncertainty in observed correlation measures as the CC is a very thin brain structure with an in plane thickness ranging from 0.5-1 mm and, at an imaging resolution of 250 μm, the CC is only 2-4 pixel thick. Due to the small size of the CC, the boundary to volume pixel ratio is large making it prone to smoothing the inherent parameter variations in lesion sites within the CC.

In an effort to reduce the partial volume effects in the slice direction on the quantitative parameter maps, the qMRI slice prescription was made perpendicular to CC. Partial voluming effects can be reduced by decreasing the MRI slice thickness and in-plane resolution. The limited imaging time for *in vivo* experiments and higher SNR requirement for qMRI measurements pose a tradeoff. Additionally, the slice profile effects in 2D MRI sequences also contributed to partial voluming. This situation is made more challenging by the fact that the LPS induced lesions were thin (only effecting 1/2 to 1/3 of CC width). Moreover, motion during imaging (that is, bulk and pulsation due to the cardiac cycle) can also induce artifacts which we reduced by cardiac gating at the expense of increasing the imaging time. We used this cardiac gating scheme when severe artifacts were seen in DTI measurements.

To address the above discussed issues, an *ex vivo* protocol was designed (subject of Chapter 3) as an *ex vivo* protocol widens the imaging time window significantly. Given that our scanning time is limited by scanner availability, we performed our *ex vivo* protocols using overnight scans. 3D sequences were implemented for both DTI and qMT measurements. 3D sequences alleviated slice profiling artifacts, which is an issue for the thin slices (167 µm) that we used for these experiments. Higher SNR from 3D sequences can be traded to gain image resolution, which is essential to avoid partial voluming effects and image the demyelination within the thin CC. Given that we are imaging a thin brain structure (CC), the choice of resolution is dictated by the smallest anatomical feature, which is the demyelinated region of the CC. As such, a 1/6 mm isotropic resolution was chosen to give 3-6 pixels along the width of the CC to reveal demyelination pattern and reduce partial voluming effects.

Conclusion

In summary, we performed quantitative *in vivo* qMT, DTI, as well as histological measurements in an animal model of type III MS lesions. Quantitative metrics from qMT and DTI were correlated against histological measures of myelin obtained from light microscopy of LFB stained tissue. This validation study intended to compare the *in vivo* sensitivity of qMT and DTI metrics with myelin histology. The results of these studies validated the *in vivo* specific sensitivities of qMT and DTI to demyelination and showed that PSR has the strongest correlation with histological myelin content.

Higher resolution and more conclusive results obtained using *ex vivo* rat brains are presented in the next chapter. The *ex vivo* results carry greater confidence levels to match the true physiological correlations. In this chapter, we were able to show *in vivo* correlations between quantitative MRI and histology between a GM and WM region. The factors influencing correlations and steps taken to address these are discussed in the next chapter.

CHAPTER III

Ex vivo qMTI and DTI in MS animal MODEL: Exploring sensitivity and specificity of qMT and DTI to myelin

In the previous chapter, we have investigated the *in vivo* correlations of qMT and DTI parameters with quantitative myelin histology in an LPS animal model of MS. However, small size of the corpus callosum needs longer imaging time to achieve the required SNR for qMT and DTI while maintaining high resolution to keep the partial volume effects from neighboring ventricular spaces at minimum. Moving to the *ex vivo* tissue, we are not limited by the scan time of keeping the animal alive. In addition, we are not limited to acquiring a single 2D imaging slice for qMRI. Hence, we implemented 3D SIR-FSE3D and 3D SE3D sequences for qMT and DTI, respectively, with improved resolution and SNR compared to *in vivo* imaging.

Introduction

Multiple sclerosis (MS) is the most common inflammatory demyelinating disease of the central nervous system (CNS), and MRI is the prominent modality to detect MS lesions. Conventional relaxation-weighted imaging of MS can track inflammation and the number and volume of lesions, but is not specific to different pathological tissue states such as axonal loss, Wallerian degeneration, gliosis, inflammation and demyelination. Quantifying the extent of demyelination

in particular has important clinical implications in monitoring disease progression, treatment planning, and drug response. Hence, while remaining an important tool for diagnosis, current MRI metrics are imprecise predictors of pathology, disease progression or response to therapy and more specific quantitative methods are needed.

qMT and DTI are quantitative methods with sensitivity to demyelination (Schmierer et al., 2004; Song et al., 2005; Stikov et al., 2011; Underhill et al., 2011). Specifically, previous studies have shown that the DTI parameter radial diffusivity increases in dysmyelinating and demyelinating animal models (Shamy et al., 2010; Song et al., 2002; Song et al., 2005), while an increase in axial diffusivity correlates with axonal damage but not with demyelination (Song et al., 2005). Similarly, magnetization transfer imaging measured magnetization transfer ratio (MTR) and pool size ratio (PSR) mapped with qMT have been shown to correlate with histological measures of demyelination (Deloire-Grassin et al., 2000; Ou et al., 2009; Rausch et al., 2009; Schmierer et al., 2004). However, MTR is also sensitive to variations in acquisition protocols (such as the irradiation power) (Berry et al., 1999a, b) and to changes in parameter values that have no direct connection to magnetization transfer (such as the free water relaxation rate, $R1_f$). Instead, metrics derived from quantitative methods are needed to isolate the biophysical changes underlying white matter damage and to make comparisons across subjects and centers. Hence, in this study we have limited ourselves to a qMT method (Gochberg and Gore, 2003, 2007b; Li et al., 2010) that images several underlying tissue characteristics, including the PSR.

The current study was designed to examine the qMT and DTI metrics, which closely reflect the underlying pathology of demyelination. While both methods have shown sensitivity to demyelination, they are based on distinct tissue models and are indirect measures of myelin

content. Hence, correlating these quantitative metrics of MRI with histological measures of myelin content (and with each other) in a range of pathologies is necessary to reveal their relative sensitivity and specificity towards demyelination.

There are different animal models of MS each addressing different patho-physiological aspects of MS lesions in humans. In the experimental autoimmune encephalomyelitis (EAE) model, immunization of animals with myelin oligodendrocyte glycoprotein (MOG) induces high levels of inflammation due to infiltration of mononuclear myelin-specific CD4 T-cells, resulting in moderate to severe axonal damage but only minor primary demyelination. Toxin-induced models show focal demyelination (e.g. local injection of lysolicithin) or diffused demyelination (e.g. animals fed with cuprizone admixed chow), but typically lack substantial T cell infiltration. Thus, both EAE and toxin based animal models deviate from MS pathology in humans, limiting the applicability and relevance of results. Similarly, while the chronic Theiler's viral model of demyelination shows features of demyelination, the inability to identify a viral pathogen in MS has reduced the enthusiasm for this model. Also, the majority of the pathology in the Theiler's virus model is seen in the spinal cord, which has made imaging of lesions difficult.

We instead used a model of CNS demyelination, which followed the intracerebral injection of lipopolysacharide (LPS). Injection of LPS into the central nervous system (CNS) results in recruitment of macrophages, followed by demyelination that is similar to that of a progressive oligodendrogliopathy (Felts et al., 2005). This animal model oligodendrogliopathy reflects features that are similar to the primary oligodendrogliopathy, which is seen in a subset of patients with MS. The pathological features show apoptotic death of oligodendrocytes and relative absence of prominent lymphocytic infiltration. Following intracerebral injection of LPS

into the corpus callosum, demyelination is maximal 20-28 days post injection (Sriram et al., 2012). There are no therapies for this form of oligodendrogliopathy.

Development of newer strategies to treat MS will be facilitated by better methods to characterize changes that are typical of primary oligodendrogliopathy. To our knowledge, this is the first quantitative magnetic resonance myelin study of a LPS mediated rat model of Type III MS lesions.

In this study, we present correlations of high-resolution 3D qMT and DTI matrices (167μm isotropic) with quantitative Luxol fast blue-periodic acid Schiff (LFB-PAS) stained histology in a model of CNS demyelination which shows features of MS.

Methods

In Vivo injection of LPS into Corpus Callosum

To induce focal lesions nine rats were injected intracerebrally with LPS (n=8) or an equal volume of saline (n=1) into the corpus callosum (CC). In one of the LPS injected rats (#3), the injection missed the CC, which was hence not affected. This animal was excluded from the analysis. Rats were anesthetized and positioned in a small-animal stereotaxic apparatus (David Kopf Instruments, Tujunga, CA) to conform to the brain atlas. Microinjection of LPS (Escherichia Coli serotype 055:B5) into the corpus callosum was performed with a 32-gauge needle through a dentist's burr hole. To perform the injection into the corpus callosum, the following coordinates were used: 1 mm posterior from bregma, 1 mm lateral from the sagittal suture, and 3.3-3.5 mm

below the dura mater. LPS-treated rats received five µl of saline containing five µg of LPS using a microinjection pump over 15 minutes. The needle was then held for an additional 10 minutes after injection.

Fixation

28 days post-injection, rats were perfused with the PBS/saline solution followed by 4% paraformaldehyde fixation. Rat brains were excised and soaked in about ten times the volume of 1X (PBS)Phosphate Buffered Saline solution for a period of 24hrs prior to *ex vivo* qMT imaging. Rat brains were then soaked for an additional 1week in 1mM Gd-DTPA/PBS solution to improve the time efficiency of *ex vivo* DTI scans (D'Arceuil et al., 2007). Due to scheduling constraints rats 2, 7, and 9 were imaged about a month later for *ex vivo* DTI. During this time, the brains were stored back in PBS solution before transferring back in 1mM Gd-DTPA/PBS Gd-doping solution one week prior to imaging. All experimental procedures were approved by Vanderbilt University's animal care committee (IACUC).

Data acquisition

Ex vivo MRI, acquisitions were performed on a 9.4T Varian scanner. The rat brains were imaged at 3D high resolution (167µm isotropic using a 192x96x96 imaging grid). qMT and DTI scans were performed on the perfusion fixed brains, in a custom brain holder in fomblin. Fomblin prevents tissue dehydration, provides susceptibility matching, and (being proton free) has no background signal. The qMT scans were performed using an optimized selective inversion recovery method with a five point scheme requiring 15s/shot shown below (Gochberg and Gore, 2007b; Li et al., 2010), eight echos with the kspace zero line on the first echo, eight

additional pulses at the end of echo train after acquisition to ensure zero z-magnetization, two averages and a total scan time of 10hrs.

Table 3-1. ti and td value for optimized 5-pt SIR-qMT method

	1	2	3	4	5
ti(s)	0.006	0.032	0.035	0.225	0.77
td(s)	3.502	4.603	1.507	3.273	0.11

DTI scans on Gd-doped brains were performed using 3D PGSE, with a b-value of 1157s/mm^2, TE/TR=29/250 ms, six diffusion sensitizing gradient directions of (x,y,z) = (0,0.707,0.707), (0.707,0,0.707), (0.707,0.707,0), (0,-0.707,-0.707), (-0.707,0,-0.707), (-0.707,-0.707,0) and an additional image with no diffusion sensitive gradients (Basser and Pierpaoli, 1998), 2 averages and a total DTI acquisition time of 8.5hrs/sample.

Histopathology

4mm coronal tissue sections containing the injection were excised matching the area diagrammed in Fig. 1 aided by the visible markers as discussed below. The section was blocked in paraffin, sectioned in 10μm slices, stained with Luxol fast blue (LFB) or Luxol fast blue-periodic acid Schiff (LFB-PAS), and quantified by optical opacity. To account for minor animal to animal differences in light microscopy of LFB stain intensity, the myelin count as measured by light microscopy of the LFB stain was normalized with Internal Capsule (IC) as internal reference and by setting pseudo-maximum calculated as average of top 100 pixels in IC w.r.t. myelin content to 200. This approach was predicated on the assumption that at IC in each rat was unaffected by LPS injection, which appears to be the case from gross visual inspection.

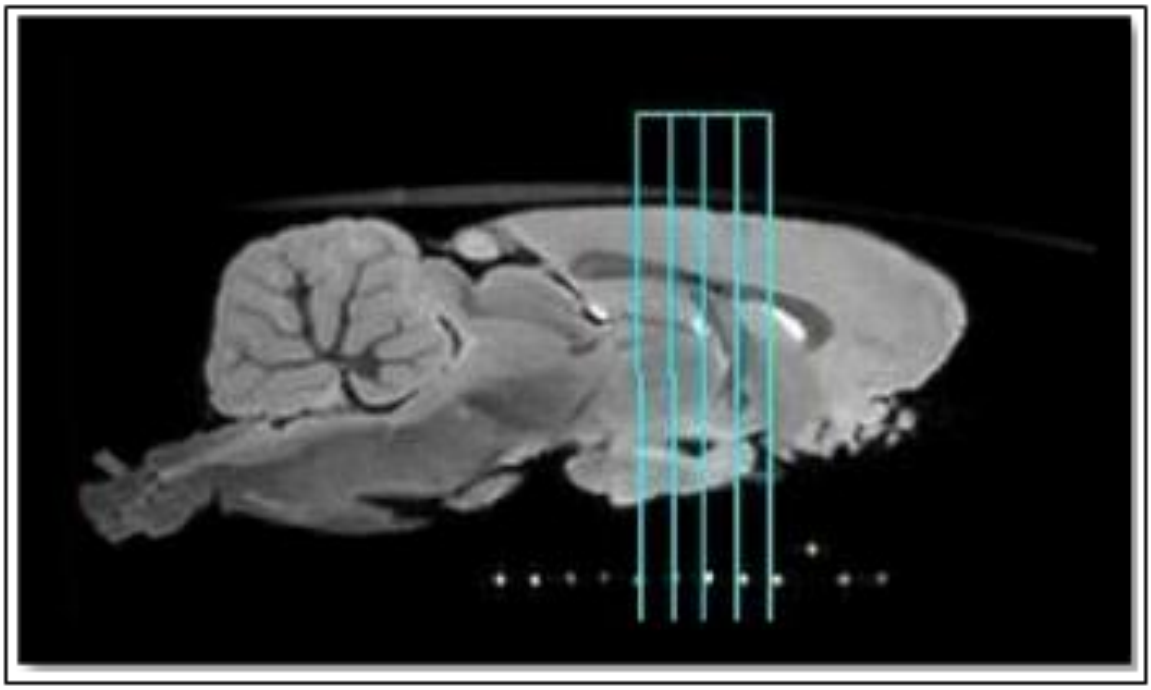

Figure 3-1. 4 mm tissue slab extracted for histology on *Ex vivo* T2* weighted sagittal slice. Representative sagittal slice from *ex vivo* T2* weighted 3D gradient echo image, which was used for anatomical positioning. qMT and DTI imaging data was taken within the 4mm axial slab (outlined in cyan), which was removed for histology. The capillary markers (white dots) ensured that the MRI and histology slices matched.

Co-registration

Co-registration of 3D qMT dataset to 3D DTI dataset was performed using affine registration programs written in Matlab maximizing the mutual information (Viola and Wells, 1997). Co-registration between MRI and histology is challenging, since the histology preparation can result in shrinkage, folding, and tearing of the brain tissue. In order to facilitate such co-registration, all MRI images were taken with the *ex vivo* brain secured in the brain cast used for slicing histology sections. While the plastic brain matrix was not directly visible in the MRI due to its short T2, capillary markers filled with doped water were incorporated into the cast and used to ensure the histology slab was cut at an angle matching the MRI imaging geometry. (These markers are visible at the bottom of Figure 3-1.) This reduced co-registration to a one-dimensional problem. The MRI slice that contained the injection site was then visually matched to the histology slice using the injection needle mark and anatomical similarity. The accuracy of the co-registration varied with the location, but was on the order of a couple pixels, motivating our use of six 1 mm (± 1 pixel or 167μm) ROI's (three on either side of the midline) within the CC as illustrated in Figure 3-2.

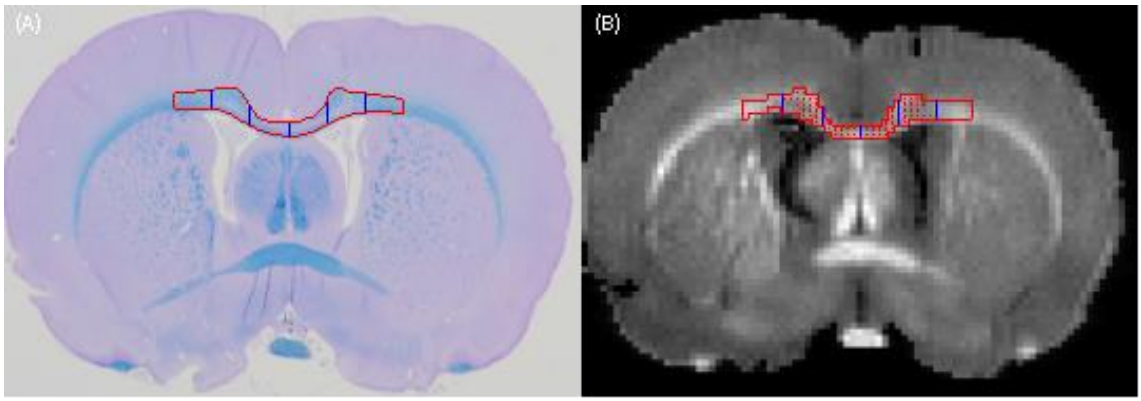

Figure 3-2. Segmentation of corpus callosum. Red outline indicates the ROI in CC selected for analysis and blue vertical lines mark the separation of 1mm ROI's from midline. (A) LFB/PAS, (B) PSR (segmented from raw qMT image)

Statistical analysis

Pearson's correlation coefficients were calculated using mean ROI values for MR and histological matrices using Matlab.

Results

LFB/LFB-PAS staining confirmed demyelination in proximity of the injection site (and often extending along white matter tracts to the contralateral hemisphere, as seen in Fig. 3) in the CC of LPS injected rats, but not all LPS injected rats showed demyelination to a comparable severity and regional expanse. We found that five LPS injected rats had severe and extended demyelinated lesions and two rats (#4 and 5) had no/mild demyelination, which we grouped in our analysis with the saline injected control (#2). The above observations suggest that the LPS injected rat model response is likely to vary depending on individual animal.

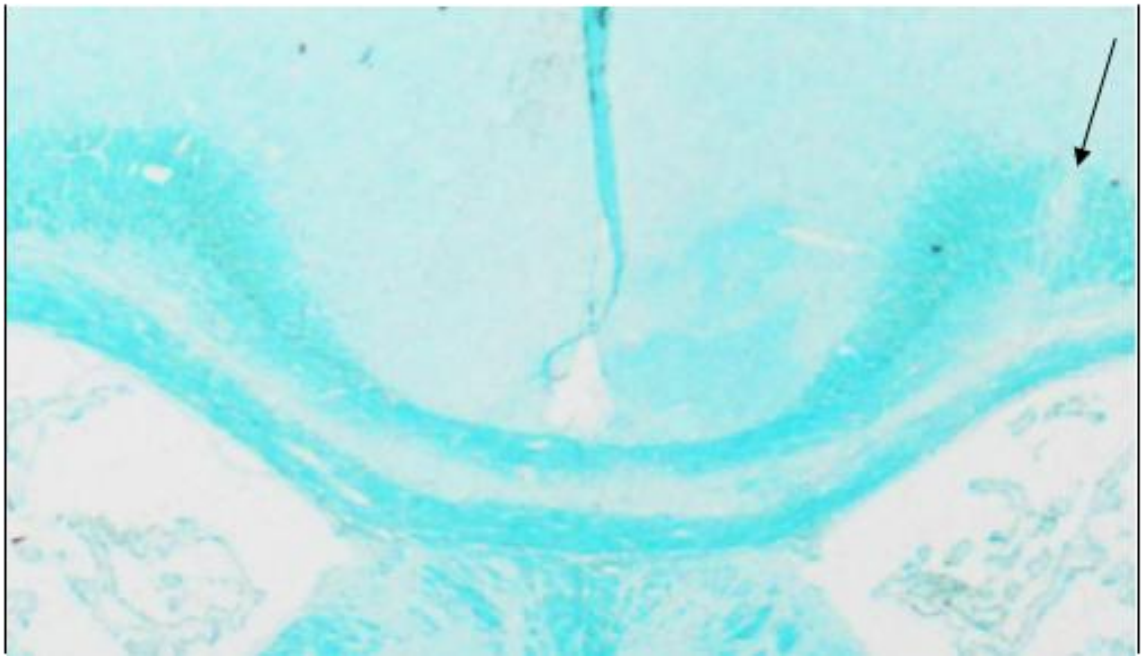

Figure 3-3. Light microscopy of demyelination on LFB stained section. Representative LFB stained slice. Arrows indicate site of injection. The loss of LFB staining in Trunk of the corpus callosum is indicative of demyelination

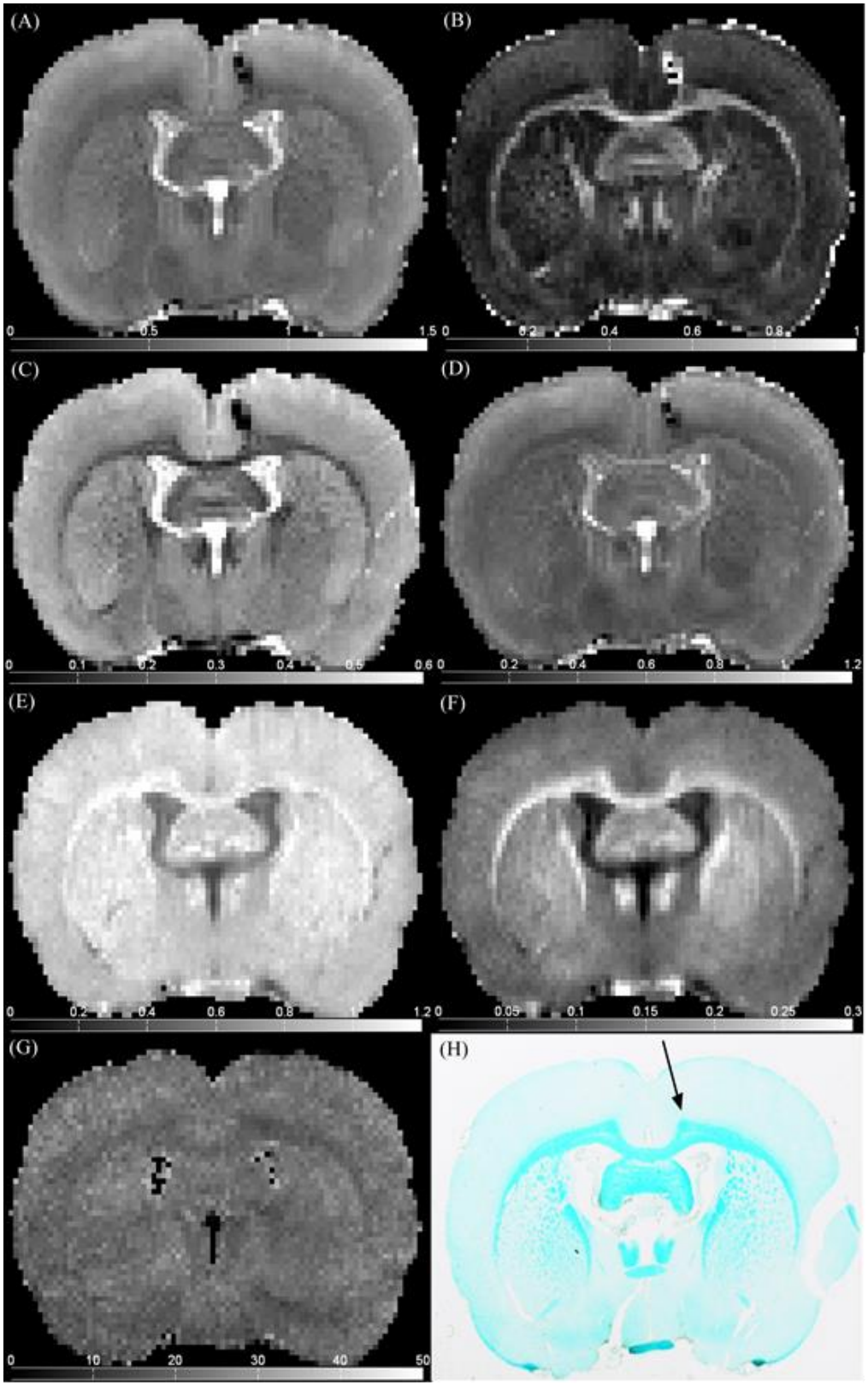
(A)
0
0.5
1
1.5
(B)
0
0.2
0.4
0.6
0.8
1
(C)
0
0.1
0.2
0.3
0.4
0.5
0.6
(D)
0
0.2
0.4
0.6
0.8
1
1.2
(E)
0
0.2
0.4
0.6
0.8
1
1.2
(F)
0
0.05
0.1
0.15
0.2
0.25
0.3
(G)
0
10
20
30
40
50
(H)

Figure 3-4. qMRI parameter maps and myelin histology. Representative (A) D_{avg}, (B) FA, (C) RD, (D) AD, (E) R_{1f}, (F) PSR, (G) k_{mf}, maps and (H) LFB histology, at injection site location.

Figure 3-4 illustrates representative *ex vivo* qMT and DTI parameter maps in a coronal slice containing the injection site indicated by the black arrow in Fig. 4(H). Note in particular the strong gray/white matter contrast relative to noise for RD (Fig. 4C) and PSR (Fig. 4F).

The correlation of qMT($R1_f$, k_{mf}, and PSR) and DTI (RD, AD, FA and D_{avg}) metrics with myelin content as measured by LFB histology with light microscopy are shown in Figure 3-5. Each point represents a 1mm section along the corpus callosum starting from the mid line (sagittal suture), traversing 3mm on both side and giving 6 data points/rat. The results from the saline injected rat (#2) and two LPS rats with minimal demyelination (#4 and #5) are plotted in blue, while all other LPS rats are plotted in red.

The key result is that PSR clearly separates demyelinated from normal white matter. The separation between demyelinated lesions and normal white matter corresponds to ~200 A.U. in LFB histology, i.e. the normalized histological myelin count for non-lesioned rats and normal appearing sections of lesioned rats ranged from about 200-256. PSR showed the clearest separation between lesioned and non-lesioned regions, with lesioned regions having a PSR less than about 0.2 (Fig 5. b). In addition, a strong linear correlation is observed within lesion areas between PSR and LFB myelin histology. Thus, PSR can distinguish between different degrees of demyelination within the LPS induced lesions. RD correlates negatively with LFB. However, this correlation is weaker than it is for PSR. Fig. 6 summarizes the correlations with Pearson coefficients for all qMT and DTI parameters vs LFB light microscopy measurements of myelin content for lesioned and for combined lesioned and non-lesioned samples. The bulk of

this correlation is due to variations in lesion severity, and hence there are similar correlation coefficients using only lesion rats vs. using all rats. Non-lesioned rats showed much weaker correlations of MR metrics with histological myelin count likely due to the restricted range of histological myelin count values.

Of all the qMT parameters, PSR has the strongest correlation with myelin histology (Pearson's r = 0.83, $p < 0.00001$). Likewise, RD has the strongest correlation ($r = -0.57$, $p < 0.001$), of the DTI parameters. Fig. 7 illustrates the connection between qMT and DTI measures of the myelin by correlating DTI parameters (RD, AD, FA, and D_{avg}) to PSR and qMT parameters (PSR, k_{mf}, and $R1_f$) to RD. (Correlations between parameters within a single imaging protocol are inherently high but less meaningful due to similar dependencies on the underlying data, e.g. AD and D_{avg} have similar analytic dependencies on the eigen values). No significant correlations were observed for non-lesion rat samples.

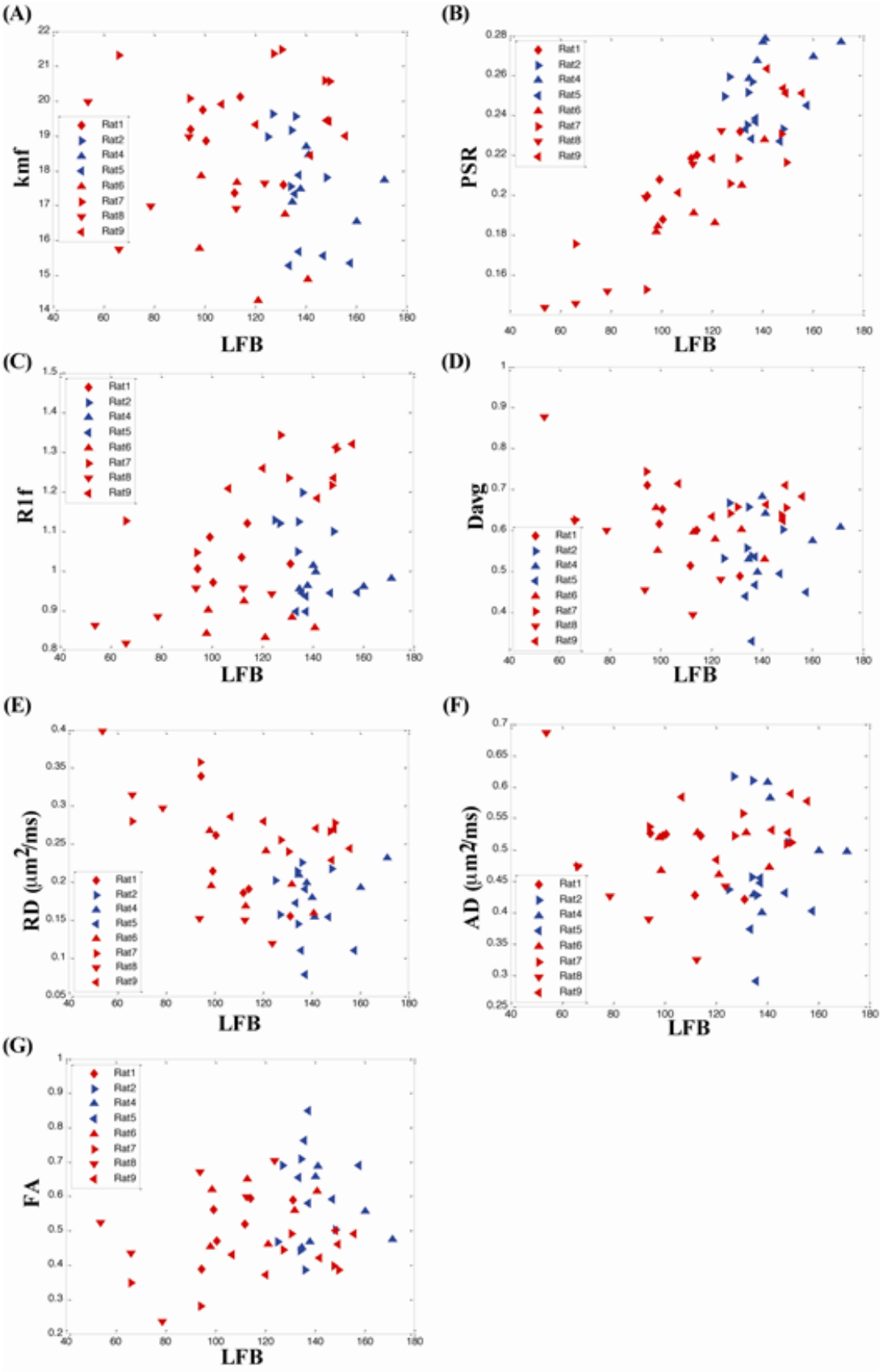
(A)
kmf
LFB
(B)
PSR
LFB
(C)
R1f
LFB
(D)
Davg
LFB
(E)
RD (μm²/ms)
LFB
(F)
AD (μm2/ms)
LFB
(G)
FA
LFB
Rat1
Rat2
Rat4
Rat5
Rat6
Rat7
Rat8
Rat9

Figure 3-5. Correlation of qMRI parameters with histological myelin count. qMT and DTI parameters vs myelin count from LFB histology demonstrate correlations in CC of lesion (red) and non-lesion (blue) rats. qMT: (a) k_{mf} vs LFB, (b) PSR vs LFB, (c) R_{1f} vs LFB and DTI: (d) D_{avg} vs LFB, (e) RD vs LFB, (f) AD vs LFB, (g) FA vs LFB. PSR shows a strong positive and RD shows strong negative correlation with myelin content measured by LFB histology. Each point represents a 1mm ROI in the CC.

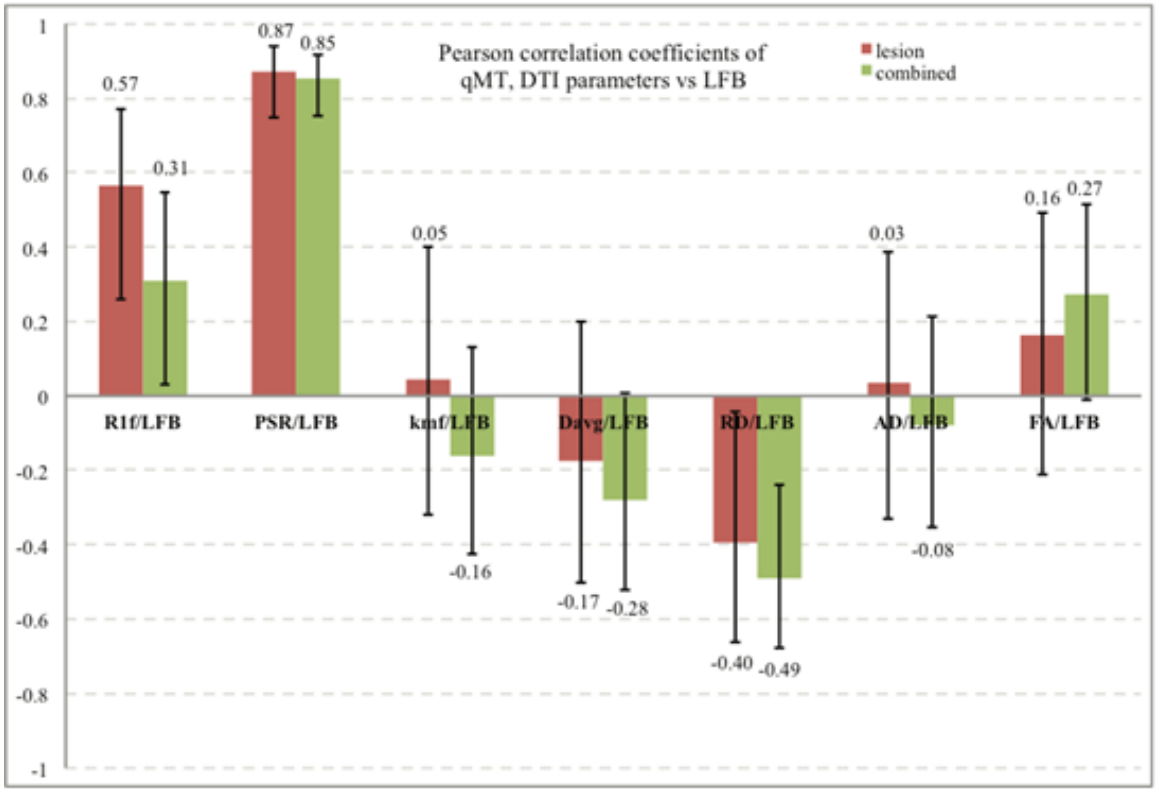

Figure 3-6. Pearson correlations of DTI (RD, AD, FA, and D_{avg}) and qMT (PSR, kmf, and R1f) parameters vs LFB histology. PSR shows a strong positive and RD shows a strong negative correlation with myelin content measured by LFB histology. Much weaker correlations are found for other parameters. lesioned rats tend to show stronger correlations then for combined lesion and non-lesion rats samples. Only correlations PSR/LFB, Davg/LFB, RD/LFB were significant ($p<0.05$) for the combined and lesion set. The error bars denote the 95% confidence intervals for correlation coefficients. p-values for the correlations are given in table below.

Table 3-2. *p*-values for correlations of qMRI with LFB histology

vs LFB	R1f/LFB	PSR/LFB	kmf/LFB	D_{avg}/LFB	RD/LFB	AD/LFB	FA/LFB
Combined	0.031728	1.22E-14	0.27691	0.055159	0.000413	0.599932	0.060281
Lesioned	0.001087	3.11E-10	0.807615	0.361128	0.030472	0.862243	0.394368

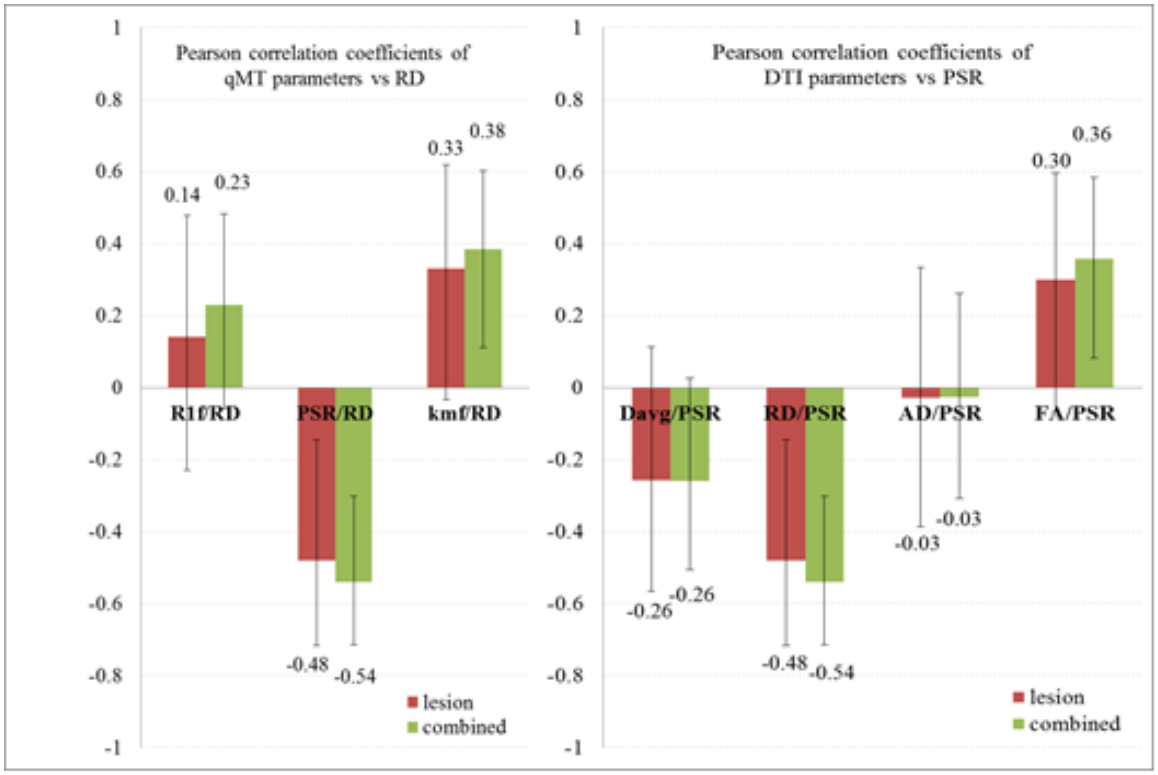

Figure 3-7. Pearson correlations between (A) DTI (RD, AD, FA, and Davg) parameters vs PSR and (B) qMT (PSR, kmf, and R1f) parameters vs RD. (RD and PSR parameters showed the strongest correlations with LFB histology.) Only correlations R1f/RD, kmf/RD, PSR/RD for the combined set and PSR/RD for the lesion set were significant ($p<0.05$). The error bars denote the 95% confidence intervals for correlation coefficients. p-values for the correlations are given in table below

Table 3-3. *p*-values for correlations of DTI parameters with PSR and qMT parameters with RD

vs PSR	Davg/PSR	RD/PSR	AD/PSR	FA/PSR	R1f/RD	PSR/RD	kmf/RD
Combined	0.073951	7.41E-05	0.863742	0.012642	0.117515	7.41E-05	0.007191
Lesioned	0.169435	0.007164	0.877948	0.107537	0.455222	0.007164	0.074348

Discussion

In this study, we have used an on-resonance qMT method due to our familiarity with this method and its advantages vs off-resonance methods. (For example, it has little sensitivity to field inhomogeneities and avoids the need to co-register T1, B0, and B1 maps acquired from different scans.) However, our key results concerning the sensitivity of PSR to myelination should be independent of the particular acquisition method, though we have not demonstrated this.

We comprehensively correlate quantitative metrics from qMT and DTI with histological myelin measure, and also explore their inter-correlations in an LPS induced animal model of type III MS lesions. To our knowledge, this is the first study correlating quantitative DTI and qMT metrics with histology and with each other. In LPS injected rats with lesions, PSR showed the strongest correlation with myelin content (Fig.5, 6) and showed strong correlations only with RD among other DTI metrics (Fig. 7). This indicates the specificity of PSR towards demyelination. qMT quantifies water protons closely associated with macromolecules like that found in myelin and cell structures. Pool size ratio (PSR) is the ratio of exchanging macromolecular protons to the free water protons. Thus, PSR may relate more directly to myelin content. Though it was not part of this study Multi exponential T2 (MeT2) is an additional quantitative putative measure of myelin. There have been several studies correlating MeT2, and specifically the amplitude of T2 ~10ms decay component, with myelin histology (Laule et al., 2006). However recent work (Dula et al., 2010b) suggests that exchange effects may bias MeT2 assessments of myelin, but that these effects do not bias PSR.

qMT measured PSR and DTI measured RD are both indirect markers of myelin content. DTI is a quantitative measure of water diffusion anisotropy within tissue microstructure. Axial and radial diffusivity reflect diffusivity of water along and perpendicular to axons within the tissue. However, this interpretation is complicated by alignment and density of fibers, along with factors like myelin sheath thickness and intactness of axons. Various studies on demyelinating and dysmyelinating animal models have shown sensitivity of radial diffusivity towards myelin (Klawiter et al., 2011; Ou et al., 2009; Song et al., 2002; Song et al., 2005), where lack of myelin is indicated by increase in radial diffusivity. Song et al. found radial diffusivity to be more specific to demyelination in presence of axonal damage, where the axonal damage is itself correlated to axonal diffusivity. However, studies have also shown in presence of inflammation (edema), RD underestimates demyelination (Budde et al., 2008). Also, AD is affected by variations in axonal diameter and the voxel scale coherence of axon tracts (Beaulieu, 2002).

The longitudinal rate R1 has also been correlated with myelin, though edema (without demyelination) also affects R1. As an added complication, R1 actually includes both relaxation and MT effects when measured using multi-angle gradient echo (Ou and Gochberg, 2008) or conventional inversion recovery (Edzes and Samulski, 1977; Gochberg and Gore, 2003, 2007a; Prantner et al., 2008). (Though these effects are often overlooked, longitudinal recovery is bi-exponential due to MT effects. While the macromolecular and water protons are in fast exchange, the signal is bi-exponential since only water protons are measured.) However, the current work avoids these issues by isolating the longitudinal relaxation rate of the free water ($R1_f$). We found that the correlation of $R1_f$ with myelin histology was much weaker than PSR.

There are various study design and method factors influencing the correlation between MR metrics and histology, and these may lead to increase in scatter on correlation plots. Hence, the correlation of the qMT parameters to histology vs. the correlation of DTI parameters vs. histology may be affected by our particular acquisition choices. However, Monte Carlo simulations (not shown) indicate that, at the measured image SNR (~100 for qMT and ~35 for DTI) and assuming the noise in each pixel is independent, the expected variation in the fitted parameters is roughly an order of magnitude less than the measured scatter. Hence, physiologic variations most likely dominate, making the details of the acquisition choices non-determinative. An additional issue and possible source of error is correlation with histology. Accurate correlation between MR metrics and quantitative histology myelin content is influenced by numerous factors including the difference in histology and MR slice thickness, orientation of histological slice plane relative to the neuronal fibres, and artifacts in histological images, all of which may result in errors in myelin quantification. The resulting errors are difficult to quantify. However, all the above factors influence the correlations between MR metrics and histology equally and the comparative results are therefore meaningful.

Conclusion

This study demonstrates sensitivity of PSR and RD to the degree of demyelination in LPS mediated white matter lesions in the CC, with PSR showing a greater degree of sensitivity compared to RD. In conclusion this study demonstrates that PSR and RD are sensitive markers of myelin content and integrity (myelin content PSR vs myelin integrity RD). PSR reflects myelin content more accurately, thus presents an attractive alternative for non-invasive detection and quantification of myelin abnormalities.

CHAPTER IV

CONCLUSIONS AND FUTURE DIRECTIONS

Quantitative MRI methods have the potential to increase the sensitivity and specificity to underlying CNS pathologies, addressing a major limitation of conventional MRI. qMT and DTI are two of the leading quantitative methods used for white matter characterization and myelin assessments in research settings. In recent years significant efforts were directed in development and optimization of qMT and DTI methods. This has decreased the imaging time and currently whole brain qMT and DTI scans can be obtained each in less than 10 minutes, reaching a clinically viable time period. However these methods are based on mathematical models and are computationally demanding. These models are relatively simple and only approximate certain key features of the tissue. In addition, these methods have implicit assumptions. Thus the qMT and DTI parameters need extensive validation for a clear interpretation in a wide range of tissue pathologies. Furthermore, both PSR and RD, the qMT and DTI parameters, respectively, are sensitive to myelin, but have different biophysical basis. Few studies compare multiple quantitative MRI methods and validate them with histology. In the studies presented in this dissertation we have addressed this need by comparing the relative sensitivities of qMT and DTI techniques to myelin, and validated them using quantitative myelin histology in an animal model of MS.

We performed comparative *in vivo* validation of the specific sensitivities of qMT and DTI techniques to myelin in the rat brains through quantitative histology (Chapter 2). Of the two putative MRI markers of myelin investigated, PSR and RD, PSR showed the stronger correlations with myelin content in the brain tissue (GM and WM grouped together). Additionally, PSR also showed the greatest contrast between GM and WM among all the qMT and DTI parameters, suggesting utility of PSR in image segmentation. A major limitation of our study was the lack of significant correlations within WM or within GM with histological myelin content, when evaluated separately. To address this limitation, the processing pipeline was carefully evaluated from beginning to end, and the sources of errors were identified that contributed to the loss of precision for the observed correlations. These issues are discussed in Chapter 2 and were addressed in the protocol designed for *ex vivo* evaluation (Chapter 3).

Subsequently, we performed *ex vivo* validation of the specific sensitivities of qMT and DTI techniques to myelin in perfusion-fixed rat brains through quantitative histology. Implementation of robust processing and registration protocol designed to address issues identified in Chapter 2 led to significant reduction in contributions from experimental uncertainties. Furthermore, optimized high resolution 3D qMT and DTI protocols were implemented. We found significant correlations within the CC of WM, which were dominated by demyelination in CC. Supporting the conclusion of *in vivo* study, PSR showed the strongest correlations amongst all qMT and DTI parameters with myelin content in the *ex vivo* study as well. RD showed the next strongest correlation indicating its sensitivity to myelin. The strong and significant linear correlation of PSR with histological myelin content demonstrates the ability of PSR to quantify myelin content within a single lesioned WM structure. In addition, we characterized the first animal model of type III MS lesions using quantitative MRI methods and investigated the non-inflammatory demyelinating phase of this MS animal model (Chapter 3). Furthermore, the gray and white

matter compositions of rat brains are similar to those of humans (Quarles R, 2006). Thus the validation and comparison of sensitivity is still meaningful for MS pathology, although our study involved a rodent model. Now that the methodology has been developed to perform quantitative comparisons, the next obvious step is to perform longitudinal and cross-sectional studies for complete characterization of the LPS induced animal model of type III MS lesions, and determine the qMRI correlates of the disease pathology.

The basic methodology we developed for systematic quantitative *in vivo* and *ex vivo* comparisons of DTI and qMT methods, and their histological validation, could in general be employed for other MRI techniques and histopathological validation. One course of action could be to include other qMRI methods in the study, such as the Multiexponential T_2 (MeT2) technique. As briefly alluded in the earlier chapters, MeT2 technique is based on the multi-compartmental T_2 relaxation tissue model and particularly apt to distinguish demyelination from inflammation (Does and Snyder, 1996; Odrobina et al., 2005). The quantitative parameters from qMT, DTI, and MeT2 techniques are complementary and may lead to a more complete characterization of WM pathology. In addition, the histological validation would reveal their relative sensitivities to a given pathological condition such as demyelination.

MS is known to have both inflammatory and neurodegenerative components. Neurodegeneration is also attributed for irreversible disability. While significant progress has been made on understanding and treating the inflammatory component, a thorough understanding of neurodegenerative aspect is lacking. Similarly, the Initial stages (day 3 post LPS injection) of lesions in the animal model used in our studies are primarily inflammatory, and the later stages (day 28 post LPS injection) are demyelinating. Thus inclusion of additional

histological stains to quantify extent of pathologies such as inflammation, axonal damage and gliosis could be included to assess the pathological specificity of qMRI parameters.

In conclusion, among the all the qMT and DTI parameters PSR is better suited to quantify degrees of demyelination in an animal model of type III MS lesions. PSR has greater sensitivity to and linear relationship with histological myelin content. Future studies could reveal if this result holds true at all time points of the LPS model and for other animal models of MS.

Appendix

Effect of thermal noise on the qMRI parameters

In this appendix, the aim is:

(1) To estimate the effect of thermal noise on the precision (standard deviation) and accuracy (mean bias) of the tissue model based qMT and DTI parameter estimation.

(2) To compare them with the physiological variation seen in the parameters in the CC of LPS injected rats.

Monte Carlo simulations were performed to estimate the contribution of the thermal noise in the estimation of qMT and DTI parameters and to predict bias and precision at the SNR levels of the image. Monte Carlo simulations were also performed at different noise levels to measure the influence of the SNR on the uncertainties of fitted the parameters for the five point optimal scheme.

Parameter sets from the ROIs with the lowest and the highest PSR values in a single representative animal were selected for these simulations. Extreme values in PSR were selected as PSR correlates the strongest with myelin histology and is the parameter of interest in this study (see Figure 3-1). The

average parameter values for 12 ROIs in the CC and for the whole CC ROI are shown in Table 1. ROI #2 and #7 were used in the analysis below.

Table 1: Average parameter values for CC and 12 1mm ROI for rat #8. Parameter set with maximum (blue) and minimum (red) PSR are selected for simulations.

ROIs	R1f	PSR	kmf	Sf	Minf
Average CC	0.9397	0.1918	18.6224	0.9391	39.7580
1	0.9940	0.2114	22.2508	0.9827	33.4841
2	1.0284	0.2339	20.9066	0.9744	31.3660
3	0.9824	0.2204	19.4976	0.9488	34.5346
4	0.9411	0.2180	17.7615	0.9451	37.3169
5	0.9506	0.2027	17.0976	0.9292	39.8209
6	0.9536	0.1859	19.4065	0.9373	41.5632
7	0.8592	0.1339	20.7843	0.9253	45.0448
8	0.8392	0.1384	15.4333	0.9283	47.0295
9	0.8753	0.1414	17.1775	0.9096	47.6028
10	0.9418	0.2045	17.1046	0.9241	41.6148
11	0.9731	0.2141	18.2459	0.9338	37.8067
12	0.9507	0.2086	19.0333	0.9292	37.6864

Table 2(a): SNR in GM and WM in qMT dataset

Region	Image 1	Image 2	Image 3	Image 4	Image 5
GM	169.663	175.628	130.343	131.095	154.629
WM (CC)	100.719	89.8914	68.6689	43.1215	103.182

Table 2(b): 'ti' and 'td' delay times for five point qMT acquisition scheme

data point	1	2	3	4	5
ti (s)	0.006	0.032	0.035	0.225	0.77
td (s)	3.502	4.603	1.507	3.273	0.11

qMT acquisition was made using the SIR-FSE sequence using the 5pt scheme (as described in Chapter 3). The set of 5 ti (inversion time) - td (delay time) (see Table 2(b).) values and the fitted parameter set values were used to generate the signal and Gaussian white noise was added to the signal points according to the SNR values. Simulated signal was than fitted to a two-pool MT tissue model in same manner as was used to get the pixel wise parameter maps for qMT, in the least square sense using Levenberg-Marquardt algorithm, implemented with the lsqcurvefit function in MATLAB.

For each of the five images the SNR was calculated using the selected whole CC WM and above-CC GM ROI's. For the noise level estimate, a region in the image away from the tissue and any imaging artifacts was selected assuming the noise in the image is spatially independent. The noise-free signal was simulated from the parameter set chosen from ROI. A sample illustration of SNR values from rat 8 are presented in Table 2(a).

The SNR of qMT data for rat 8 has the SNR range of 43-103 in WM and 130-175 in GM, with the first image having the SNR of 100 in the CC. For the ROI analysis, the CC was further divided in 1 mm ROIs from the sagittal suture (midline in the axial image). Each rat had about 10-13 ROI's in the CC depending on the structural details of CC and the size of WM ROI selected in the CC. As the histology slice is the

gold standard for tissue condition, including the GM and WM distinction, a MRI matched histology slice stained with LFB for myelin is shown in the Figure 1 with ROIs drawn in the CC.

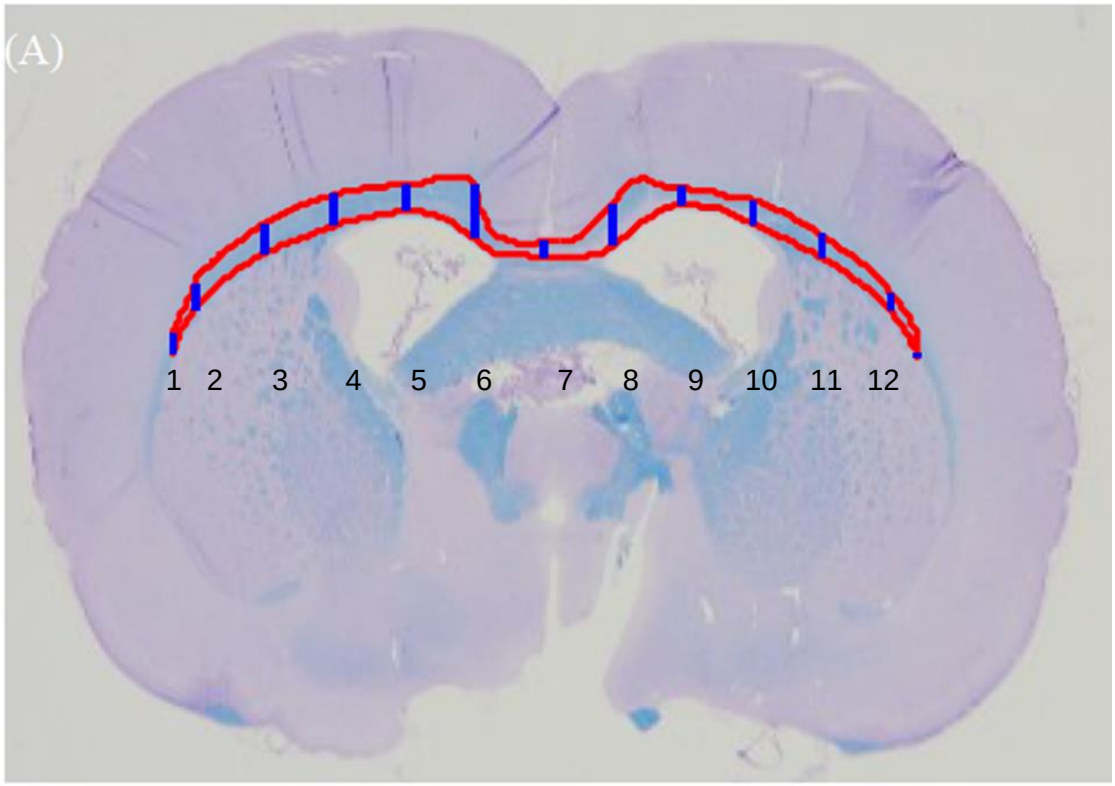

Figure 1: **ROIs shown on MRI matched histology slice image LFB stained for myelin, from rat #8**. CC ROI is shown in Red, with blue vertical line separating the 1mm ROIs starting from the midline. The ROI's are numbered left to right.

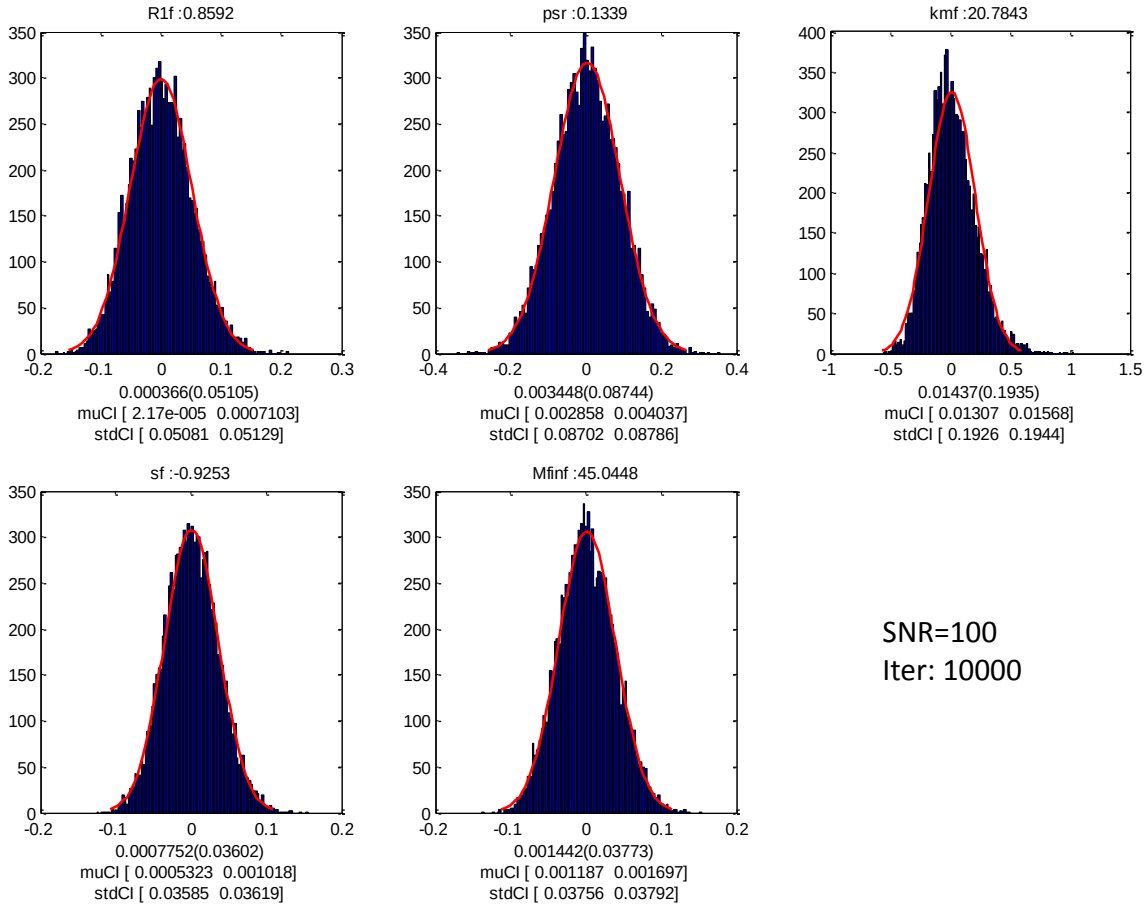

Figure 2: Thermal noise bias and precision estimate for low PSR qMT set by Monte-Carlo Simulations. Fitted parameter distributions from Monte-Carlo simulations using the low PSR qMT parameter set with the SNR of 100 and 10,000 iterations. The red curve is a normal distribution fit to the distribution. The title of each parameter distribution figure indicates the true parameter value. Y-axis indicates the number of occurrences and X-axis denotes the normalized difference from true value, normalized with true parameter value. The values at the bottom of each figure denote the mean (std dev.) or normalized fitted parameter and their 95% confidence intervals.

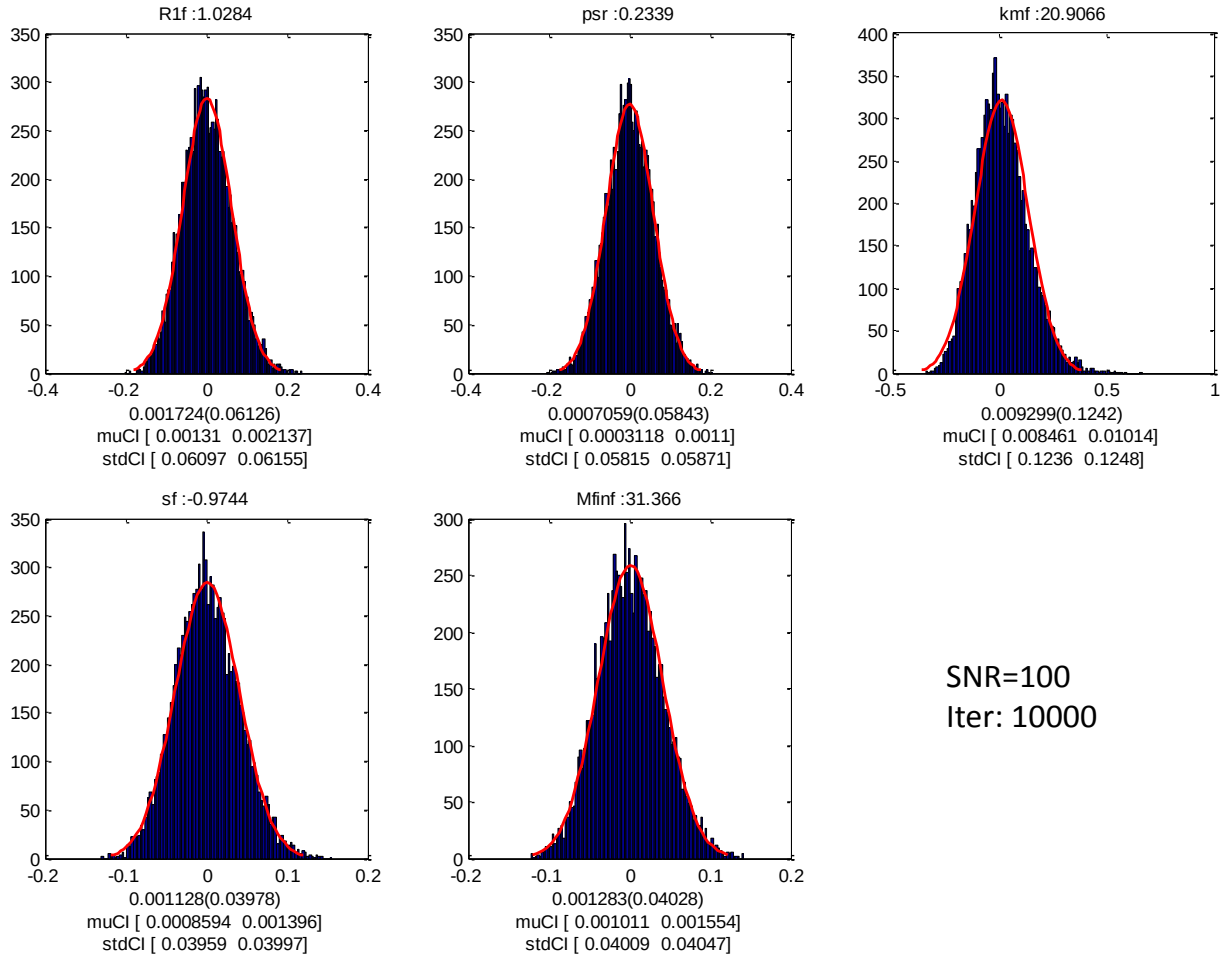

Figure 3: Thermal noise bias and precision estimate for high PSR qMT set by Monte-Carlo Simulations. Fitted parameter distributions from Monte-Carlo simulations using the high PSR qMT parameter set with the SNR of 100 and 10,000 iterations. The red curve is a normal distribution fit to the distribution. The title of each parameter distribution figure indicates the true parameter value. Y-axis indicates the number of occurrences and X-axis denotes the normalized difference from true value, normalized with true parameter value. The values at the bottom of each figure denote the mean (std dev.) or normalized fitted parameter and their 95% confidence intervals.

Two set of parameter values were used for simulations over the range of iterations to determine the minimum number of iterations required for the distribution to stabilize. Table 3, summarizes the results for number of iterations (N) 10, 100, 1000, and 10000. The bias in parameter estimation was evaluated using the relative bias (RB) defined as $\frac{\mu-\mu_0}{\mu_0}$, where μ is the mean of fitted parameter distribution, mu0 is the true value of the parameter. To evaluate the precision, relative standard deviation (RSD) was calculated defined by equation RSD = std($\frac{\pi-\mu_0}{\mu_0}$) , where π is the fitted parameter value and std is standard deviation. The definition of RB and RSD facilitate comparison of bias and precision across the parameters. We found the mean (RB) and the standard deviation (RSD) of the simulated parameter set did not vary beyond one percent after about 100 iterations (see RB, RSD in Table 3). Thus the number of iterations performed is sufficient to obtain reliable estimate.

Simulations were also performed over the range of SNR to determine the influence of SNR on the fitted parameter distributions the results obtained were consistent with Li et al. 2010, Dortch et al. 2011. SNR of 100 was found to be adequate to produce robust fitting results. The qMT parameter sets used for simulations are listed below:

Low PSR parameter set which corresponds to ROI# 7 in Table 1:

R_{1f}= 0.8592 Hz, kmf= 20.7843 Hz, PSR = 0.1339 and S_f = -0.9253, R_{1m}=0.5, and S_m = 0.83

High PSR parameter set which corresponds to ROI# 2 in Table 1:

R_{1f}= 1.0284 Hz, kmf= 20.9066 Hz, PSR = 0.2339 and S_f = -0.9744, R_{1m}=0.5, and S_m = 0.83

Table 3: Determination of sufficient number of iterations for low and high PSR set Effect on relative bias (RB) and relative standard deviation (RSD) with increasing number of iterations. The values stabilized within 1% after 100 iterations. (a) Low PSR set, and (b) High PSR set.

(a) Low PSR set

N=10		N=100		N=1000		N=10000	
RB	RSD	RB	RSD	RB	RSD	RB	RSD
0.0142	0.067	-0.002	0.0537	-0.0013	0.0514	0.0004	0.051
0.0429	0.0822	0.0056	0.0849	0.0057	0.0856	0.0034	0.0874
-0.0279	0.2867	0.0069	0.1776	0.0181	0.1944	0.0144	0.1935
0.0047	0.0452	-0.0003	0.0357	-0.0005	0.0361	0.0008	0.036
-0.0047	0.0536	0.0039	0.0389	0.0034	0.0375	0.0014	0.0377

(b) High PSR set

N=10		100		1000		10000	
RB	RSD	RB	RSD	RB	RSD	RB	RSD
0.0097	0.0463	0.0044	0.063	0.0006	0.0641	0.0017	0.0613
0.0204	0.0641	-0.0051	0.0599	-0.0012	0.0575	0.0007	0.0584
0.0417	0.1383	0.0091	0.1288	0.0116	0.128	0.0093	0.1242
0.0151	0.0419	-0.0003	0.0421	0.0005	0.0405	0.0011	0.0398
-0.0086	0.0393	0.0007	0.0425	0.002	0.0417	0.0013	0.0403

The relative bias and relative standard deviation of the fit parameter values for the low PSR parameter set was found to be

R_{1f}= 0. 04%(0.51%), kmf= 1.44%(19.35%), PSR = 0.34%(8.74%), S_f = 0.08(3.6%), and Minf=0.14%(3.77%).

And for the high PSR parameter set to be

R_{1f}= 0.17%(6.13%), kmf= 0.93%(12.42%), PSR = 0.07%(5.84%), S_f= 0.11%(3.98%),and Minf=0.13%(4.03%).

The relative bias in each of the fitted parameters was found to be less than 0.5% except for kmf for which it was close to 1%. PSR, R1f, Sf and Minf are robustly determined. The standard deviation in kmf was found to be 2-5 times more than other parameters with this acquisition scheme. Consistent with studies Li, dortch et al. the uncertainty in kmf was found to be much larger than other parameters, especially in the regions where SNR is low.

Detailed statistics for each of the ROIs for the PSR parameter are given below in Table 4, where Npix is number of pixels in the ROI, Avg is the average parameter value, Max and Min are respectively, the maximum and the minimum parameter value in ROI, std and RSD are the standard deviation and the relative standard deviation (std/Avg) of the parameter values within the ROI. Tshows the relative size of each ROI selected I CC (Npix) and the extent of PSR variation observed within each ROI as summarized by max, min, and std. The variations observed in PSR within each ROI has contributions from both

thermal noise and physiological variations. A qualitative estimate of the contribution form physiological variation can be estimated from the myelin variation in the LFB image shown in Figure 1. For example ROI # 8 both myelinated and demyelinated regions within ROI and correspondingly has highest RSD in Table 4.

Table 4: Details of within the ROI statistics for the PSR parameter in the CC and 12 1mm ROI for the rat #8. ROIs are numbered left to right starting from 1 through 12. Npix denotes the number of pixels in each ROI. Avg, Max, Min, std and RSD are the average, maximum, minimum, standard deviation and the relative standard deviation of the PSR values in the respective ROI.

ROI	CC	1	2	3	4	5	6	7	8	9	10	11	12
Npix	144	12	12	14	10	13	12	12	15	11	15	14	4
Avg	0.192	0.211	0.234	0.22	0.218	0.203	0.186	0.134	0.138	0.141	0.205	0.214	0.209
Max	0.26	0.241	0.26	0.254	0.257	0.232	0.237	0.165	0.198	0.166	0.228	0.228	0.216
Min	0.041	0.182	0.202	0.191	0.202	0.169	0.123	0.104	0.041	0.1	0.174	0.197	0.197
std	0.042	0.018	0.018	0.017	0.017	0.02	0.034	0.016	0.049	0.026	0.016	0.01	0.008
RSD	0.219	0.085	0.077	0.077	0.078	0.099	0.183	0.119	0.355	0.184	0.078	0.047	0.038

Table 5: Inter and intra ROI variation in parameters is much larger than the thermal noise contributions to PSR variability. Comparison of intra and inter ROI variation in PSR values with variations in values due to thermal noise. The inter and intra ROI variations include contributions from both the physiological variation and thermal noise variation.

Intra ROI RSD		Whole CC	Thermal Noise RSD		Inter ROI	
Min	Max	RSD	Low PSR set	High PSR set	RSD	variation
3.8%	35.5%	22 %	8.74%	5.84%	17.4	75%

Table 6: SNR in GM and WM in DTI dataset

Region	Image 1	Image 2	Image 3	Image 4	Image 5	Image 6	Image 7
GM	53.8411	54.1604	46.1974	46.6569	46.5458	53.065	48.148
WM (CC)	34.2429	36.9878	31.9833	29.3731	34.4653	34.6339	34.1369

The simulated distributions only include the effect of thermal noise on the parameters, whereas the parameters determined on pixel-by-pixel basis include the contributions from both the thermal noise and the physiological variation. The table below summarizes the variation in PSR seen within ROIs, between ROIs and due to thermal noise.

The physiological variation seen in the PSR was an order of magnitude greater than the thermal noise generated variations in the fitted parameters on ROI basis. For example variation in PSR across ROIs in rat 8 was (0.2339 - 0.1339) about 75% change relative to lower PSR value. The parameters were calculated on a pixel basis and the variation in parameters is even greater on a pixel basis across the ROIs, thus physiological variations are dominant factor for inter ROI variation of parameters.

For estimation if thermal noise in DTI parameters a similar Monte-Carlo simulations were performed. The DTI data set consists of 13 images acquired. With 6 pairs of diffusion weighted images in independent directions with each pair of images having diffusion weighting in opposing directions and one image with no diffusion gradients on. The average SNR of the non-diffusion weighted image in the GM above CC was 53 and in the CC, SNR was 34. The pair of images with the diffusion gradients in opposing direction is averaged to get the final 7 images used for DTI analysis. Table 6 summarizes the SNR in the images used for analysis.

Assuming the noise contribution is spatially independent the SNR in DTI dataset in the CC of rat #8 is in the range of 16 to 50. DTI parameter maps were calculated by DTI analysis (as described in Chapter 3).

Registration was performed using maximization of mutual information algorithm implemented in Matlab on non-diffusion weighted image with qMT data and affine transformation was determined to bring DTI data to the qMT space. The transformation was later applied to DTI parameter set to allow correlation of DTI and qMT parameters on a pixel-by-pixel basis. The ROI analysis was performed on the DTI parameter maps using same ROI as used for qMT data. Each rat had about 10-13 ROI's in the CC.

Monte Carlo simulations were performed using the diffusion dataset from randomly selected pixels in CC using a range of SNRs to estimate the contribution of the thermal noise to DTI parameter estimation and to predict the bias and precision at the SNR levels of the image. The number of iterations used were 100 000, the noise was added to raw data based on the mean SNR level and the noisy data was analyzed in the same manner as to obtain the DTI parameter maps in the chapter 3. The data used for the simulation have noise contribution.

DTI Simulation, Rat 8 Slice 68, Nsim = 100 000: SNR image with the pixel selected for simulation data is indicated by a red open circle in the CC. SNR pix = 43.25

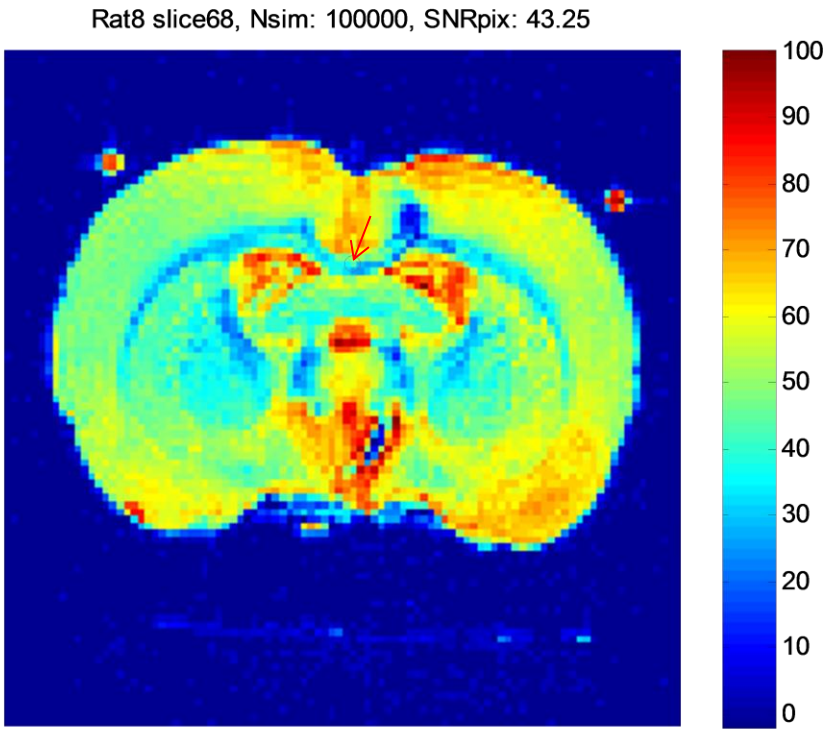

Figure 4: Representative randomly selected pixels in CC of DTI image selected for Monte-Carlo simulations and corresponding pixel SNR. Red arrow indicates the selected pixel.

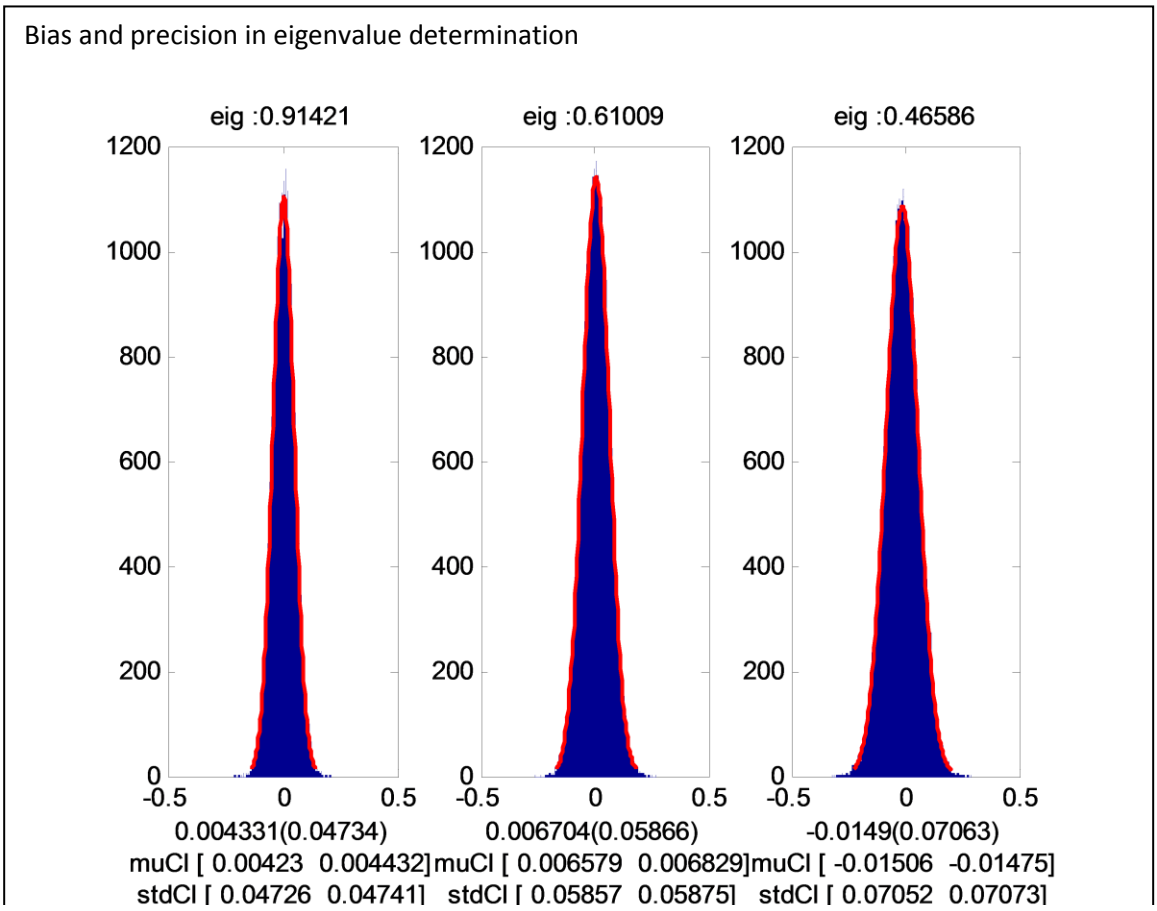

Figure 5: Representative bias and precision determination in eigenvalue determination.

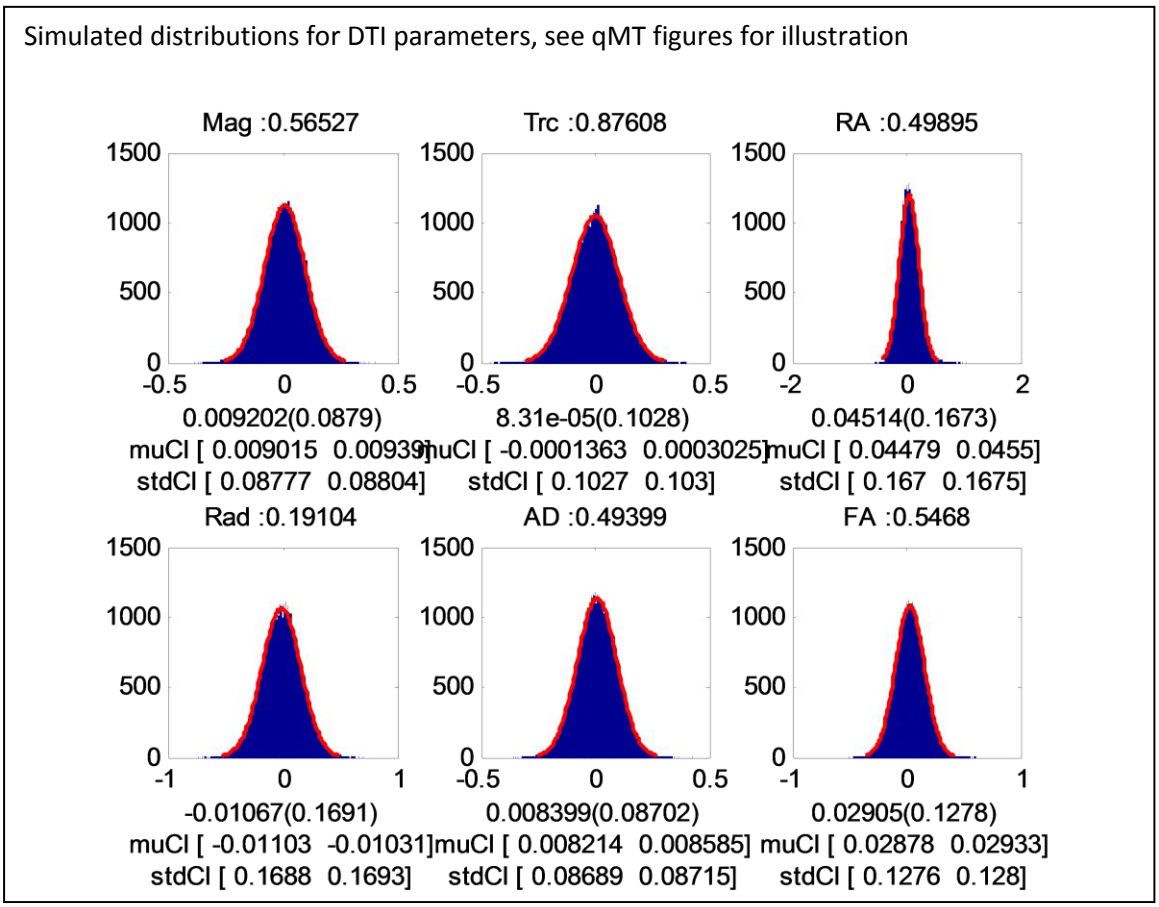

Figure 6: Representative bias and precision determination in estimated DTI parameters.

DTI Simulation, Rat 8 Slice 68, Nsim = 100 000: SNR image with the pixel selected for simulation data is indicated by a red open circle in the CC. SNR pix = 35.1

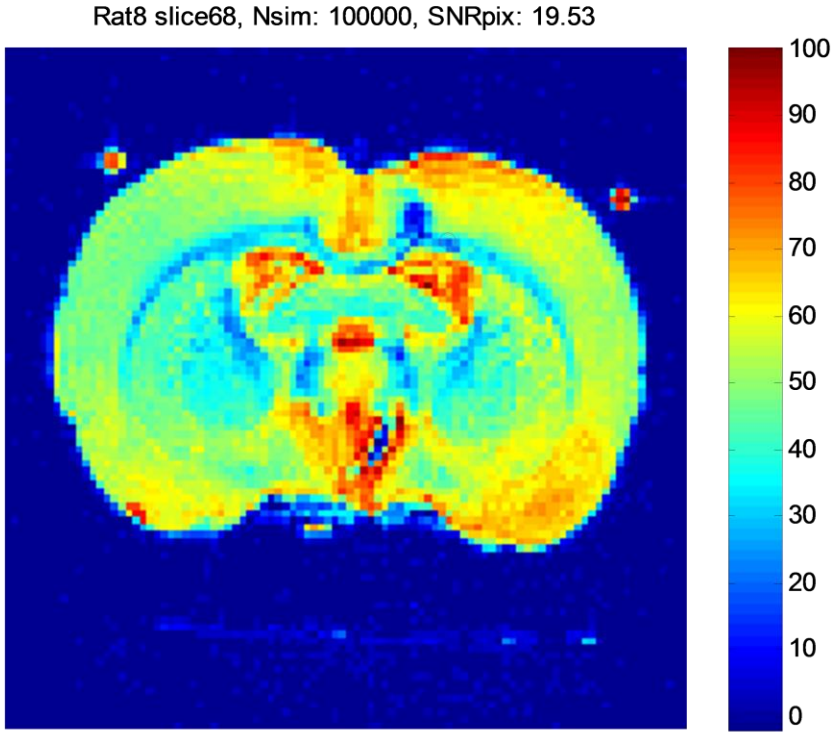

Simulated distributions for DTI parameters, see qMT figures for illustration

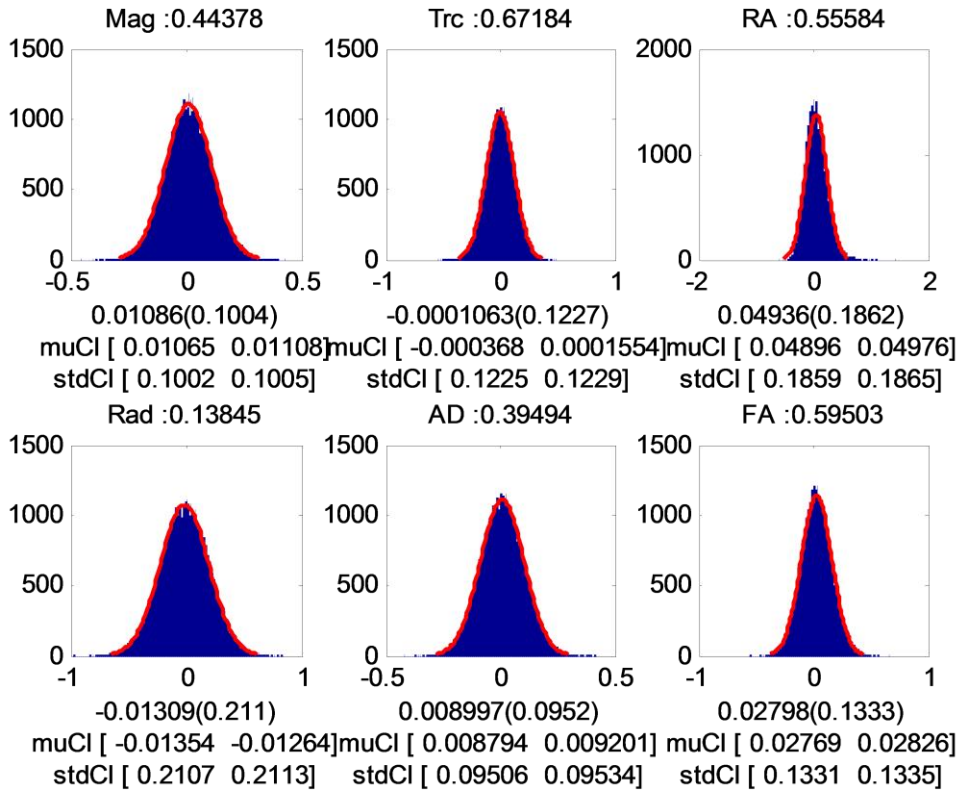

Bias and precision in eigenvalue determination

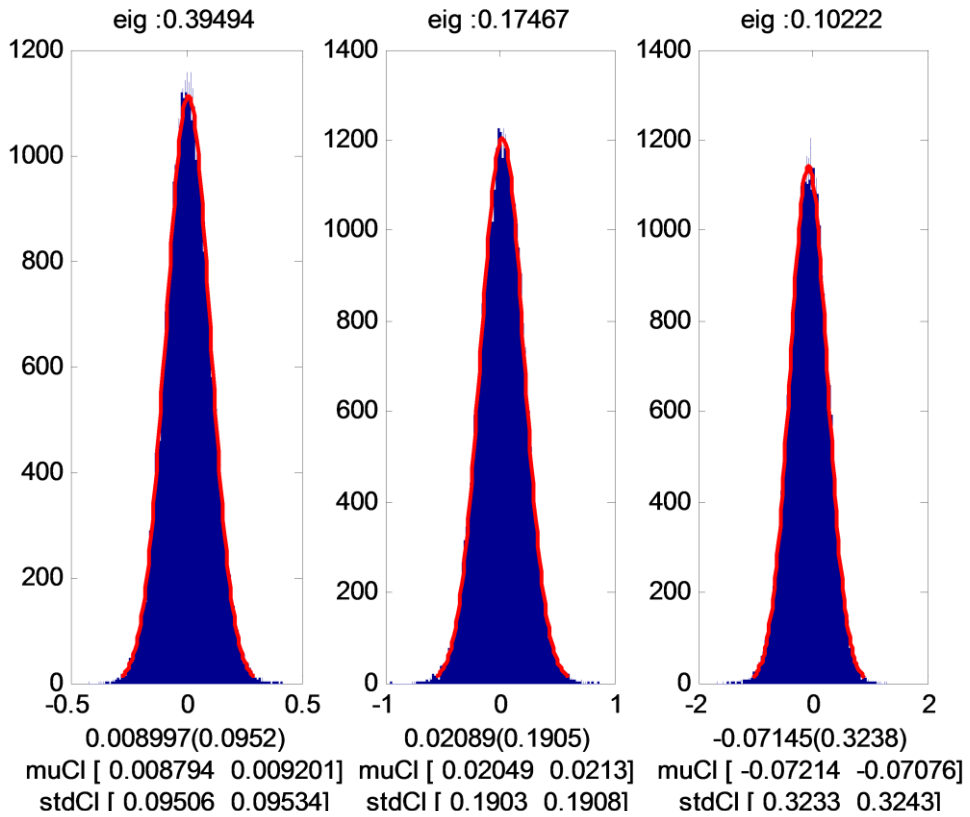

Table 7: Average DTI parameters values for CC and twelve 1mm ROI for rat #8.

ROI	Davg	Trace	RA	RD	AD	FA
CC	0.5701	0.8874	0.533	0.2175	0.4676	0.5302
1	0.5056	0.8082	0.4086	0.2019	0.4044	0.4541
2	0.5124	0.7081	0.7734	0.1166	0.475	0.7348
3	0.5651	0.8244	0.6464	0.1576	0.5092	0.649
4	0.4808	0.6799	0.7264	0.119	0.4419	0.703
5	0.394	0.6007	0.6344	0.15	0.3239	0.5991
6	0.4535	0.6676	0.7499	0.1521	0.3886	0.6708
7	0.8769	1.4032	0.5582	0.3982	0.6865	0.5251
8	0.623	1.0184	0.4492	0.3144	0.4734	0.4346
9	0.6001	1.0202	0.197	0.2975	0.4252	0.2361
10	0.6409	1.026	0.3992	0.2541	0.5178	0.4362
11	0.6237	0.989	0.4289	0.2407	0.5076	0.4642
12	0.5972	0.9708	0.3657	0.2462	0.4783	0.4156

The average parameter values for 12 ROI in CC and for the whole CC ROI for RD are shown in Table 7.

Table 8: Comparison of thermal noise variation and the physiological variation including thermal noise within and between ROIs.

Intra ROI RSD		Whole CC	Thermal Noise RSD			Inter ROI	
Min	Max	RSD	SNR= 42	SNR=31.2	SNR=19.5	RSD	Range
21.79%	86.45%	59.75 %	6.52%	16.91%	21.1%	37.9%	241%

The physiological variation seen in the radial diffusivity (RD) was an order of magnitude greater than the thermal noise generated variations in the fitted parameters on ROI basis. For example variation in RD across ROIs in rat #8 was (0.3982 - 0.1166) about 241% change relative to lower RD value. The parameters were calculated on a pixel basis and the variation in parameters is even greater on a pixel basis across the ROIs, thus physiological variations are dominant factor for inter ROI variation of parameters.

REFERENCES

Assaf, Y., Pasternak, O., 2008. Diffusion tensor imaging (DTI)-based white matter mapping in brain research: a review. J Mol Neurosci 34, 51-61.

Barkhof, F., Filippi, M., Miller, D.H., Scheltens, P., Campi, A., Polman, C.H., Comi, G., Ader, H.J., Losseff, N., Valk, J., 1997. Comparison of MRI criteria at first presentation to predict conversion to clinically definite multiple sclerosis. Brain 120 (Pt 11), 2059-2069.

Basser, P.J., Mattiello, J., LeBihan, D., 1994a. Estimation of the effective self-diffusion tensor from the NMR spin echo. J Magn Reson B 103, 247-254.

Basser, P.J., Mattiello, J., LeBihan, D., 1994b. MR diffusion tensor spectroscopy and imaging. Biophys J 66, 259-267.

Basser, P.J., Pierpaoli, C., 1996. Microstructural and physiological features of tissues elucidated by quantitative-diffusion-tensor MRI. Journal of Magnetic Resonance Series B 111, 209-219.

Berry, I., Barker, G.J., Barkhof, F., Campi, A., Dousset, V., Franconi, J.M., Gass, A., Schreiber, W., Miller, D.H., Tofts, P.S., 1999. A multicenter measurement of magnetization transfer ratio in normal white matter. J Magn Reson Imaging 9, 441-446.

Confavreux, C., Vukusic, S., Moreau, T., Adeleine, P., 2000. Relapses and progression of disability in multiple sclerosis. N Engl J Med 343, 1430-1438.

Cook, L.L., Foster, P.J., Mitchell, J.R., Karlik, S.J., 2004. In vivo 4.0-T magnetic resonance investigation of spinal cord inflammation, demyelination, and axonal damage in chronic-progressive experimental allergic encephalomyelitis. J Magn Reson Imaging 20, 563-571.

Does, M.D., Beaulieu, C., Allen, P.S., Snyder, R.E., 1998. Multi-component T1 relaxation and magnetisation transfer in peripheral nerve. Magn Reson Imaging 16, 1033-1041.

Dousset, V., Grossman, R.I., Ramer, K.N., Schnall, M.D., Young, L.H., Gonzalez-Scarano, F., Lavi, E., Cohen, J.A., 1992. Experimental allergic encephalomyelitis and multiple sclerosis: lesion characterization with magnetization transfer imaging. Radiology 182, 483-491.

Filippi, M., 2011. Multiple sclerosis in 2010: Advances in monitoring and treatment of multiple sclerosis. Nat Rev Neurol 7, 74-75.

Gareau, P.J., Rutt, B.K., Karlik, S.J., Mitchell, J.R., 2000. Magnetization transfer and multicomponent T2 relaxation measurements with histopathologic correlation in an experimental model of MS. J Magn Reson Imaging 11, 586-595.

Gass, A., Barker, G.J., Kidd, D., Thorpe, J.W., MacManus, D., Brennan, A., Tofts, P.S., Thompson, A.J., McDonald, W.I., Miller, D.H., 1994. Correlation of magnetization transfer ratio with clinical disability in multiple sclerosis. Ann Neurol 36, 62-67.

Ge, Y., Grossman, R.I., Udupa, J.K., Babb, J.S., Kolson, D.L., McGowan, J.C., 2001. Magnetization transfer ratio histogram analysis of gray matter in relapsing-remitting multiple sclerosis. AJNR Am J Neuroradiol 22, 470-475.

Gochberg, D.F., Gore, J.C., 2003. Quantitative imaging of magnetization transfer using an inversion recovery sequence. Magnetic Resonance in Medicine 49, 501-505.

Gochberg, D.F., Gore, J.C., 2007. Quantitative magnetization transfer imaging via selective inversion recovery with short repetition times. Magnetic Resonance in Medicine 57, 437-441.

Hansen, J.R., 1971. Pulsed NMR study of water mobility in muscle and brain tissue. Biochim Biophys Acta 230, 482-486.

Henkelman, R.M., Huang, X.M., Xiang, Q.S., Stanisz, G.J., Swanson, S.D., Bronskill, M.J., 1993. Quantitative Interpretation of Magnetization-Transfer. Magnetic Resonance in Medicine 29, 759-766.

Henkelman, R.M., Stanisz, G.J., Graham, S.J., 2001. Magnetization transfer in MRI: a review. NMR Biomed 14, 57-64.

Horch, R.A., Gore, J.C., Does, M.D., 2011. Origins of the Ultrashort-T(2)(1)H NMR Signals in Myelinated Nerve: A Direct Measure of Myelin Content? Magnetic resonance in medicine : official journal of the Society of Magnetic Resonance in Medicine / Society of Magnetic Resonance in Medicine 66, 24-31.

Keiper, M.D., Grossman, R.I., Hirsch, J.A., Bolinger, L., Ott, I.L., Mannon, L.J., Langlotz, C.P., Kolson, D.L., 1998. MR identification of white matter abnormalities in multiple sclerosis: a comparison between 1.5 T and 4 T. AJNR Am J Neuroradiol 19, 1489-1493.

Lauterbur, P.C., 1973. Image Formation by Induced Local Interactions - Examples Employing Nuclear Magnetic-Resonance. Nature 242, 190-191.

Le Bihan, D., Breton, E., Lallemand, D., Grenier, P., Cabanis, E., Laval-Jeantet, M., 1986. MR imaging of intravoxel incoherent motions: application to diffusion and perfusion in neurologic disorders. Radiology 161, 401-407.

Liu, C., Li, W., Johnson, G.A., Wu, B., 2011. High-field (9.4 T) MRI of brain dysmyelination by quantitative mapping of magnetic susceptibility. Neuroimage 56, 930-938.

Lucchinetti, C., Bruck, W., Parisi, J., Scheithauer, B., Rodriguez, M., Lassmann, H., 2000. Heterogeneity of multiple sclerosis lesions: implications for the pathogenesis of demyelination. Ann Neurol 47, 707-717.

MacKay, A., Whittall, K., Adler, J., Li, D., Paty, D., Graeb, D., 1994. In vivo visualization of myelin water in brain by magnetic resonance. Magn Reson Med 31, 673-677.

Maggs, F.G., Palace, J., 2004. The pathogenesis of multiple sclerosis: is it really a primary inflammatory process? Mult Scler 10, 326-329.

Mansfield, P., Grannell, P.K., 1973. Nmr Diffraction in Solids. Journal of Physics C-Solid State Physics 6, L422-L426.

McDonald, W.I., Compston, A., Edan, G., Goodkin, D., Hartung, H.P., Lublin, F.D., McFarland, H.F., Paty, D.W., Polman, C.H., Reingold, S.C., Sandberg-Wollheim, M., Sibley, W., Thompson, A., van den Noort, S., Weinshenker, B.Y., Wolinsky, J.S., 2001. Recommended diagnostic criteria for multiple sclerosis: guidelines from the International Panel on the diagnosis of multiple sclerosis. Ann Neurol 50, 121-127.

Milo, R., Miller, A., 2014. Revised diagnostic criteria of multiple sclerosis. Autoimmun Rev 13, 518-524.

Moseley, M.E., Cohen, Y., Mintorovitch, J., Chileuitt, L., Shimizu, H., Kucharczyk, J., Wendland, M.F., Weinstein, P.R., 1990. Early detection of regional cerebral ischemia in cats: comparison of diffusion- and T2-weighted MRI and spectroscopy. Magn Reson Med 14, 330-346.

Naci, H., Fleurence, R., Birt, J., Duhig, A., 2010. Economic burden of multiple sclerosis: a systematic review of the literature. Pharmacoeconomics 28, 363-379.

Norton, W.T., Autilio, L.A., 1966. LIPID COMPOSITION OF PURIFIED BOVINE BRAIN MYELIN. Journal of Neurochemistry 13, 213-&.

Obrien, J.S., Sampson, E.L., 1965. LIPID COMPOSITION OF NORMAL HUMAN BRAIN - GRAY MATTER WHITE MATTER AND MYELIN. J Lipid Res 6, 537-&.

Polman, C.H., Reingold, S.C., Banwell, B., Clanet, M., Cohen, J.A., Filippi, M., Fujihara, K., Havrdova, E., Hutchinson, M., Kappos, L., Lublin, F.D., Montalban, X., O'Connor, P., Sandberg-Wollheim, M., Thompson, A.J., Waubant, E., Weinshenker, B., Wolinsky, J.S., 2011. Diagnostic criteria for multiple sclerosis: 2010 revisions to the McDonald criteria. Ann Neurol 69, 292-302.

Polman, C.H., Reingold, S.C., Edan, G., Filippi, M., Hartung, H.P., Kappos, L., Lublin, F.D., Metz, L.M., McFarland, H.F., O'Connor, P.W., Sandberg-Wollheim, M., Thompson, A.J.,

Weinshenker, B.G., Wolinsky, J.S., 2005. Diagnostic criteria for multiple sclerosis: 2005 revisions to the "McDonald Criteria". Ann Neurol 58, 840-846.

Sehy, J.V., Ackerman, J.J.H., Neil, J.J., 2002. Evidence that both fast and slow water ADC components arise from intracellular space. Magnetic Resonance in Medicine 48, 765-770.

Sicotte, N.L., Voskuhl, R.R., Bouvier, S., Klutch, R., Cohen, M.S., Mazziotta, J.C., 2003. Comparison of multiple sclerosis lesions at 1.5 and 3.0 Tesla. Invest Radiol 38, 423-427.

Silver, N.C., Barker, G.J., Miller, D.H., 1999. Standardization of magnetization transfer imaging for multicenter studies. Neurology 53, S33-39.

Song, S.K., Sun, S.W., Ramsbottom, M.J., Chang, C., Russell, J., Cross, A.H., 2002. Dysmyelination revealed through MRI as increased radial (but unchanged axial) diffusion of water. Neuroimage 17, 1429-1436.

Stejskal, E.O., Tanner, J.E., 1965. Spin Diffusion Measurements: Spin Echoes in the Presence of a Time-Dependent Field Gradient. Journal of Chemical Physics 42, 288-+.

Tofts, P.S., Steens, S.C., Cercignani, M., Admiraal-Behloul, F., Hofman, P.A., van Osch, M.J., Teeuwisse, W.M., Tozer, D.J., van Waesberghe, J.H., Yeung, R., Barker, G.J., van Buchem, M.A., 2006. Sources of variation in multi-centre brain MTR histogram studies: body-coil transmission eliminates inter-centre differences. MAGMA 19, 209-222.

van Buchem, M.A., Tofts, P.S., 2000. Magnetization transfer imaging. Neuroimaging Clin N Am 10, 771-788 ,ix.

Vavasour, I.M., Clark, C.M., Li, D.K., Mackay, A.L., 2006. Reproducibility and reliability of MR measurements in white matter: clinical implications. Neuroimage 32, 637-642.

Weinshenker, B.G., Bass, B., Rice, G.P., Noseworthy, J., Carriere, W., Baskerville, J., Ebers, G.C., 1989. The natural history of multiple sclerosis: a geographically based study. I. Clinical course and disability. Brain 112 (Pt 1), 133-146.

Wolff, S.D., Balaban, R.S., 1989. Magnetization transfer contrast (MTC) and tissue water proton relaxation in vivo. Magn Reson Med 10, 135-144.

Young, I.R., Hall, A.S., Pallis, C.A., Legg, N.J., Bydder, G.M., Steiner, R.E., 1981. Nuclear magnetic resonance imaging of the brain in multiple sclerosis. Lancet 2, 1063-1066.

Berry, I., Barker, G.J., Barkhof, F., Campi, A., Dousset, V., Franconi, J.M., Gass, A., Schreiber, W., Miller, D.H., Tofts, P.S., 1999. A multicenter measurement of magnetization transfer ratio in normal white matter. J Magn Reson Imaging 9, 441-446.

Bodhireddy, S.R., Lyman, W.D., Rashbaum, W.K., Weidenheim, K.M., 1994. Immunohistochemical detection of myelin basic protein is a sensitive marker of myelination in second trimester human fetal spinal cord. J Neuropathol Exp Neurol 53, 144-149.

Compston, A., Coles, A., 2002. Multiple sclerosis. The Lancet 359, 1221-1231.

Cook, L.L., Foster, P.J., Mitchell, J.R., Karlik, S.J., 2004. In vivo 4.0-T magnetic resonance investigation of spinal cord inflammation, demyelination, and axonal damage in chronic-progressive experimental allergic encephalomyelitis. J Magn Reson Imaging 20, 563-571.

Does, M.D., Beaulieu, C., Allen, P.S., Snyder, R.E., 1998. Multi-component T1 relaxation and magnetisation transfer in peripheral nerve. Magn Reson Imaging 16, 1033-1041.

Dousset, V., Grossman, R.I., Ramer, K.N., Schnall, M.D., Young, L.H., Gonzalez-Scarano, F., Lavi, E., Cohen, J.A., 1992. Experimental allergic encephalomyelitis and multiple sclerosis: lesion characterization with magnetization transfer imaging. Radiology 182, 483-491.

Dula, A.N., Gochberg, D.F., Valentine, H.L., Valentine, W.M., Does, M.D., 2010. Multi-exponential T(2), Magnetization Transfer and Quantitative Histology in White Matter Tracts of Rat Spinal Cord. Magnetic resonance in medicine : official journal of the Society of Magnetic Resonance in Medicine / Society of Magnetic Resonance in Medicine 63, 902-909.

Fralix, T.A., Ceckler, T.L., Wolff, S.D., Simon, S.A., Balaban, R.S., 1991. Lipid bilayer and water proton magnetization transfer: effect of cholesterol. Magn Reson Med 18, 214-223.

Gareau, P.J., Rutt, B.K., Karlik, S.J., Mitchell, J.R., 2000. Magnetization transfer and multicomponent T2 relaxation measurements with histopathologic correlation in an experimental model of MS. J Magn Reson Imaging 11, 586-595.

Gass, A., Barker, G.J., Kidd, D., Thorpe, J.W., MacManus, D., Brennan, A., Tofts, P.S., Thompson, A.J., McDonald, W.I., Miller, D.H., 1994. Correlation of magnetization transfer ratio with clinical disability in multiple sclerosis. Ann Neurol 36, 62-67.

Ge, Y., Grossman, R.I., Udupa, J.K., Babb, J.S., Kolson, D.L., McGowan, J.C., 2001. Magnetization transfer ratio histogram analysis of gray matter in relapsing-remitting multiple sclerosis. AJNR Am J Neuroradiol 22, 470-475.

Gochberg, D.F., Gore, J.C., 2007a. Quantitative magnetization transfer imaging via selective inversion recovery with short repetition times. Magn Reson Med 57, 437-441.

Gochberg, D.F., Gore, J.C., 2007b. Quantitative magnetization transfer imaging via selective inversion recovery with short repetition times. Magnetic Resonance in Medicine 57, 437-441.

Gore, J.C., Doyle, F.H., Pennock, J.M., 1981. Nuclear Magnetic Resonance (NMR) Imaging At Hammersmith Hospital. pp. 8-10.

Henkelman, R.M., Huang, X., Xiang, Q.S., Stanisz, G.J., Swanson, S.D., Bronskill, M.J., 1993. Quantitative interpretation of magnetization transfer. Magn Reson Med 29, 759-766.

Henkelman, R.M., Stanisz, G.J., Graham, S.J., 2001. Magnetization transfer in MRI: a review. NMR Biomed 14, 57-64.

Kluver, H., Barrera, E., 1953. A method for the combined staining of cells and fibers in the nervous system. J Neuropathol Exp Neurol 12, 400-403.

Koenig, S.H., 1991. Cholesterol of myelin is the determinant of gray-white contrast in MRI of brain. Magn Reson Med 20, 285-291.

Kucharczyk, W., Macdonald, P.M., Stanisz, G.J., Henkelman, R.M., 1994. Relaxivity and magnetization transfer of white matter lipids at MR imaging: importance of cerebrosides and pH. Radiology 192, 521-529.

Lauterbur, P.C., 1973. Image Formation by Induced Local Interactions - Examples Employing Nuclear Magnetic-Resonance. Nature 242, 190-191.

Llufriu, S., Blanco, Y., Martinez-Heras, E., Casanova-Molla, J., Gabilondo, I., Sepulveda, M., Falcon, C., Berenguer, J., Bargallo, N., Villoslada, P., Graus, F., Valls-Sole, J., Saiz, A., 2012. Influence of Corpus Callosum Damage on Cognition and Physical Disability in Multiple Sclerosis: A Multimodal Study. PLoS One 7, e37167.

Lucchinetti, C., Bruck, W., Parisi, J., Scheithauer, B., Rodriguez, M., Lassmann, H., 2000. Heterogeneity of multiple sclerosis lesions: implications for the pathogenesis of demyelination. Ann Neurol 47, 707-717.

Macenko, M., Niethammer, M., Marron, J.S., Borland, D., Woosley, J.T., Xiaojun, G., Schmitt, C., Thomas, N.E., 2009. A method for normalizing histology slides for quantitative analysis. Biomedical Imaging: From Nano to Macro, 2009. ISBI '09. IEEE International Symposium on, pp. 1107-1110.

Mansfield, P., Grannell, P.K., 1973. Nmr Diffraction in Solids. Journal of Physics C-Solid State Physics 6, L422-L426.

Polman, C.H., Reingold, S.C., Banwell, B., Clanet, M., Cohen, J.A., Filippi, M., Fujihara, K., Havrdova, E., Hutchinson, M., Kappos, L., Lublin, F.D., Montalban, X., O'Connor, P., Sandberg-Wollheim, M., Thompson, A.J., Waubant, E., Weinshenker, B., Wolinsky, J.S., 2011. Diagnostic criteria for multiple sclerosis: 2010 revisions to the McDonald criteria. Ann Neurol 69, 292-302.

Rodney, A.B., Giovanni Di, C., Mark, R.K., 1980. Explanation of Cerebral White-Gray Contrast in Computed Tomography. Journal of Computer Assisted Tomography 4, 489-489.

Rovira-Canellas, A., Alonso-Farre, J., Rio-Izquierdo, J., 2000. [Magnetic resonance in the clinical and therapeutic follow-up of multiple sclerosis]. Rev Neurol 30, 980-985.

Salthouse, T.N., 1962. A quantitative histochemical method for estimating phospholipids. Nature 195, 187-188.

Samsonov, A., Alexander, A.L., Mossahebi, P., Wu, Y.C., Duncan, I.D., Field, A.S., 2012. Quantitative MR imaging of two-pool magnetization transfer model parameters in myelin mutant shaking pup. Neuroimage 62, 1390-1398.

Scholtz, C.L., 1977. Quantitative histochemistry of myelin using Luxol Fast Blue MBS. Histochem J 9, 759-765.

Sehy, J.V., Ackerman, J.J.H., Neil, J.J., 2002. Evidence that both fast and slow water ADC components arise from intracellular space. Magnetic Resonance in Medicine 48, 765-770.

Silver, N.C., Barker, G.J., Miller, D.H., 1999. Standardization of magnetization transfer imaging for multicenter studies. Neurology 53, S33-39.

Simmons, D.M., Swanson, L.W., 2009. Comparing histological data from different brains: sources of error and strategies for minimizing them. Brain Res Rev 60, 349-367.

Simons, M., Misgeld, T., Kerschensteiner, M., 2014. A unified cell biological perspective on axon-myelin injury. J Cell Biol 206, 335-345.

Stejskal, E.O., Tanner, J.E., 1965. Spin Diffusion Measurements: Spin Echoes in the Presence of a Time-Dependent Field Gradient. Journal of Chemical Physics 42, 288-+.

Tofts, P.S., Steens, S.C., Cercignani, M., Admiraal-Behloul, F., Hofman, P.A., van Osch, M.J., Teeuwisse, W.M., Tozer, D.J., van Waesberghe, J.H., Yeung, R., Barker, G.J., van Buchem, M.A., 2006. Sources of variation in multi-centre brain MTR histogram studies: body-coil transmission eliminates inter-centre differences. MAGMA 19, 209-222.

Underhill, H.R., Rostomily, R.C., Mikheev, A.M., Yuan, C., Yarnykh, V.L., 2011. Fast bound pool fraction imaging of the in vivo rat brain: association with myelin content and validation in the C6 glioma model. Neuroimage 54, 2052-2065.

van Buchem, M.A., Tofts, P.S., 2000. Magnetization transfer imaging. Neuroimaging Clin N Am 10, 771-788 ,ix.

Vavasour, I.M., Clark, C.M., Li, D.K., Mackay, A.L., 2006. Reproducibility and reliability of MR measurements in white matter: clinical implications. Neuroimage 32, 637-642.

Wolff, S.D., Balaban, R.S., 1989. Magnetization transfer contrast (MTC) and tissue water proton relaxation in vivo. Magn Reson Med 10, 135-144.

Young, I.R., Hall, A.S., Pallis, C.A., Legg, N.J., Bydder, G.M., Steiner, R.E., 1981. Nuclear magnetic resonance imaging of the brain in multiple sclerosis. Lancet 2, 1063-1066.

Assaf, Y., Pasternak, O., 2008. Diffusion tensor imaging (DTI)-based white matter mapping in brain research: a review. J Mol Neurosci 34, 51-61.

Barkhof, F., Filippi, M., Miller, D.H., Scheltens, P., Campi, A., Polman, C.H., Comi, G., Ader, H.J., Losseff, N., Valk, J., 1997. Comparison of MRI criteria at first presentation to predict conversion to clinically definite multiple sclerosis. Brain 120 (Pt 11), 2059-2069.

Barkovich, A.J., 2005. Magnetic resonance techniques in the assessment of myelin and myelination. J Inherit Metab Dis 28, 311-343.

Basser, P.J., Mattiello, J., LeBihan, D., 1994a. Estimation of the effective self-diffusion tensor from the NMR spin echo. J Magn Reson B 103, 247-254.

Basser, P.J., Mattiello, J., LeBihan, D., 1994b. MR diffusion tensor spectroscopy and imaging. Biophys J 66, 259-267.

Basser, P.J., Pierpaoli, C., 1996. Microstructural and physiological features of tissues elucidated by quantitative-diffusion-tensor MRI. Journal of Magnetic Resonance Series B 111, 209-219.

Basser, P.J., Pierpaoli, C., 1998. A simplified method to measure the diffusion tensor from seven MR images. Magnetic Resonance in Medicine 39, 928-934.

Beaulieu, C., 2002. The basis of anisotropic water diffusion in the nervous system - a technical review. NMR Biomed 15, 435-455.

Berry, I., Barker, G.J., Barkhof, F., Campi, A., Dousset, V., Franconi, J.M., Gass, A., Schreiber, W., Miller, D.H., Tofts, P.S., 1999a. A multicenter measurement of magnetization transfer ratio in normal white matter. Journal of Magnetic Resonance Imaging 9, 441-446.

Berry, I., Barker, G.J., Barkhof, F., Campi, A., Dousset, V., Franconi, J.M., Gass, A., Schreiber, W., Miller, D.H., Tofts, P.S., 1999b. A multicenter measurement of magnetization transfer ratio in normal white matter. J Magn Reson Imaging 9, 441-446.

Bodhireddy, S.R., Lyman, W.D., Rashbaum, W.K., Weidenheim, K.M., 1994. Immunohistochemical detection of myelin basic protein is a sensitive marker of myelination in second trimester human fetal spinal cord. J Neuropathol Exp Neurol 53, 144-149.

Budde, M.D., Kim, J.H., Liang, H.F., Russell, J.H., Cross, A.H., Song, S.K., 2008. Axonal injury detected by in vivo diffusion tensor imaging correlates with neurological disability in a mouse model of multiple sclerosis. NMR Biomed 21, 589-597.

Compston, A., Coles, A., 2002. Multiple sclerosis. The Lancet 359, 1221-1231.

Confavreux, C., Vukusic, S., Moreau, T., Adeleine, P., 2000. Relapses and progression of disability in multiple sclerosis. N Engl J Med 343, 1430-1438.

Cook, L.L., Foster, P.J., Mitchell, J.R., Karlik, S.J., 2004. In vivo 4.0-T magnetic resonance investigation of spinal cord inflammation, demyelination, and axonal damage in chronic-progressive experimental allergic encephalomyelitis. J Magn Reson Imaging 20, 563-571.

D'Arceuil, H.E., Westmoreland, S., de Crespigny, A.J., 2007. An approach to high resolution diffusion tensor imaging in fixed primate brain. Neuroimage 35, 553-565.

Deloire-Grassin, M.S.A., Brochet, B., Quesson, B., Delalande, C., Dousset, V., Canioni, P., Petry, K.G., 2000. In vivo evaluation of remyelination in rat brain by magnetization transfer imaging. Journal of the Neurological Sciences 178, 10-16.

Does, M.D., Beaulieu, C., Allen, P.S., Snyder, R.E., 1998. Multi-component T1 relaxation and magnetisation transfer in peripheral nerve. Magn Reson Imaging 16, 1033-1041.

Does, M.D., Snyder, R.E., 1996. Multiexponential T2 relaxation in degenerating peripheral nerve. Magn Reson Med 35, 207-213.

Dousset, V., Grossman, R.I., Ramer, K.N., Schnall, M.D., Young, L.H., Gonzalez-Scarano, F., Lavi, E., Cohen, J.A., 1992. Experimental allergic encephalomyelitis and multiple sclerosis: lesion characterization with magnetization transfer imaging. Radiology 182, 483-491.

Dula, A.N., Gochberg, D.F., Valentine, H.L., Valentine, W.M., Does, M.D., 2010a. Multi-exponential T(2), Magnetization Transfer and Quantitative Histology in White Matter Tracts of Rat Spinal Cord. Magnetic resonance in medicine : official journal of the Society of Magnetic Resonance in Medicine / Society of Magnetic Resonance in Medicine 63, 902-909.

Dula, A.N., Gochberg, D.F., Valentine, H.L., Valentine, W.M., Does, M.D., 2010b. Multiexponential T-2, Magnetization Transfer, and Quantitative Histology in White Matter Tracts of Rat Spinal Cord. Magnetic Resonance in Medicine 63, 902-909.

Edzes, H.T., Samulski, E.T., 1977. Cross relaxation and spin diffusion in the proton NMR or hydrated collagen. Nature 265, 521-523.

Fatouros, P.P., Marmarou, A., Kraft, K.A., Inao, S., Schwarz, F.P., 1991. In vivo brain water determination by T1 measurements: effect of total water content, hydration fraction, and field strength. Magn Reson Med 17, 402-413.

Felts, P.A., Woolston, A.M., Fernando, H.B., Asquith, S., Gregson, N.A., Mizzi, O.J., Smith, K.J., 2005. Inflammation and primary demyelination induced by the intraspinal injection of lipopolysaccharide. Brain 128, 1649-1666.

Filippi, M., 2011. Multiple sclerosis in 2010: Advances in monitoring and treatment of multiple sclerosis. Nat Rev Neurol 7, 74-75.

Fralix, T.A., Ceckler, T.L., Wolff, S.D., Simon, S.A., Balaban, R.S., 1991. Lipid bilayer and water proton magnetization transfer: effect of cholesterol. Magn Reson Med 18, 214-223.

Gareau, P.J., Rutt, B.K., Karlik, S.J., Mitchell, J.R., 2000. Magnetization transfer and multicomponent T2 relaxation measurements with histopathologic correlation in an experimental model of MS. J Magn Reson Imaging 11, 586-595.

Gass, A., Barker, G.J., Kidd, D., Thorpe, J.W., MacManus, D., Brennan, A., Tofts, P.S., Thompson, A.J., McDonald, W.I., Miller, D.H., 1994. Correlation of magnetization transfer ratio with clinical disability in multiple sclerosis. Ann Neurol 36, 62-67.

Ge, Y., Grossman, R.I., Udupa, J.K., Babb, J.S., Kolson, D.L., McGowan, J.C., 2001. Magnetization transfer ratio histogram analysis of gray matter in relapsing-remitting multiple sclerosis. AJNR Am J Neuroradiol 22, 470-475.

Gochberg, D.F., Gore, J.C., 2003. Quantitative imaging of magnetization transfer using an inversion recovery sequence. Magnetic Resonance in Medicine 49, 501-505.

Gochberg, D.F., Gore, J.C., 2007a. Quantitative magnetization transfer imaging via selective inversion recovery with short repetition times. Magn Reson Med 57, 437-441.

Gochberg, D.F., Gore, J.C., 2007b. Quantitative magnetization transfer imaging via selective inversion recovery with short repetition times. Magnetic Resonance in Medicine 57, 437-441.

Gore, J.C., Doyle, F.H., Pennock, J.M., 1981. Nuclear Magnetic Resonance (NMR) Imaging At Hammersmith Hospital. pp. 8-10.

Hansen, J.R., 1971. Pulsed NMR study of water mobility in muscle and brain tissue. Biochim Biophys Acta 230, 482-486.

Hauser, S., 1994. Multiple sclerosis and other demyelinating diseases. In: Isselbacher KJ, Martin JB, Fauci AS, et al, eds. Harrison’s principles of internal medicine. New York: McGraw-Hill.

Henkelman, R.M., Huang, X.M., Xiang, Q.S., Stanisz, G.J., Swanson, S.D., Bronskill, M.J., 1993. Quantitative Interpretation of Magnetization-Transfer. Magnetic Resonance in Medicine 29, 759-766.

Henkelman, R.M., Stanisz, G.J., Graham, S.J., 2001. Magnetization transfer in MRI: a review. NMR Biomed 14, 57-64.

Horch, R.A., Gore, J.C., Does, M.D., 2011. Origins of the Ultrashort-T(2)(1)H NMR Signals in Myelinated Nerve: A Direct Measure of Myelin Content? Magnetic resonance in medicine : official journal of the Society of Magnetic Resonance in Medicine / Society of Magnetic Resonance in Medicine 66, 24-31.

Inglese, M., 2006. Multiple sclerosis: new insights and trends. AJNR Am J Neuroradiol 27, 954-957.

Kamman, R.L., Go, K.G., Brouwer, W., Berendsen, H.J., 1988. Nuclear magnetic resonance relaxation in experimental brain edema: effects of water concentration, protein concentration, and temperature. Magn Reson Med 6, 265-274.

Keiper, M.D., Grossman, R.I., Hirsch, J.A., Bolinger, L., Ott, I.L., Mannon, L.J., Langlotz, C.P., Kolson, D.L., 1998. MR identification of white matter abnormalities in multiple sclerosis: a comparison between 1.5 T and 4 T. AJNR Am J Neuroradiol 19, 1489-1493.

Klawiter, E.C., Schmidt, R.E., Trinkaus, K., Liang, H.F., Budde, M.D., Naismith, R.T., Song, S.K., Cross, A.H., Benzinger, T.L., 2011. Radial diffusivity predicts demyelination in ex vivo multiple sclerosis spinal cords. Neuroimage 55, 1454-1460.

Kluver, H., Barrera, E., 1953. A method for the combined staining of cells and fibers in the nervous system. J Neuropathol Exp Neurol 12, 400-403.

Koenig, S.H., 1991. Cholesterol of myelin is the determinant of gray-white contrast in MRI of brain. Magn Reson Med 20, 285-291.

Kucharczyk, W., Macdonald, P.M., Stanisz, G.J., Henkelman, R.M., 1994. Relaxivity and magnetization transfer of white matter lipids at MR imaging: importance of cerebrosides and pH. Radiology 192, 521-529.

Lassmann, H., Bruck, W., Lucchinetti, C., 2001. Heterogeneity of multiple sclerosis pathogenesis: implications for diagnosis and therapy. Trends Mol Med 7, 115-121.

Laule, C., Leung, E., Li, D.K.B., Troboulsee, A.L., Paty, D.W., MacKay, A.L., Moore, G.R.W., 2006. Myelin water imaging in multiple sclerosis: quantitative correlations with histopathology. Multiple Sclerosis 12, 747-753.

Lauterbur, P.C., 1973. Image Formation by Induced Local Interactions - Examples Employing Nuclear Magnetic-Resonance. Nature 242, 190-191.

Le Bihan, D., Breton, E., Lallemand, D., Grenier, P., Cabanis, E., Laval-Jeantet, M., 1986. MR imaging of intravoxel incoherent motions: application to diffusion and perfusion in neurologic disorders. Radiology 161, 401-407.

Li, K., Zu, Z.L., Xu, J.Z., Janve, V.A., Gore, J.C., Does, M.D., Gochberg, D.F., 2010. Optimized Inversion Recovery Sequences for Quantitative T(1) and Magnetization Transfer Imaging. Magnetic Resonance in Medicine 64, 491-500.

Liu, C., Li, W., Johnson, G.A., Wu, B., 2011. High-field (9.4 T) MRI of brain dysmyelination by quantitative mapping of magnetic susceptibility. Neuroimage 56, 930-938.

Lucchinetti, C., Bruck, W., Noseworthy, J., 2001. Multiple sclerosis: recent developments in neuropathology, pathogenesis, magnetic resonance imaging studies and treatment. Curr Opin Neurol 14, 259-269.

Lucchinetti, C., Bruck, W., Parisi, J., Scheithauer, B., Rodriguez, M., Lassmann, H., 2000. Heterogeneity of multiple sclerosis lesions: implications for the pathogenesis of demyelination. Ann Neurol 47, 707-717.

Macenko, M., Niethammer, M., Marron, J.S., Borland, D., Woosley, J.T., Xiaojun, G., Schmitt, C., Thomas, N.E., 2009. A method for normalizing histology slides for quantitative analysis. Biomedical Imaging: From Nano to Macro, 2009. ISBI '09. IEEE International Symposium on, pp. 1107-1110.

MacKay, A., Whittall, K., Adler, J., Li, D., Paty, D., Graeb, D., 1994. In vivo visualization of myelin water in brain by magnetic resonance. Magn Reson Med 31, 673-677.

Maggs, F.G., Palace, J., 2004. The pathogenesis of multiple sclerosis: is it really a primary inflammatory process? Mult Scler 10, 326-329.

Mansfield, P., Grannell, P.K., 1973. Nmr Diffraction in Solids. Journal of Physics C-Solid State Physics 6, L422-L426.

McDonald, W.I., Compston, A., Edan, G., Goodkin, D., Hartung, H.P., Lublin, F.D., McFarland, H.F., Paty, D.W., Polman, C.H., Reingold, S.C., Sandberg-Wollheim, M., Sibley, W., Thompson, A., van den Noort, S., Weinshenker, B.Y., Wolinsky, J.S., 2001. Recommended diagnostic criteria for multiple sclerosis: guidelines from the International Panel on the diagnosis of multiple sclerosis. Ann Neurol 50, 121-127.

Milo, R., Miller, A., 2014. Revised diagnostic criteria of multiple sclerosis. Autoimmun Rev 13, 518-524.

Moseley, M.E., Cohen, Y., Mintorovitch, J., Chileuitt, L., Shimizu, H., Kucharczyk, J., Wendland, M.F., Weinstein, P.R., 1990. Early detection of regional cerebral ischemia in cats: comparison of diffusion- and T2-weighted MRI and spectroscopy. Magn Reson Med 14, 330-346.

Naci, H., Fleurence, R., Birt, J., Duhig, A., 2010. Economic burden of multiple sclerosis: a systematic review of the literature. Pharmacoeconomics 28, 363-379.

Norton, W.T., Autilio, L.A., 1966. The lipid composition of purified bovine brain myelin. Journal of Neurochemistry 13, 213-222.

Noseworthy, J.H., Lucchinetti, C., Rodriguez, M., Weinshenker, B.G., 2000. Multiple sclerosis. N Engl J Med 343, 938-952.

Obrien, J.S., Sampson, E.L., 1965. LIPID COMPOSITION OF NORMAL HUMAN BRAIN - GRAY MATTER WHITE MATTER AND MYELIN. J Lipid Res 6, 537-&.

Odrobina, E.E., Lam, T.Y., Pun, T., Midha, R., Stanisz, G.J., 2005. MR properties of excised neural tissue following experimentally induced demyelination. NMR Biomed 18, 277-284.

Ou, X., Gochberg, D.F., 2008. MT effects and T1 quantification in single-slice spoiled gradient echo imaging. Magn Reson Med 59, 835-845.

Ou, X.W., Sun, S.W., Liang, H.F., Song, S.K., Gochberg, D.F., 2009. The MT pool size ratio and the DTI radial diffusivity may reflect the myelination in shiverer and control mice. Nmr in Biomedicine 22, 480-487.

Polman, C.H., Reingold, S.C., Banwell, B., Clanet, M., Cohen, J.A., Filippi, M., Fujihara, K., Havrdova, E., Hutchinson, M., Kappos, L., Lublin, F.D., Montalban, X., O'Connor, P., Sandberg-Wollheim, M., Thompson, A.J., Waubant, E., Weinshenker, B., Wolinsky, J.S., 2011. Diagnostic criteria for multiple sclerosis: 2010 revisions to the McDonald criteria. Ann Neurol 69, 292-302.

Polman, C.H., Reingold, S.C., Edan, G., Filippi, M., Hartung, H.P., Kappos, L., Lublin, F.D., Metz, L.M., McFarland, H.F., O'Connor, P.W., Sandberg-Wollheim, M., Thompson, A.J., Weinshenker, B.G., Wolinsky, J.S., 2005a. Diagnostic criteria for multiple sclerosis: 2005 revisions to the "McDonald Criteria". Ann Neurol 58, 840-846.

Polman, C.H., Wolinsky, J.S., Reingold, S.C., 2005b. Multiple sclerosis diagnostic criteria: three years later. Mult Scler 11, 5-12.

Prantner, A.M., Bretthorst, G.L., Neil, J.J., Garbow, J.R., Ackerman, J.J.H., 2008. Magnetization transfer induced biexponential longitudinal relaxation. Magnetic Resonance in Medicine 60, 555-563.

Quarles R, M.W., Morell P., 2006. Myelin formation, structure and biochemistry. Elsevier Academic Press, London.

Rausch, M., Tofts, P., Lervik, P., Walmsley, A., Mir, A., Schubart, A., Seabrook, T., 2009. Characterization of white matter damage in animal models of multiple sclerosis by magnetization transfer ratio and quantitative mapping of the apparent bound proton fraction f. Mult Scler 15, 16-27.

Rodney, A.B., Giovanni Di, C., Mark, R.K., 1980. Explanation of Cerebral White-Gray Contrast in Computed Tomography. Journal of Computer Assisted Tomography 4, 489-489.

Rovira-Canellas, A., Alonso-Farre, J., Rio-Izquierdo, J., 2000. [Magnetic resonance in the clinical and therapeutic follow-up of multiple sclerosis]. Rev Neurol 30, 980-985.

Salthouse, T.N., 1962. A quantitative histochemical method for estimating phospholipids. Nature 195, 187-188.

Samsonov, A., Alexander, A.L., Mossahebi, P., Wu, Y.C., Duncan, I.D., Field, A.S., 2012. Quantitative MR imaging of two-pool magnetization transfer model parameters in myelin mutant shaking pup. Neuroimage 62, 1390-1398.

Schmierer, K., Scaravilli, F., Altmann, D.R., Barker, G.J., Miller, D.H., 2004. Magnetization transfer ratio and myelin in postmortem multiple sclerosis brain. Annals of Neurology 56, 407-415.

Scholtz, C.L., 1977. Quantitative histochemistry of myelin using Luxol Fast Blue MBS. Histochem J 9, 759-765.

Sehy, J.V., Ackerman, J.J.H., Neil, J.J., 2002. Evidence that both fast and slow water ADC components arise from intracellular space. Magnetic Resonance in Medicine 48, 765-770.

Shamy, J.L., Carpenter, D.M., Fong, S.G., Murray, E.A., Tang, C.Y., Hof, P.R., Rapp, P.R., 2010. Alterations of White Matter Tracts Following Neurotoxic Hippocampal Lesions in Macaque Monkeys: A Diffusion Tensor Imaging Study. Hippocampus 20, 906-910.

Sicotte, N.L., Voskuhl, R.R., Bouvier, S., Klutch, R., Cohen, M.S., Mazziotta, J.C., 2003. Comparison of multiple sclerosis lesions at 1.5 and 3.0 Tesla. Invest Radiol 38, 423-427.

Silver, N.C., Barker, G.J., Miller, D.H., 1999. Standardization of magnetization transfer imaging for multicenter studies. Neurology 53, S33-39.

Simmons, D.M., Swanson, L.W., 2009. Comparing histological data from different brains: sources of error and strategies for minimizing them. Brain Res Rev 60, 349-367.

Simons, M., Misgeld, T., Kerschensteiner, M., 2014. A unified cell biological perspective on axon-myelin injury. J Cell Biol 206, 335-345.

Song, S.K., Sun, S.W., Ramsbottom, M.J., Chang, C., Russell, J., Cross, A.H., 2002. Dysmyelination revealed through MRI as increased radial (but unchanged axial) diffusion of water. Neuroimage 17, 1429-1436.

Song, S.K., Yoshino, J., Le, T.Q., Lin, S.J., Sun, S.W., Cross, A.H., Armstrong, R.C., 2005. Demyelination increases radial diffusivity in corpus callosum of mouse brain. Neuroimage 26, 132-140.

Sriram, S., Yao, S.Y., Natarajan, C., Zhang, F.L., 2012. Innate Immunity Mediated Model of Primary Oligodendrogliopathy. Neurology 78.

Stejskal, E.O., Tanner, J.E., 1965. Spin Diffusion Measurements: Spin Echoes in the Presence of a Time-Dependent Field Gradient. Journal of Chemical Physics 42, 288-+.

Stikov, N., Perry, L.M., Mezer, A., Rykhlevskaia, E., Wandell, B.A., Pauly, J.M., Dougherty, R.F., 2011. Bound pool fractions complement diffusion measures to describe white matter micro and macrostructure. Neuroimage 54, 1112-1121.

Tofts, P.S., Steens, S.C., Cercignani, M., Admiraal-Behloul, F., Hofman, P.A., van Osch, M.J., Teeuwisse, W.M., Tozer, D.J., van Waesberghe, J.H., Yeung, R., Barker, G.J., van Buchem, M.A., 2006. Sources of variation in multi-centre brain MTR histogram studies: body-coil transmission eliminates inter-centre differences. MAGMA 19, 209-222.

Trapp, B.D., Nave, K.A., 2008. Multiple sclerosis: an immune or neurodegenerative disorder? Annu Rev Neurosci 31, 247-269.

Underhill, H.R., Rostomily, R.C., Mikheev, A.M., Yuan, C., Yarnykh, V.L., 2011. Fast bound pool fraction imaging of the in vivo rat brain: association with myelin content and validation in the C6 glioma model. Neuroimage 54, 2052-2065.

van Buchem, M.A., Tofts, P.S., 2000. Magnetization transfer imaging. Neuroimaging Clin N Am 10, 771-788 ,ix.

Vavasour, I.M., Clark, C.M., Li, D.K., Mackay, A.L., 2006. Reproducibility and reliability of MR measurements in white matter: clinical implications. Neuroimage 32, 637-642.

Viola, P., Wells, W.M., 1997. Alignment by maximization of mutual information. International Journal of Computer Vision 24, 137-154.

Weinshenker, B.G., 1996. Epidemiology of multiple sclerosis. Neurol Clin 14, 291-308.

Weinshenker, B.G., Bass, B., Rice, G.P., Noseworthy, J., Carriere, W., Baskerville, J., Ebers, G.C., 1989. The natural history of multiple sclerosis: a geographically based study. I. Clinical course and disability. Brain 112 (Pt 1), 133-146.

Wolff, S.D., Balaban, R.S., 1989. Magnetization transfer contrast (MTC) and tissue water proton relaxation in vivo. Magn Reson Med 10, 135-144.

Young, I.R., Hall, A.S., Pallis, C.A., Legg, N.J., Bydder, G.M., Steiner, R.E., 1981. Nuclear magnetic resonance imaging of the brain in multiple sclerosis. Lancet 2, 1063-1066.